



Simulations of laser-driven correlated many-electron dynamics in molecular systems

Dissertation

zur Erlangung des akademischen Grades

“doctor rerum naturalium”

(Dr. rer. nat.)

in der Wissenschaftsdisziplin Theoretische Chemie

eingereicht an der

Mathematisch-Naturwissenschaftlichen Fakultät

der Universität Potsdam

von

Stefan Klinkusch

aus Berlin

Potsdam, im Juni 2011

1. Gutachter: Prof. Dr. Peter Saalfrank
 2. Gutachter: Priv.-Doz. Dr. Alejandro Saenz
 3. Gutachter: Prof. Dr. Mathias Nest
- Tag der Disputation: 20. Oktober 2011

Simulations of laser-driven correlated many-electron dynamics in molecular systems

vorgelegt von Stefan Klinkusch

Im Rahmen dieser Doktorarbeit werden Simulationen lasergetriebener korrelierter Vielelektronendynamik in molekularen Systemen präsentiert. Dabei geht es im einzelnen darum, die Wechselwirkungen elektromagnetischer Wellen mit einem Molekül, insbesondere im Bezug auf Photoionisation, zu demonstrieren. Die Photoionisation wird insbesondere durch hochfrequente und intensive Lichtwellen hervorgerufen. Dabei können Elektronen ausreichend Energie erhalten, um die potentielle Energie zu überwinden und als freie Elektronen betrachtet zu werden. Mit Hilfe des hier vorgestellten Modells lassen sich dann Anregungen zwischen einzelnen Zuständen unterhalb eines Ionisationspotentials, die Anregung von Wellenpaketen und deren Abbildung als Ionisationssignal in der Simulation eines Pump-Probe-Experiments berechnen. Außerdem wird diese Methode verwendet, um den Einfluss auf so genannte Response-Signale zu testen. Als Beispiel soll das hier an der Polarisierbarkeit des Wasserstoffmoleküls demonstriert werden. In einem weiteren Modell werden zustandsselektive Anregungen auch in einer elektronenreichen Umgebung simuliert.

Ein weiterer Teil der Doktorarbeit ist der Elektronenkorrelation gewidmet. Die Hartree-Fock-Theorie, im Rahmen der closed-shell-Näherung, betrachtet keine direkte Wechselwirkung der Elektronen untereinander, sondern lediglich die Wechselwirkung einzelner Elektronen mit einem durch die anderen Elektronen aufgespannten Feld. Dabei entsteht ein Fehler in der Gesamtenergie, der als Korrelationsenergie bezeichnet wird. Die Korrelationsenergie selbst ist für zeitunabhängige Betrachtungen definiert, bei dynamischen Rechnungen nicht einfach zugänglich, aber dennoch von Bedeutung. Deshalb wird die Einelektronenentropie als Maß für die Korrelationsenergie angenommen. Es wird für einfache Systeme (molekularer Wasserstoff, ein Aggregat zweier Heliumatome und ein Methanmolekül) gezeigt, dass diese Annahme sinnvoll und richtig ist. Im weiteren Verlauf wird versucht, diese Systeme mit Laserpulsen zu dekorrelieren, d.h., es wird versucht, die Entropie und damit die Korrelationsenergie zu verringern.

List of publications

- Dominik Kröner, Stefan Klinkusch, and Tillmann Klamroth, “*Enhanced photodesorption by vibrational pre-excitation: Quantum model simulations for Cs/Cu(111)*”, *Surface Science* **602**, 3148-3152 (2008).
- Stefan Klinkusch, Tillmann Klamroth, and Peter Saalfrank, “*Long-range intermolecular charge transfer induced by laser pulses: an explicitly time-dependent configuration interaction approach*”, *Physical Chemistry Chemical Physics* **11**, 3875-3884 (2009).
- Stefan Klinkusch, Peter Saalfrank, and Tillmann Klamroth, “*Laser-induced electron dynamics including photoionization: A heuristic model within time-dependent configuration interaction theory*”, *Journal of Chemical Physics* **131**, 114304 (2009).
- Jean Christophe Tremblay, Stefan Klinkusch, Tillmann Klamroth, and Peter Saalfrank, “*Dissipative many-electron dynamics of ionizing systems*”, *Journal of Chemical Physics* **134**, 044311 (2011).
- Stefan Klinkusch and Tillmann Klamroth, “*Simulations of pump-probe excitations of electronic wave packets for a large quasi-rigid molecular system by means of an extension to the time-dependent configuration interaction singles method*”, in preparation (2011).

Danksagung

Diese Dissertation wurde von April 2008 bis Juni 2011 am Institut für Chemie der Universität Potsdam. Ich möchte allen danken, die durch ihr Mitwirken zum Gelingen der Arbeit beigetragen haben.

Mein besondere Dank gilt meinem Doktorvater, Herrn Prof. Dr. Peter Saalfrank, für die Bereitstellung dieses Forschungsthemas, viele zielführende Diskussionen und die ausgezeichnete Betreuung.

Weiterhin danke ich meinem Betreuer, Herrn Priv.-Doz. Dr. Tillmann Klamroth, für die hervorragende wissenschaftliche und technische Unterstützung, die sehr gute Betreuung und viele Diskussionen.

Ich danke Herrn Dr. Pascal Krause (jetzt in Temple, Philadelphia) für die Einführung in die vorhandenen Programme, die ich zwar bereits für die Erstellung der Diplomarbeit genutzt habe, aber auch hier zum Einsatz kamen.

Außerdem danke ich Herrn Dr. Jean Christophe Tremblay für die gemeinsame Realisierung des Modells zur Betrachtung der Dissipation und Ionisation und für viele Diskussionen.

Ich möchte Frau Dr. Stephanie Beyvers danken für die Einführung in die Programme, die zur Entropieberechnung genutzt werden.

Weiterhin danke ich Herrn Prof. Dr. Mathias Nest (jetzt in München) für die Hilfestellung bei Fragen zum MCTDHF-Programm.

Im Übrigen danke ich der gesamten Arbeitsgruppe für die stets freundliche Arbeitsatmosphäre. Insbesondere sind dabei meine "Office mates" zu nennen, und zwar Dr. Jan Götze (jetzt in Mülheim an der Ruhr), Dr. Tijo Vazhappily (jetzt in den USA), Dr. Padmanaban Ramanathan (jetzt wieder in Indien), Bastian Klaumünzer, Gernot Fücksel, Gereon Floß, Jonas Wirth und Monique Mertens.

Ein ganz besonderer Dank gilt allen in meiner Familie, die mich in irgendeiner Form unterstützt haben, insbesondere meinem Vater, der für mich eine ganz wichtige Stütze ist.

Contents

1	Introduction	1
2	Theoretical foundations and methods	7
2.1	Stationary quantum chemistry	7
2.1.1	The time-independent Schrödinger equation	7
2.1.2	The Hartree-Fock method	8
2.1.3	The Roothaan-Hall equation	10
2.1.4	Electron correlation	11
2.1.5	Configuration Interaction (CI)	12
2.1.5.1	CIS	13
2.1.5.2	CISD	14
2.1.6	The Complete Active Space Self-Consistent Field (CASSCF) method	15
2.2	Quantum electron dynamics in a laser field	15
2.2.1	The time-dependent electronic Schrödinger equation	16
2.2.2	Time-dependent Configuration Interaction (TD-CI)	18
2.2.3	Multi-configuration time-dependent Hartree-Fock (MCTDHF)	19
2.3	Treatment of photoionization	20
2.3.1	Eigenenergy algorithm	21
2.3.2	Configuration State Function (CSF) algorithm	22
2.3.3	Combined algorithm	23
2.3.4	Escape length parameter	23
2.4	Reduced density matrices	24
2.4.1	Calculation of the von Neumann entropy	24
2.4.2	Ionization in a dissipative environment	26
2.5	Laser pulses	28

2.5.1	π -pulses	28
2.5.2	Optimal control theory (OCT)	29
2.5.3	Stochastic pulse optimization (SPO)	30
2.6	Electronic transitions	32
2.6.1	Processes of interest	32
2.6.2	Induced dipole moment	32
3	Molecules in intense laser fields: Photoionization	35
3.1	The lithium cyanide (LiCN) molecule	36
3.1.1	System states and ionization rates	36
3.1.2	Transitions to non-ionizing states	42
3.1.3	Transitions to ionizing states	43
3.1.4	Creation of electronic wavepackets	45
3.1.5	Pump-probe spectra for electronic wavepackets	46
3.2	A more rigid molecule	48
3.2.1	System states and ionization rates	48
3.2.2	Creation of electronic wavepackets	52
3.2.3	Pump-probe spectra	55
3.3	Dynamic polarizabilities for H_2	61
3.3.1	The H_2 molecule as a test system	62
3.4	State-to-state excitations in a dissipative environment	67
3.4.1	System states and ionization rates	67
3.4.2	Laser-driven state-to-state excitations	68
3.4.2.1	Direct excitation	68
4	Correlation and Entropy	73
4.1	Correlation and entropy: Foundations	74
4.1.1	Minimal basis model of H_2	74
4.1.2	Extended basis sets	77
4.1.3	Dynamical aspects	79
4.2	Correlation and entropy: Control	82
4.2.1	Creation of a Hartree-Fock state in CISD space	82
4.2.1.1	CISD representation of the RHF state	82
4.2.1.2	Optimal control theory	84
4.2.1.3	Stochastic pulse optimization	86

4.2.2	Low SEEs with longer characteristic times	87
4.2.2.1	Energy-cutoff criterion	88
4.2.2.2	Population-cutoff criterion	90
4.2.2.3	OCT excitation of “approximate HF wavefunctions”	92
5	Conclusions and Outlook	95
A	Functions of matrices	101
A.1	Functions of diagonal matrices	101
A.2	Functions of diagonalizable matrices	101
B	Propagation in imaginary time	103

Chapter 1

Introduction

The motion of electrons plays a huge role in chemistry, *e.g.* in redox reactions, ring currents, radical reactions and biological function. Also, it is important for electrochemical and STM-induced processes. The theoretical description of these processes is a big challenge for scientists.

A first break-through in the observation of electron movement in real time was the foundation of femtochemistry, *i.e.*, the femtosecond (fs, $1\text{ fs} = 10^{-15}\text{ s}$) laser experiments by Zewail [1,2]. The possibility to generate even attosecond (as, $1\text{ as} = 10^{-18}\text{ s}$) laser pulses [3–6] makes it possible not only to observe but also to control the electron motion. On these timescales a rearrangement of nuclei plays an inferior role.

From the theoretical point of view, some methods to simulate such experiments were developed. All of these methods have in common that they are time-dependent (TD). Ferrell extended the Hartree-Fock (HF) theory [7,8] to the time-dependent Hartree-Fock method (TD-HF) [9] in 1957. In 1984, Runge and Gross developed the time-dependent density functional theory (TD-DFT) [10] to solve the time-dependent Kohn-Sham [11,12] equations. In contrast to TD-HF, which contains no electron correlation, TD-DFT treats the electron correlation using an appropriate functional. There are also multi-determinant approaches to solve a time-dependent electronic Schrödinger equation [13–16], *i.e.*, methods in which the total wavefunction is expanded as a linear combination of electron configurations or determinants. One of these methods is the multi-configuration time-dependent Hartree-Fock method (MCTDHF) which was developed – amongst others – by Scrinzi and coworkers [17–19]. This method can be seen as the time-dependent variant of the

well-known complete active space self-consistent field (CASSCF) method [20], or as an extension for electron dynamics of the multi-configuration time-dependent Hartree (MCTDH) method by Meyer, Manthe, and Cederbaum [21]. The characteristic feature of MCTDHF is the simultaneous propagation of the coefficients of the determinants, and the determinants themselves in time. However, this systematically improvable method is computationally very demanding and thus typically used for small systems (up to 10 electrons) or for small active spaces only. Another multi-determinant approach is the time-dependent configuration interaction theory (TD-CI) [22–27], where only the coefficients are propagated in time while the configurations are stationary. Like MCTDHF but unlike TD-DFT, this method can be improved systematically by including more and more excitations explicitly (singles [TD-CIS], singles and doubles [TD-CISD], and higher), or within perturbation theory (TD-CIS(D) or TD-CISD(T)). With TD-CIS, also larger systems can be treated. Another advantage of time-dependent methods in general is that they treat laser fields explicitly and can describe non-linear processes of arbitrary order (in contrast to the time-dependent perturbation theory (TD-PT)) [28]. The TD-CIS approach was also extended to strong-field interactions of closed-shell atoms in presence of a complex absorbing potential by Santra and coworkers [29].

Electron movement can be induced by ultrashort laser pulses. One possible result are electronic or excitonic wavepackets, either intramolecular (shown by Krause and coworkers [30–32]) or intermolecular [33]. Also, stimulated emission [33] or a switch of a permanent dipole moment is possible due to state-to-state transitions [31–34]. Breidbach and Cederbaum demonstrated the possibility of charge migration [35], and Barth and Manz modeled ring currents [36].

Some other processes cannot be described by the standard implementations of MCTDHF or TD-CI which usually employ the fixed nuclei approximation and atom-centered atomic orbital-like basis sets and are based on the non-relativistic electronic Schrödinger equation. (A fully quantum mechanical MCTDHF-type approach to coupled electron nuclear dynamics is given by Nest [37].) Such processes are, *e.g.*, rearrangement of nuclei, or a radiationless decay due to internal conversion or inter-system crossing, and photoionization.

Rearrangement of nuclei occurs, if two different states do not have the same equilibrium geometry. Nuclear motion usually takes place on longer timescales than electronic motion but during longer excitation sequences or propagations the nuclear

motion should be considered in order to describe the system properly. A computational example where coupled electron-nuclear dynamics are treated has been given for the H_2^+ ion [38].

The internal conversion is the radiationless transfer of population from one electronic state to another one of the same spin multiplicity. This happens most probably at intersection points between the potential energy surfaces of two different electronic states. If the two electronic states have different spin multiplicities and are connected through spin-orbit couplings, an intersystem crossing can occur instead.

In this thesis, the fixed nuclei approximation is used. Thus, nuclear motion and internal conversion are not considered within this work. Furthermore, in this work, only optical transitions between singlet states are considered. Therefore, spin-orbit couplings and intersystem crossings are neglected.

The last phenomenon mentioned above is photoionization, which will be treated in this thesis. One can distinguish two types of ionization. The first one is the below-threshold- or tunneling ionization. This type occurs at any photon energy, even far below the ionization potential of a molecular system. It is well described for atoms by the Ammosov-Delone-Krainov (ADK) model [39]. Also, models to calculate the tunneling ionization in molecules were developed [25, 40, 41].

The other type is above-threshold ionization that occurs if the excitation energy (from the ground state) exceeds the ionization potential. For molecules in intense laser fields, this may be the dominating ionization process. First, a molecule can ionize because the frequency of the incoming electric field is sufficiently high to transfer the system over the ionization potential (IP). Second, if a laser pulse is short, the spectral width of the pulse is broadened. Hence, also states above the IP are populated even if the carrier frequency is smaller than the IP. Third, if a laser pulse or a continuous wave electric field is very intense, multi-photon excitations are promoted. In the framework of many-electron dynamics to treat photoionization, there are some existing models, *e.g.* for atoms by Scrinzi and Piraux [42], for molecules by Saenz [25, 43], and for model systems employing extended grid basis sets [23]. Furthermore, ionization spectra can be calculated using the algebraic diagrammatic construction (ADC) approach by Cederbaum and coworkers [44]. In this work, a rather heuristic approach is presented and tested, which relies on standard atom-centered Gauss-type basis sets.

A very powerful technique in today’s laser physics is the pump-probe experiment [45–50]. This means, a first pulse excites the system to a target state (electronic [46], vibrational [48], or vibronic) or – more often – creates a wave packet. After a certain delay time a second pulse is applied to the system. This pulse induces a response signal, for instance, a fluorescence signal [47,49], ionized matter that can be analyzed in a mass spectrometer, or photoelectrons [50]. The response depending on the delay time is related to the time evolution of the system after the first pulse. Hence, pump-probe spectroscopy is used for the analysis and control of ultrafast physical and chemical processes. It is a challenge to describe these pump-probe processes theoretically, a problem which will be treated in this work.

Further in this work, electronic wave packets are generated in systems with electronically excited charge transfer states. Time-dependent density functional theory (TD-DFT) – in most cases formulated in the linear response regime [51, 52] – is not capable of describing the R -dependence properly for most functionals [52–58]. This is due to a lack of Hartree-Fock-like exchange. TD-CI methods account for an “exact” exchange and they are more appropriate methods to treat systems with long-range charge transfer states.

Furthermore, if a system is excited photophysically, this usually leads to a change of its molecular properties. Excited electronic states are dominated by different electron configurations. This leads, for instance, to a higher total energy of the system. Also, the electron distribution and thus the dipole moment of the molecule is changed. It is an interesting challenge to control such properties on ultra-fast timescales using laser pulses, which will also be attempted in this thesis.

Another property of interest for physicists and chemists is the entropy, which is important for many processes. Here, we investigate the time evolution of the “single electron entropy” derived from the many electron wavefunction. The time-dependent wavefunction arising from a TD-CI or MCTDHF calculation is taken in order to build a reduced one-electron density matrix. From this density matrix $\underline{\underline{\gamma}}$, the time-dependent “single electron entropy” of the system can be defined according to von Neumann as $S = -k_B \text{Tr}\{\underline{\underline{\gamma}} \ln \underline{\underline{\gamma}}\}$ [59], where k_B is Boltzmann’s constant and Tr denotes a trace. Conceptually, the single electron entropy is rather interesting, because it can be linked to correlation. In quantum chemistry, the correlation energy is defined as the difference between the exact non-relativistic ground state energy and the Hartree-Fock ground state energy at the basis set limit. Obviously, it is

hard to generalize this concept to a time-dependent picture. However, as a single determinant wavefunction, *i.e.*, an uncorrelated state, has always zero single electron entropy, the time-dependent single electron entropy can be taken as a measure for correlation. We do not only aim for computing the time-dependent single electron entropy but also an attempt is made to decrease the single electron entropy of a given system photophysically using optimally shaped laser pulses. Another approach to quantify electron correlation in a time-dependent scheme has been suggested by Kato and Kono [60].

This thesis is organized as follows: In chapter 2, methods used in this thesis are described. First, some aspects of Hartree-Fock theory and the post-Hartree-Fock methods applied in this work (CI, CASSCF) are recalled. Their time-dependent variants (TD-CI, MCTDHF) are then introduced. A heuristic model is presented that is capable of treating photoionization within the time-dependent configuration interaction theory. This model is extended to dissipation in order to treat laser-driven electron dynamics of molecules in electron-rich environments including photoionization. Also, the possibility of transforming a time-dependent wavefunction into a reduced one electron density matrix and calculating an entropy from it is demonstrated. Finally, in this section, laser pulses and optimization methods are presented in order to obtain maximal yields in target states, or minimal single electron entropies.

In chapter 3, effects of ionization are considered. It is shown for a first model system (LiCN) whether excitations to states below or above the ionization potential are efficient and selective. Also, a pump-probe simulation is performed and it is argued that this model is expected to be useful for the experimental detection of electronic wavepackets in molecular systems. As a second example, a molecule which does not undergo substantial geometrical changes in the involved excited state is also presented and a corresponding pump-probe simulation is shown. Some results of this simulation are analyzed in detail. As a result, an optimized pump-probe scheme is derived. A further aspect in this section is the effect of photoionization on the dynamic polarizability which is demonstrated for the H_2 molecule. For this molecule, simulations of state-to-state excitations in an electron-rich environment are also presented.

In chapter 4, attempts to control electron correlation by laser pulses are reported. First, the close correspondence between the correlation energy and other correlation

measures, *e.g.*, the single electron entropy, is demonstrated for H_2 , first for a minimal basis, then for extended basis sets. It is shown for the H_2 molecule, how well the correlation energy can be described by different correlated wavefunction-based methods. The time-dependent single electron entropy is calculated (also upon laser pulse excitation). Further, several attempts are made in order to decrease the single electron entropy, and thus decorrelate the electrons of a system, photophysically.

Chapter 5 concludes this thesis and gives some proposals for future work. If not stated otherwise, all values are given in atomic units ($\hbar = m_e = e = 4\pi\epsilon_0 = 1$). The units are, however, sometimes mentioned for clarity.

Chapter 2

Theoretical foundations and methods

2.1 Stationary quantum chemistry

In this section, several time-independent electronic structure methods are recalled. These methods are presented because analogous time-dependent wavefunctions are used to simulate the electron dynamics.

2.1.1 The time-independent Schrödinger equation

The basic equation of stationary quantum mechanics in a non-relativistic wavefunction-based picture is the time-independent Schrödinger equation [13–16]

$$\hat{H}\Psi_i = E_i\Psi_i \quad (2.1)$$

with the eigenenergies E_i and the eigenfunctions Ψ_i . The Hamiltonian \hat{H} which is a molecular Hamiltonian \hat{H}_{mol} here, for a system consisting of N electrons and N_A nuclei

$$\hat{H}_{mol} \equiv \hat{T}_{el} + \hat{V}_{el,el} + \hat{T}_{nuc} + \hat{V}_{el,nuc} + \hat{V}_{nuc,nuc} \quad (2.2)$$

is described as the sum of the kinetic energy operator of the electrons

$$\hat{T}_{el} = -\frac{1}{2} \sum_{i=1}^N \nabla_i^2 \quad , \quad (2.3)$$

the electron-electron potential energy operator

$$\hat{V}_{el,el} = \sum_{i=1}^N \sum_{j>i}^N \frac{1}{r_{ij}} \quad , \quad (2.4)$$

the kinetic energy operator of the nuclei

$$\hat{T}_{nuc} = - \sum_{A=1}^{N_A} \frac{1}{2M_A} \nabla_A^2 \quad , \quad (2.5)$$

the electron-nuclei potential energy operator

$$\hat{V}_{el,nuc} = - \sum_{i=1}^N \sum_{A=1}^{N_A} \frac{Z_A}{r_{iA}} \quad , \quad (2.6)$$

and the nuclei-nuclei potential energy operator

$$\hat{V}_{nuc,nuc} = \sum_{A=1}^{N_A} \sum_{B>A}^{N_A} \frac{Z_A Z_B}{R_{AB}} \quad . \quad (2.7)$$

In these equations, small indices stand for electrons and capital indices for nuclei. r_{ij} is the distance between the electrons i and j , r_{iA} is the distance between electron i and nucleus A , and R_{AB} is the distance between the nuclei A and B . M_A stands for the mass of nucleus A and Z_A for its charge.

Next, the wavefunction is written as a product of an electronic wavefunction Ψ_{el} , which depends only parametrically on the nuclear coordinates, and a nuclear wavefunction Ψ_{nuc}

$$\Psi(\{\underline{r}_i\}, \{\underline{R}_A\}) = \Psi_{el}(\{\underline{r}_i\}; \{\underline{R}_A\}) \cdot \Psi_{nuc}(\{\underline{R}_A\}) \quad , \quad (2.8)$$

and an electronic Schrödinger equation can be written as

$$\hat{H}_{el}|\Psi_{el}\rangle = (\hat{T}_{el} + \hat{V}_{el,el} + \hat{V}_{el,nuc})|\Psi_{el}\rangle = E_{el}|\Psi_{el}\rangle \quad . \quad (2.9)$$

The electronic wavefunction can be obtained by solving equation (2.9) with nuclear positions held fixed. This approximation – namely the Born-Oppenheimer approximation [61] – is usually valid because electron motion often takes place on much shorter timescales (within some femtoseconds or even below) than nuclear motion (more than 10 fs). Nuclear motion as in photoisomerizations, for example, however, can be induced by electronic transitions.

2.1.2 The Hartree-Fock method

The electronic Schrödinger equation (equation (2.9)) can only be solved exactly for few-electron systems, and approximate methods are needed in more general cases.

In the framework of the Hartree-Fock theory [7, 8], the wavefunction for a many-electron system is approximated as a Slater determinant [62]

$$|\Psi_{el}\rangle = |\Psi_0^{HF}\rangle = \frac{1}{\sqrt{N!}} \begin{vmatrix} \chi_1(\underline{x}_1) & \chi_2(\underline{x}_1) & \cdots & \chi_N(\underline{x}_1) \\ \chi_1(\underline{x}_2) & \chi_2(\underline{x}_2) & \cdots & \chi_N(\underline{x}_2) \\ \vdots & \vdots & \ddots & \vdots \\ \chi_1(\underline{x}_N) & \chi_2(\underline{x}_N) & \cdots & \chi_N(\underline{x}_N) \end{vmatrix} \quad (2.10)$$

with $\chi_j(\underline{x})$ as the single electron wavefunction, *i.e.*, the spin orbital j . The spin orbitals depend on the electron coordinates \underline{x} comprising a spatial coordinate \underline{r} and a spin coordinate ω . Within the restricted Hartree-Fock (RHF) ansatz, the spin orbitals χ_j and χ_{j-1} ($j > 1$) are then written as a product of a spatial orbital ψ_i and a spin function which is one for α (if the spin quantum number is $+\frac{1}{2}$) or for β (if the spin quantum number is $-\frac{1}{2}$) for electrons

$$\chi_j(\underline{x}) = \chi_j(\underline{r}, \omega) = \begin{cases} \psi_i(\underline{r}) \cdot \alpha(\omega) & \text{if } j = 2i - 1 \\ \psi_i(\underline{r}) \cdot \beta(\omega) & \text{if } j = 2i \end{cases} . \quad (2.11)$$

Here, non-italic indices are used for spin orbitals while italic indices indicate spatial orbitals.

The spin orbitals are determined from the variational principle. The variational principle states that the eigenenergy for a test function $\tilde{\Psi}$ can be either greater than the exact energy E_0^{exact} (if the test function is not the exact solution), or equal to it (if the test function is the exact wavefunction). The most suitable wavefunction is found by minimizing the energy

$$E_0^{exact} \leq \langle \tilde{\Psi} | \hat{H}_{el} | \tilde{\Psi} \rangle \stackrel{!}{=} \min . \quad (2.12)$$

If the energy of a Slater determinant is minimized under the condition that the single electron wavefunctions are orthonormal, *i.e.*,

$$\langle \chi_i | \chi_j \rangle = \delta_{ij} , \quad (2.13)$$

one obtains the Hartree-Fock equations which are coupled effective single electron equations that are used in order to determine the spin orbitals

$$\hat{f}(\underline{x}_1) \chi_a(\underline{x}_1) = \varepsilon_a \chi_a(\underline{x}_1) \quad \text{with } a = 1, \dots, \infty . \quad (2.14)$$

In this equation, ε_a stands for the orbital energy of the spin orbital $\chi_a(\underline{x}_1)$. $\hat{f}(\underline{x}_1)$ is the Fock operator which is written as the sum of a core Hamiltonian (describing

the kinetic energy of the electrons and the electron-nuclei interaction), an operator describing the Coulomb interaction between electrons, and another operator giving the description of an exchange interaction between electrons with parallel spin.

These equations lead to an infinite number of solutions χ_a (molecular orbitals or MOs) with their respective energies ε_a . In practice, a finite basis (K basis functions) is introduced – see below. Due to the two spin directions, this limits the number of solutions to $2K$. Among these solutions, there are N occupied and $2K - N$ unoccupied (virtual) spin orbitals. One can reformulate the Hartree-Fock equations (equation (2.14)) for a closed-shell system (all spatial orbitals are doubly occupied or unoccupied) by integrating over the spin function. These Hartree-Fock equations contain only the spatial orbitals ψ_i and the spatial coordinates \underline{r}

$$\hat{f}(\underline{r}_1)\psi_j(\underline{r}_1) = \varepsilon_j\psi_j(\underline{r}_1) \quad j = 1, \dots, K \quad . \quad (2.15)$$

Also, a reformulation of the Fock operator, the Coulomb operator, and the exchange operator is required.

There is an analogous algorithm to form Hartree-Fock equations for the unrestricted case, *i.e.*, for systems with singly occupied molecular orbitals. This algorithm leads to the Pople-Nesbet equations (see Ref. [63]).

2.1.3 The Roothaan-Hall equation

In order to solve the Hartree-Fock equations (equation (2.15)) numerically the molecular orbitals ψ_i are written as a linear combination of atomic orbitals ϕ_μ (LCAO-MO) with respective coefficients $C_{\mu i}$. In principle, also other basis sets like plane waves, extended grids etc. can be used. For electronic structure calculations for molecular systems, atom-centered contracted Gauss-type atomic orbitals have been most successful and will be also used within this thesis. These atomic orbitals form the basis; we thus write

$$\psi_i(\underline{r}) = \sum_{\mu=1}^K C_{\mu i} \phi_\mu(\underline{r}) \quad . \quad (2.16)$$

Thus the Hartree-Fock-Roothaan, or Roothaan-Hall equation [64,65] in matrix form is

$$\underline{\underline{F}} \underline{\underline{C}} = \underline{\underline{S}} \underline{\underline{C}} \underline{\underline{\varepsilon}} \quad . \quad (2.17)$$

Here, $\underline{\underline{F}}$ stands for the Fock matrix

$$(\underline{\underline{F}})_{\mu\nu} = \langle \phi_\mu | \hat{f} | \phi_\nu \rangle \quad , \quad (2.18)$$

the matrix $\underline{\underline{C}} = (\underline{C}_1, \underline{C}_2, \dots, \underline{C}_K)$ contains the LCAO-MO coefficients $C_{\mu i}$ (as in equation (2.16)). $\underline{\underline{\varepsilon}}$ is a diagonal matrix containing the energies of the molecular orbitals ($(\underline{\underline{\varepsilon}})_{ij} = \varepsilon_i \delta_{ij}$), and $\underline{\underline{S}}$ the overlap between two atomic orbitals ($(\underline{\underline{S}})_{\mu\nu} = \langle \phi_\mu | \phi_\nu \rangle$). The Fock matrix

$$(\underline{\underline{F}})_{\mu\nu} = (\underline{\underline{H}})_{\mu\nu} + (\underline{\underline{G}})_{\mu\nu} \quad (2.19)$$

can be written as the sum of a one-electron matrix

$$(\underline{\underline{H}})_{\mu\nu} = \langle \phi_\mu | -\frac{1}{2}\Delta | \phi_\nu \rangle - \sum_{A=1}^{N_A} \langle \phi_\mu | \frac{Z_A}{r_{iA}} | \phi_\nu \rangle \quad (2.20)$$

and a two-electron matrix, given for closed shells as

$$(\underline{\underline{G}})_{\mu\nu} = \sum_{\sigma} \sum_{\lambda} (\underline{\underline{P}})_{\lambda\sigma} \left[\langle \phi_\mu \phi_\sigma | \phi_\nu \phi_\lambda \rangle - \frac{1}{2} \langle \phi_\mu \phi_\sigma | \phi_\lambda \phi_\nu \rangle \right] \quad (2.21)$$

The one-electron matrix $\underline{\underline{H}}$ contains the kinetic energy of the electrons and the electron-nuclei interaction. The two electron matrix $\underline{\underline{G}}$ contains the elements of the charge density bond order (CDBO) matrix

$$(\underline{\underline{P}})_{\mu\nu} = 2 \sum_{a=1}^{N/2} C_{\mu a} C_{\nu a}^* \quad (2.22)$$

and two-electron integrals

$$\langle \phi_\mu \phi_\sigma | \phi_\nu \phi_\lambda \rangle = \iint d\mathbf{r}_1 d\mathbf{r}_2 \phi_\mu^*(\mathbf{r}_1) \phi_\sigma^*(\mathbf{r}_2) \frac{1}{r_{12}} \phi_\nu(\mathbf{r}_1) \phi_\lambda(\mathbf{r}_2) \quad (2.23)$$

The Fock matrix depends on the coefficient vectors $\{\underline{C}_j\}$. Thus, the set of equations cannot be solved trivially. The Hartree-Fock-Roothaan equations

$$\underline{\underline{F}} \{\underline{C}_j\} \underline{C}_j = \varepsilon_j \underline{\underline{S}} \underline{C}_j \quad (2.24)$$

can be solved by the well-known self-consistent field (SCF) method [63]. The results are – amongst others – a converged Hartree-Fock wavefunction $|\Psi_0^{HF}\rangle$ and the respective electronic energy for the ground state E_0^{HF} .

2.1.4 Electron correlation

The Hartree-Fock theory contains several approximations (neglect of electron correlation, Born-Oppenheimer approximation, neglect of relativistic effects) and further limitations are introduced in practice (finite basis). Thus, Hartree-Fock calculations do not provide exact results. One of the errors made in HF is the neglect of correlation energy

$$E_{corr} = E_0^{exact,BO} - E_0^{HF,limit} \quad (2.25)$$

that is approximately -1 eV for each electron (according to a rule of thumb) and thus in the range of chemical binding energies. In this equation, $E_0^{HF,limit}$ is the Hartree-Fock ground state energy for a complete basis and $E_0^{exact,BO}$ is the exact ground state energy within the Born-Oppenheimer approximation.

One typically distinguishes between two different types of electron correlation: the dynamic correlation and the non-dynamic (static) correlation [66]. The non-dynamic correlation occurs if the total wavefunction is not dominated by a single Slater determinant. This is the case if there are some resonant electron configurations for one molecule that are quasi-degenerate.

The other type of correlation is dynamic correlation. This type arises from the fact that a single electron in Hartree-Fock theory is not influenced by another single electron, but by the average field of all the other electrons. Dynamic correlation is the type of correlation leading to dispersion bonds, *e.g.*, in noble gas dimers.

In the following, two types of post-Hartree-Fock methods are described that include electron correlation. The first one is the configuration interaction method (CI, in Sec. 2.1.5), the second one is the complete active space self-consistent field method (CASSCF, in Sec. 2.1.6).

2.1.5 Configuration Interaction (CI)

One method to minimize the error due to electron correlation (or even to make it vanish) is configuration interaction [67]. While the Hartree-Fock theory includes only a single Slater determinant (the ground state configuration), CI includes in addition also other possible configurations. Depending on the CI method, one considers only single excitations (CIS, S=Singles), double excitations (CID, D=Doubles), both of them (CISD), or even all possible excitations (Full-CI), *i.e.*, up to N -fold excitations in an N -electron system. It can be shown that the Full-CI result is the exact solution within the Born-Oppenheimer approximation for the respective basis set. The total CI wavefunction is a linear combination of all these configurations:

$$\begin{aligned} |\Psi^{CI}\rangle = & D_0|\Psi_0^{HF}\rangle + \sum_a \sum_r D_a^r |\Psi_a^r\rangle + \sum_{a<b} \sum_{r<s} D_{ab}^{rs} |\Psi_{ab}^{rs}\rangle \\ & + \sum_{a<b<c} \sum_{r<s<t} D_{abc}^{rst} |\Psi_{abc}^{rst}\rangle + \dots \end{aligned} \quad (2.26)$$

Here, $|\Psi_0^{HF}\rangle$ is the ground state Hartree-Fock wavefunction, $|\Psi_a^r\rangle$ is the wavefunction for the configuration when one electron is excited from the occupied spin orbital a

to the virtual spin orbital r , and D_a^r is the appropriate coefficient. These coefficients are determined from a variational calculation using the secular equations

$$\underline{\underline{H}} \underline{\underline{D}}_i = E_i \underline{\underline{D}}_i \quad (2.27)$$

with the elements of the Hamiltonian matrix

$$(\underline{\underline{H}})_{IJ} = \langle \Psi_I | \hat{H}_{el} | \Psi_J \rangle \quad . \quad (2.28)$$

In this equation, Ψ_I and Ψ_J are Slater determinants which occur in equation (2.26). The results of equation (2.27) are a corrected ground state energy and wavefunction and also the energies and wavefunctions of excited states. A Full-CI calculation is technically not feasible for most systems. Therefore, the CI wavefunction is often truncated, taking only excitations up to single electron excitations or the excitation of two electrons (CISD) into account. As a further simplification, Slater determinants are not used here, but spin-adapted linear combinations of these, the so-called configuration state functions (CSFs) [68].

As already mentioned, there are two types of correlation. CI methods describe dynamical correlation well and cover the most important effects of static correlation [66].

Although the CI theory is a systematically improvable method that is capable of describing electron correlation, there are some disadvantages of this method. If the CI wavefunction is truncated, the size consistency is not given any more. If higher excitations than single electron transitions are considered, the scaling increases to non-tractable dimensions. According to a rule of thumb, CI methods scale with K^{2m+2} where K is the number of orbitals taken into account and m is the order of the highest excitation (1 for CIS, 2 for CISD, etc.). The CIS method that can be applied to larger systems, however, does not include any correlation of the electronic ground state.

2.1.5.1 Configuration Interaction Singles (CIS)

The total wavefunction within the CIS [69] method includes additionally to the Hartree-Fock ground state determinant the Slater determinants of all possible single electron excitations. The singlet CSF of a single excitation can be written as

$$|^1\Psi_a^r\rangle = \frac{1}{2} (|\Psi_a^r\rangle + |\Psi_a^{\bar{r}}\rangle) \quad . \quad (2.29)$$

In this equation, $|\Psi_a^r\rangle$ stands for the excitation of an α electron from the occupied spatial orbital a to the virtual spatial orbital r . $|\Psi_a^{\bar{r}}\rangle$ is the same for a β electron. Note, that only singlet CSFs are considered here.

This method does not lead to a change of the ground state energy. According to Brillouin's theorem [70], the off-diagonal elements in the first row and column of the Hamiltonian matrix (these elements stand for the coupling between the HF ground state and the possible configuration with single electron excitations) are all zero, so the CIS ground state wavefunction is equal to the Hartree-Fock wavefunction and is thus not correlated. The method provides excited states which are partly correlated. The total number of states n_{st} which can be computed is calculated from

$$n_{st} = 1 + (n_o - n_{fc}) \cdot (n_v - n_{fv}) \quad , \quad (2.30)$$

where n_o is the number of occupied spatial orbitals and n_v is the number of virtual spatial orbitals. n_{fc} (fc = frozen core) and n_{fv} (fv = frozen virtuals) are the numbers of very low-lying (fc) or very high-energetic (fv) spatial orbitals which are neglected in the single excitations. The one additional state is the ground state. Here, we usually set $n_{fv} = 0$ and n_{fc} equal to the number of MOs, that correspond to the non-valence AOs, *e.g.*, the 1s-orbitals in the case of second-row atoms.

2.1.5.2 Configuration Interaction Singles Doubles (CISD)

Within this method, also double excitations are used to form the total wavefunction. Therefore, also the following CSFs are important [63]:

$$\begin{aligned} |\Psi_{aa}^{rr}\rangle &= |\Psi_{aa}^{r\bar{r}}\rangle \quad , \\ |\Psi_{aa}^{rs}\rangle &= \frac{1}{\sqrt{2}} (|\Psi_{aa}^{r\bar{s}}\rangle + |\Psi_{aa}^{\bar{r}s}\rangle) \quad , \\ |\Psi_{ab}^{rr}\rangle &= \frac{1}{\sqrt{2}} (|\Psi_{ab}^{r\bar{r}}\rangle + |\Psi_{ab}^{\bar{r}r}\rangle) \quad , \\ |\Psi_{ab}^{rs}\rangle &= \frac{1}{\sqrt{12}} (2|\Psi_{ab}^{rs}\rangle + 2|\Psi_{ab}^{r\bar{s}}\rangle - |\Psi_{ab}^{\bar{s}r}\rangle + |\Psi_{ab}^{\bar{r}s}\rangle + |\Psi_{ab}^{r\bar{s}}\rangle - |\Psi_{ab}^{\bar{s}r}\rangle) \quad , \\ |\Psi_{ab}^{rs}\rangle &= \frac{1}{2} (|\Psi_{ab}^{\bar{s}r}\rangle + |\Psi_{ab}^{\bar{r}s}\rangle + |\Psi_{ab}^{r\bar{s}}\rangle + |\Psi_{ab}^{s\bar{r}}\rangle) \quad . \end{aligned} \quad (2.31)$$

The total number of states n_{st} is calculated from

$$n_{st} = 1 + \frac{(n_o - n_{fc})(n_v - n_{fv})}{2} [3 + (n_o - n_{fc})(n_v - n_{fv})] \quad . \quad (2.32)$$

where n_{fv} and n_{fc} are chosen in the same way as for CIS.

In contrast to CIS, the ground state in CISD is not only described by the Hartree-Fock ground state Slater determinant, but by a linear combination of different configuration state functions. This leads to correlation in the electronic ground state and thus to a correction of the ground state energy. However, this ground state energy is not size-consistent if more than two electrons are present.

2.1.6 The Complete Active Space Self-Consistent Field (CASSCF) method

Another post-Hartree-Fock method that is capable of including correlation in the ground state wavefunction is the complete active space self-consistent field (CASSCF) method [20]. This method is very similar to Full-CI with some restrictions. There, in an active space of n orbitals (including occupied and virtual orbitals), all possible configurations with the m electrons within the active space are used to find a suitable ground state energy. These configurations are built from all single-electron excitations, two-electron excitations and higher excitations and their respective configurations. However, in contrast to a CAS-CI calculation, not only the coefficients of the electron configurations, *e.g.*, D_a^r , but also the orbitals forming these configurations, *i.e.*, the AO coefficients $C_{\mu i}$ are optimized with respect to a minimal energy. The notation for CASSCF is CASSCF(m,n), meaning the treatment of m electrons in a space of n active spatial orbitals. The number of configurations used in a CASSCF calculation can be calculated from

$$n_{conf} = \binom{2n}{m} . \quad (2.33)$$

The CASSCF method behaves differently compared to CI as far as the two types of correlation are regarded. While static correlation is well described by CASSCF, the description of dynamic correlation is not sufficient, at least for numerically tractable active spaces.

2.2 Quantum electron dynamics in a laser field

In order to simulate many-electron dynamics within the fixed nuclei approximation, time-dependent methods have to be applied. These methods are explained in the next sections. The time-independent methods presented in the previous sections are used as a basis for their time-dependent variants.

2.2.1 The time-dependent electronic Schrödinger equation

A central postulate of quantum mechanics is the time-dependent Schrödinger equation [13–16]

$$i\hbar \frac{\partial \Psi(\{\underline{x}_i\}, t)}{\partial t} = \hat{H}(t) \Psi(\{\underline{x}_i\}, t) \quad . \quad (2.34)$$

In the present context the time-dependent Hamiltonian $\hat{H}(\{\underline{x}_i\}, t)$ is the sum of the electronic Hamiltonian of the unperturbed system \hat{H}_{el} (which is not time-dependent, but it depends on the spatial coordinates of the electrons, $\{\underline{r}_i\}$) and an operator $\hat{W}(\{\underline{r}_i\}, t)$ describing the interaction between the molecule and the laser field

$$\hat{H}(\{\underline{r}_i\}, t) = \hat{H}_{el}(\{\underline{r}_i\}) + \hat{W}(\{\underline{r}_i\}, t) \quad . \quad (2.35)$$

In equation (2.35), any dependencies on spin coordinates have been neglected. A description for the interaction operator $\hat{W}(t)$ is derived as follows. In a classical picture a particle (with the charge q , the mass m , the velocity \underline{v} , and neglected spin) in an electromagnetic field consisting of an electric field $\underline{F}(\underline{r}, t)$ and a magnetic field $\underline{B}(\underline{r}, t)$, is influenced by an electrostatic force and the Lorentz force

$$\underline{K} = q\underline{F} + q\underline{v} \times \underline{B} \quad . \quad (2.36)$$

The corresponding classical Hamiltonian is given as

$$H(t) = \frac{1}{2m}(\underline{p} - q\underline{A})^2 + q\phi + V_s \quad . \quad (2.37)$$

In the semiclassical approximation (*i.e.*, the particle being treated quantum mechanically and the field classically), the corresponding quantum expression is

$$\hat{H}(t) = \frac{1}{2m}(\hat{\underline{p}} - q\underline{A})^2 + q\phi + V_s \quad . \quad (2.38)$$

with the momentum operator

$$\hat{\underline{p}} = \frac{\hbar}{i} \underline{\nabla} \quad , \quad (2.39)$$

the electrostatic potential ϕ and the vector potential \underline{A} . The connection between fields and potentials are

$$\underline{F}(\underline{r}, t) = -\underline{\nabla}\phi - \frac{\partial \underline{A}}{\partial t} \quad \text{and} \quad (2.40)$$

$$\underline{B}(\underline{r}, t) = \underline{\nabla} \times \underline{A} \quad . \quad (2.41)$$

Further, V_s is indicating an additional static potential, *e.g.*, the electron-nuclei attraction in molecules. Equation (2.37) can also be written as the sum of a Hamiltonian of the unperturbed system

$$\hat{H} = -\frac{\hbar^2}{2m}\nabla^2 + q\phi + V_s \quad (2.42)$$

and the interaction operator

$$\hat{W}(\underline{r}, t) = \frac{i\hbar q}{2m}(\nabla \cdot \underline{A} + \underline{A} \cdot \nabla) + \frac{q^2}{2m}\underline{A} \cdot \underline{A} \quad . \quad (2.43)$$

This can be simplified to (with the Coulomb gauge $\nabla \cdot \underline{A} = 0$):

$$\hat{W}(\underline{r}, t) = -\frac{q}{m}(\underline{A} \cdot \hat{\underline{p}}) + \frac{q^2}{2m}\underline{A} \cdot \underline{A} \quad . \quad (2.44)$$

For weak fields, the second term can be neglected. For a periodic field with an amplitude \underline{A}_0 , a wave vector $|\underline{k}| = \frac{2\pi}{\lambda}$ (with λ as the wavelength), and a frequency ω

$$\underline{A}(\underline{r}, t) = \underline{A}_0 \cos(\underline{k} \cdot \underline{r} - \omega t) \quad , \quad (2.45)$$

the interaction operator is written as

$$\hat{W}(\underline{r}, t) = -\frac{q}{m}\underline{A}_0 \cdot \frac{1}{2} \left[e^{i\underline{k} \cdot \underline{r}} e^{-i\omega t} + e^{-i\underline{k} \cdot \underline{r}} e^{i\omega t} \right] \hat{\underline{p}} \quad . \quad (2.46)$$

If the wavelength of the electric field is much longer than the size of the molecule, *i.e.*, $\lambda \gg |\underline{r}|$ (this is valid for UV/Vis spectroscopy and many other spectroscopies), the semiclassical dipole approximation [71] can be applied. Within this approximation, the exponential functions containing the \underline{r} -dependence are expanded in a Taylor series that is truncated after the constant term ($e^{\pm i\underline{k} \cdot \underline{r}} \approx 1$). The interaction operator then becomes

$$\hat{W}(t) = -\frac{q}{m}\underline{A}_0 \cos(\omega t) \hat{\underline{p}} = -\hat{\underline{\mu}} \underline{F}_0 \cos(\omega t) \quad . \quad (2.47)$$

This means that the interaction is not dependent of the magnetic field and the spatial dependence of the electric field is also neglected, *i.e.*, $\underline{E}(\underline{r}, t) \approx \underline{E}_0 \cdot \cos(\omega t)$ in the periodic case. For arbitrary fields $\underline{E}(t)$, equation (2.47) becomes $\hat{W}(t) = -\hat{\underline{\mu}} \underline{E}(t)$.

For a molecular system, the dipole operator $\hat{\underline{\mu}}$ is written as the sum of an electronic dipole operator $\hat{\underline{\mu}}_{el}$ and a nuclear dipole operator $\hat{\underline{\mu}}_{nuc}$

$$\hat{\underline{\mu}} = \hat{\underline{\mu}}_{el} + \hat{\underline{\mu}}_{nuc} = -\sum_{i=1}^N \underline{r}_i + \sum_{A=1}^{N_A} Z_A \cdot \underline{R}_A \quad . \quad (2.48)$$

Here, the second sum enters as a constant, as we work in the fixed nuclei approximation. In order to simulate correlated many-electron dynamics in molecular systems the time-dependent Schrödinger equation (equation (2.34)) has to be solved. For this purpose, two time-dependent methods are used that are explained in detail in the following sections: The time-dependent configuration interaction theory (Sec. 2.2.2) based on CI (see Sec. 2.1.5), and the multi-configuration time-dependent Hartree-Fock method (Sec. 2.2.3) based on CASSCF (see Sec. 2.1.6).

2.2.2 Time-dependent Configuration Interaction (TD-CI)

One possible way to solve the time-dependent electronic Schrödinger equation is a multi-determinant approach. In the case of time-dependent configuration interaction (TD-CI) methods [22–27, 30–34, 72], only the coefficients Θ_i of the CI states are time-dependent, the CI states themselves Φ_i and thus the electron configurations forming these states remain stationary. If also the orbitals forming the electron configurations are assumed to be time-dependent, this results in the multi-configuration time-dependent Hartree-Fock method (MCTDHF) [17–19]. The electronic wavefunction within the TD-CI method is written as

$$\Psi(t) = \sum_i \Theta_i(t) \Phi_i \quad , \quad (2.49)$$

where Φ_i is the electronic wavefunction of the state i , *e.g.*, in the TD-CIS case

$$\Phi_i = D_{0,i} |\Psi_0\rangle + \sum_a \sum_r D_{a,i}^r |\Psi_a^r\rangle \quad . \quad (2.50)$$

Here, $D_{a,i}^r$ is the coefficient for the electron configuration where a single electron has been excited from the occupied orbital a to the virtual orbital r within the state i , and $D_{0,i}$ is the coefficient of the Hartree-Fock state. The D_i s are obtained from equation (2.27). In this case, the coefficients have to be propagated in time. Bandrauk *et al.* [73] developed an algorithm that is used for this propagation. Accordingly, we write

$$\underline{\Theta}(t + \Delta t) = \left[\prod_{q=x,y,z} \underline{U}_q^\dagger e^{iF_q(t)\underline{\mu}_q \Delta t} \underline{U}_q \right] e^{-i\tilde{H}\Delta t} \underline{\Theta}(t) \quad . \quad (2.51)$$

Here, $\underline{\Theta}(t)$ is a vector containing all coefficients $\Theta_i(t)$, \tilde{H} is a diagonal Hamiltonian matrix in the basis of the CI eigenstates containing the energies E_i , \underline{U}_q is a unitary

matrix which transforms the wavefunction from the basis of CI eigenstates into a basis in which the dipole matrix $\underline{\underline{\mu}}$ is diagonal.

When the laser is switched off, this propagation can be simplified to

$$\underline{\Theta}(t + \Delta t) = e^{-i\underline{\underline{H}}\Delta t}\underline{\Theta}(t) \quad . \quad (2.52)$$

The populations of the eigenstates, which are also time-dependent if the laser pulse is on, can be determined by calculating the square of the absolute of the respective coefficients:

$$P_i(t) = |\Theta_i(t)|^2 = |\langle \Phi_i | \Psi(t) \rangle|^2 \quad . \quad (2.53)$$

Another observable of interest is the time-dependent dipole moment. The latter can be calculated as

$$\mu_q(t) = \langle \Psi(t) | \hat{\mu}_q | \Psi(t) \rangle \text{ with } q = x, y, z \quad . \quad (2.54)$$

As the dipole operator contains the electron positions, the time-dependent dipole moment provides information concerning the position expectation value of the electronic wavepacket within the fixed nuclei approximation.

2.2.3 Multi-configuration time-dependent Hartree-Fock (MCTDHF)

Within the multi-configuration time-dependent Hartree-Fock method, the configurations are also time-dependent. The total wavefunction Ψ does not consist exclusively of a superposition of a stationary basis of electron configurations with time-dependent coefficients but of a superposition of time-dependent electron configurations $\Psi_I(t)$ with time-dependent coefficients $\Lambda_I(t)$. The wavefunction can now be written as

$$\Psi(t) = \sum_{I=1}^{n_{conf}} \Lambda_I(t) \Psi_I(t) \quad . \quad (2.55)$$

Here, n_{conf} is the number of configurations taken into account according to equation (2.33). The configurations are written as a Slater determinant including spin orbitals χ_i :

$$\Psi_I = |\chi_{i_1} \chi_{i_2} \cdots \chi_{i_N} \rangle \quad . \quad (2.56)$$

The equations of motion for the coefficients Λ_I and the orbitals χ_i are taken from Dirac-Frenkel variational principle [74, 75] and are integrated using an eighth order

Runge-Kutta integrator [76]:

$$\frac{d\Lambda_I}{dt} = -i \sum_J \langle \Psi_I(t) | \hat{H} | \Psi_J(t) \rangle \Lambda_J \quad , \quad (2.57)$$

$$\frac{\partial \chi_j}{\partial t} = -i \sum_{kl} (1 - \hat{P})_{jk} \left((\underline{h})_{kl} + \sum_m (\underline{\rho}^{-1})_{km} (\langle \underline{V}_{el,el} \rangle)_{ml} \right) \chi_l \quad . \quad (2.58)$$

In these equations, $(\underline{h})_{kl}$ is an element of the core Hamiltonian matrix in the representation of spin orbitals. $(\langle \underline{V}_{el,el} \rangle)_{ml}$ is an element of the mean field matrix $\langle \underline{V}_{el,el} \rangle$ describing the Coulomb repulsion between electrons. $(\underline{\rho}^{-1})_{km}$ is an element of the inverse of the reduced one electron density matrix, given in the basis of the time-dependent spin orbitals. \hat{P} is a projector on the space of single particle functions:

$$\hat{P} = \sum_{j=1}^{2K} |\chi_j\rangle \langle \chi_j| \quad . \quad (2.59)$$

The spin orbitals $|\chi_j\rangle$ are represented in an orthogonalized basis set that is derived from standard Gauss-type atomic orbitals. The method is (like CASSCF) systematically improvable by increasing the number of virtual orbitals forming the active space or the number of occupied orbitals within this active space and thus by increasing the number of electrons. The number of electrons m and the number of spatial orbitals n within this active space is written down in the same manner as for CASSCF, *i.e.*, MCTDHF(m, n). If all electrons of a given system are in the active space ($m = N$), there are two limiting cases: A MCTDHF($N, \frac{N}{2}$) calculation is equivalent to time-dependent Hartree-Fock (TD-HF). If the active space consists of all molecular orbitals ($n = K$), this results in MCTDHF(N, K), which is equivalent to TD-Full-CI, analogous to TD-CIS...N.

2.3 Treatment of photoionization

CI methods provide a large number of eigenstates. If atom-centered basis sets are used, most of these states have a large energy which can be above the ionization potential IP according to Koopmans' theorem [77] (see below). In the TD-CI method – as described above – all these states are non-ionizing, *i.e.*, the electrons remain localized at the molecule. This does not correspond to the experimental situation. If higher electronic states are excited, above-threshold ionization is possible. In the heuristic approach for photoionization developed in this thesis, the Hamiltonian

matrix in eigenstate representation $\underline{\tilde{H}}$ from equation (2.51) becomes non-Hermitian:

$$\underline{\tilde{H}} \rightarrow \underline{\tilde{H}} - \frac{i}{2}\underline{\Gamma} \quad . \quad (2.60)$$

Here, $\underline{\Gamma}$ is a diagonal matrix containing the ionization rates Γ_n for the respective states. This results in an exponential decay of population as one can see from the modified propagation equation

$$\underline{\Theta}(t + \Delta t) = \left[\prod_{q=x,y,z} \underline{U}_q^\dagger e^{iF_q(t)\underline{\mu}_q \Delta t} \underline{U}_q \right] e^{-i\underline{\tilde{H}}\Delta t} e^{-\frac{1}{2}\underline{\Gamma}\Delta t} \underline{\Theta}(t) \quad . \quad (2.61)$$

This decay of population can be considered as a model for ionization losses. For the heuristic model to treat this phenomenon, which is presented here (also Ref. [78]), we postulate, that all electronic states below an ionization threshold should have an infinite lifetime. The states above IP have a finite lifetime and decay with an ionization rate Γ_n .

To derive an expression for Γ_n , we first introduce an “escape velocity” v . In a classical picture, v can be defined from an “escape length” \tilde{d} , and an “ionization lifetime” τ as

$$v = \frac{\tilde{d}}{\tau} = \tilde{d}\Gamma \quad , \quad (2.62)$$

where the lifetime τ is equal to the inverse ionization rate Γ .

For a classical electron, the kinetic energy E_{kin} is given as

$$E_{kin} = \frac{1}{2}m_e v^2 \quad , \quad (2.63)$$

where m_e is the mass of the electron. The resulting classical equation for the ionization rate is

$$\Gamma = \frac{\sqrt{2}}{\tilde{d}} \sqrt{\frac{E_{kin}}{m_e}} = \frac{1}{\tilde{d}} \sqrt{\frac{E_{kin}}{m_e}} \quad . \quad (2.64)$$

In this equation, the ionization rates depend only on the kinetic energy of the electron and the modified “escape length” parameter d (that is short for $\frac{\tilde{d}}{\sqrt{2}}$). It is also assumed that once the electron is above IP, it is considered as a free electron with a total energy according to equation (2.63). In the following, we test three different models for the kinetic energy (in Sec. 2.3.1, 2.3.2, and 2.3.3). After that, some remarks concerning the escape length are made (in Sec. 2.3.4).

2.3.1 Eigenenergy algorithm

Within this model, all states below the ionization potential according to Koopmans’ theorem [77] are non-ionizing, *i.e.*, the electrons remain localized at the molecule.

All higher states are ionizing states. As the kinetic energy the eigenenergy of the respective state is chosen, reduced by the Koopmans' ionization potential. If this difference is negative, the state is non-ionizing. The ionization rate is then calculated in the TD-CIS case as

$$\Gamma_n = \begin{cases} 0 & \text{if } E_n^{CIS} - IP < 0 \\ \frac{1}{d} \sqrt{\frac{E_n^{CIS} - IP}{m_e}} & \text{if } E_n^{CIS} - IP \geq 0 \end{cases} \quad (2.65)$$

with E_n^{CIS} being the excitation energy from the ground state to the state $|n\rangle$. IP is the ionization potential according to Koopmans' theorem, *i.e.*, $IP = -\varepsilon_{HOMO}$, where ε_{HOMO} is the energy of the highest occupied Hartree-Fock orbital.

As a higher electronic state usually has a higher eigenenergy (if states are not degenerate), the ionization rate increases monotonically for higher electronic states in this model. On the other hand, excitations from a low-lying orbital to a valence orbital below the vacuum level can be very stable with respect to ionization losses. Therefore, for photoionization, a monotonic behavior of the lifetimes and thus the ionization rates is not desirable.

2.3.2 Configuration State Function (CSF) algorithm

To account for this, an alternative model was tested. Within this model, all states are transferred to the space of configuration state functions. Again we refer to TD-CIS. In CIS, each CSF corresponds to a defined configuration, where one electron has been excited from an occupied spatial orbital a to a virtual spatial orbital r . By definition, all electrons in orbitals with a negative orbital energy are considered as bound, all others are unbound. This algorithm splits the energy difference between the orbitals into two parts. The first part is the energy difference between the occupied orbital a and the energy-zero, *i.e.* in Koopmans' spirit the energy needed for the electron to escape from the molecule,

$$E_{esc} = -\varepsilon_a \quad , \quad (2.66)$$

where ε_a is the energy of the orbital a . The other part, *i.e.*, the energy difference between the energy-zero and the virtual orbital r , is the kinetic energy of the electron

$$E_{kin} = \varepsilon_r \quad . \quad (2.67)$$

If the virtual orbital is still bound (it has a negative orbital energy), this CSF does not contribute to ionization because the escape energy is not reached. These

propositions result in an algorithm to calculate the ionization rate for a CSF as

$$\Gamma_{a,r}^{CSF} = \begin{cases} 0 & \text{if } \varepsilon_r < 0 \\ \frac{1}{d} \sqrt{\frac{\varepsilon_r}{m_e}} & \text{if } \varepsilon_r \geq 0 \end{cases} \quad (2.68)$$

with d being the “escape length” of equation (2.64).

The ionization rate for a CIS eigenstate is then calculated as

$$\Gamma_n = \sum_a \sum_r |D_{a,n}^r|^2 \Gamma_{a,r}^{CSF} \quad (2.69)$$

with $D_{a,n}^r$ as the coefficient for the linear combination of the CSF (excitation $a \rightarrow r$) to the eigenstate Φ_n , and $|D_{a,n}^r|^2$ being the probability that this excitation took place in eigenstate n .

A disadvantage of this algorithm is the low number of non-ionizing states. The ground state in CIS is determined by the Hartree-Fock ground state configuration; the ionization rate is zero. All higher states are formed by a linear combination of several CSFs with a non-vanishing ionization rate. This means, only the ground state is non-ionizing in this picture. All higher states are ionizing, even if their energy is below the IP, which is artificial.

2.3.3 Combined algorithm

As both of the previously mentioned algorithms have advantages and disadvantages, it was also attempted to combine both models. The combination of both models is obtained if the equations (2.65) and (2.69) are combined to

$$\Gamma_n = \begin{cases} 0 & \text{if } E_n^{CIS} < IP \\ \sum_a \sum_r |D_{a,n}^r|^2 \Gamma_{a,r}^{CSF} & \text{if } E_n^{CIS} \geq IP \end{cases} \quad (2.70)$$

with E_n^{CIS} as the excitation energy from the ground state to the state Φ_n .

Using this algorithm, all states below the IP according to Koopmans’ theorem are non-ionizing. A set of stable states besides the electronic ground state is guaranteed. The other states are ionizing, but the ionization rate is not increasing monotonically for higher excited states.

2.3.4 Escape length parameter

All of the three previously introduced algorithms need an “escape length” d after which the electron can be considered as released. The escape length cannot be

obtained from standard quantum chemical calculations. It is not even known if this parameter has different values for different final states. In a first approximation, this parameter is kept constant and chosen equal for all final states.

There are different possible ways to determine a value for the escape length parameter. First, one can simulate a process which has been investigated experimentally, adjusted such that the experimental yields are reproduced.

Another way is to propagate a pulse or pulse sequence leading to the excitation of final, ionizing or non-ionizing states. This is done for different values of d . At the end of the propagation the norm N is calculated as the sum of the populations P_i of all states

$$N = \sum_i P_i \quad , \quad (2.71)$$

and the difference to one is seen as the loss of norm

$$\bar{N} = 1 - N \quad . \quad (2.72)$$

The value for the escape length parameter where the loss of norm is maximal is taken, to obtain an “upper bound” for the ionization rate. Using “upper bounds” allows one to decide if ionization may play a role for a given process or quantity – or not. This variant is used in this work.

2.4 Reduced density matrices

2.4.1 Calculation of the von Neumann entropy

Electron correlation energy can be determined – as already stated in equation (2.25) – as the difference of the exact non-relativistic energy and the Hartree-Fock ground state energy, both within the Born-Oppenheimer approximation and at the basis set limit. This is true for the time-independent case. In a time-dependent picture, it cannot be said trivially how much a system is affected by electron correlation at a certain time. However, there are some approaches to calculate a correlation energy in a time-dependent scheme. One possible ansatz is based on MCTDHF and natural orbitals [60]. Another approach is to calculate the exact time-dependent electronic energy in a MCTDHF calculation and to take the Hartree-Fock energy from a TD-HF calculation. The correlation energy is the difference of these two time-dependent energies.

Another suitable measure for time-dependent electron correlation could be a single electron entropy calculated by means of a reduced one electron density matrix. This reduced one electron density matrix (or short one-matrix) can be calculated from a TD-CI or MCTDHF wavefunction. The one-matrix is derived as follows: If $\Psi(\underline{x}_1, \underline{x}_2, \dots, \underline{x}_N)$ is a normalized electronic wavefunction, the probability that one electron is in the space and spin volume element between \underline{x}_1 and $\underline{x}_1 + d\underline{x}_1$, and another electron is between \underline{x}_2 and $\underline{x}_2 + d\underline{x}_2$ and so on, is

$$\Psi(\underline{x}_1, \underline{x}_2, \dots, \underline{x}_N) \Psi^*(\underline{x}_1, \underline{x}_2, \dots, \underline{x}_N) d\underline{x}_1 d\underline{x}_2 \cdots d\underline{x}_N \quad . \quad (2.73)$$

The probability that an electron is between \underline{x}_1 and $\underline{x}_1 + d\underline{x}_1$, is obtained by integrating over all other coordinates $d\underline{x}_2 \cdots d\underline{x}_N$:

$$\rho(\underline{x}_1) = N \int \Psi(\underline{x}_1, \underline{x}_2, \dots, \underline{x}_N) \Psi^*(\underline{x}_1, \underline{x}_2, \dots, \underline{x}_N) d\underline{x}_2 \cdots d\underline{x}_N \quad (2.74)$$

where $\rho(\underline{x}_1)$ is the reduced density function for an electron in a N electron system. The reduced density function is normalized such that its integral gives the total number of electrons:

$$\int \rho(\underline{x}_1) d\underline{x}_1 = N \quad . \quad (2.75)$$

This can be generalized to the reduced one electron density matrix:

$$\gamma(\underline{x}_1, \underline{x}_{1'}) = N \int \Psi(\underline{x}_1, \underline{x}_2, \dots, \underline{x}_N) \Psi^*(\underline{x}_{1'}, \underline{x}_2, \dots, \underline{x}_N) d\underline{x}_2 \cdots d\underline{x}_N \quad . \quad (2.76)$$

The diagonal elements of the reduced one-electron density matrix are the electron densities at the respective coordinates, *i.e.*, $\gamma(\underline{x}_1, \underline{x}_1) = \rho(\underline{x}_1)$. This matrix can be expanded in the orthonormal basis of Hartree-Fock spin orbitals $\{\chi_i\}$ as

$$\gamma(\underline{x}_1, \underline{x}_{1'}) = \sum_{ij} \chi_i(\underline{x}_1) (\underline{\gamma})_{ij} \chi_j^*(\underline{x}_{1'}) \quad (2.77)$$

with the elements

$$(\underline{\gamma})_{ij}(\underline{x}_1, \underline{x}_{1'}) = \int \chi_i^*(\underline{x}_1) \gamma(\underline{x}_1, \underline{x}_{1'}) \chi_j(\underline{x}_{1'}) d\underline{x}_1 d\underline{x}_{1'} \quad (2.78)$$

forming the reduced one electron density matrix in the orthonormal basis of Hartree-Fock spin orbitals.

This density matrix formalism can be useful for various applications in quantum mechanics. One could use it to couple a system to an external bath (*e.g.*, a solvent or a surface) and propagate the density matrix, or one takes the time-dependent wavefunctions for a calculation of the reduced density matrix in order to determine

properties. Observables that are related to an arbitrary one-electron operator \hat{O} can be calculated from

$$\langle \hat{O} \rangle = \text{Tr}\{\underline{\underline{Q}}\underline{\underline{\gamma}}\} \quad . \quad (2.79)$$

A very special property that can be calculated from a one matrix is a single electron entropy (SEE) in the von Neumann definition [59], calculated as

$$S = -k_B \text{Tr}\{\underline{\underline{\gamma}} \ln \underline{\underline{\gamma}}\} \quad (2.80)$$

where k_B is Boltzmann's constant.

This SEE is zero if the total wavefunction consists of only one configuration, *e.g.*, the Hartree-Fock ground state wavefunction. Otherwise, the SEE is larger than zero as not all eigenvalues of $\underline{\underline{\gamma}}$ are either zero or one (see below).

2.4.2 Ionization in a dissipative environment [79]

Another interesting challenge is the development of a method which is capable of describing laser-driven electron dynamics including photoionization and dissipation. Therefore, the algorithm to calculate ionization rates from Sec. 2.3.3 was included into the ρ -TDCI method from Ref. [80]. The ρ -TDCI method is an extension of the TD-CI method to Liouville space, allowing for the treatment of coupling of the system to a bath which leads to energy and phase relaxation.

At the beginning, a field-free electronic Hamiltonian \hat{H}_{el} is considered, represented in a set of electronic configurations. From a CI calculation, the eigenvalues E_n and the eigenvectors $|n\rangle$ (denoted as Φ_n above) are obtained. Next, a reduced density operator is formulated

$$\hat{\rho}(t) = \sum_{nm} \rho_{nm}(t) |n\rangle \langle m| \quad , \quad (2.81)$$

where ρ_{nm} is an expansion coefficient. The density operator is propagated in time according to the Liouville-von Neumann equation [81] ($\hbar = 1$):

$$\frac{\partial \hat{\rho}(t)}{\partial t} = -i[\hat{H}_{el}, \hat{\rho}(t)] + i[\underline{\underline{\hat{\mu}}} \cdot \underline{\underline{E}}(t), \hat{\rho}] + \mathcal{L}_D \hat{\rho} \quad . \quad (2.82)$$

The interaction between the system and the field is treated within the semiclassical dipole approximation. Furthermore, dissipation is represented by the dissipative Liouvillian using the Lindblad semigroup formalism [82]:

$$\mathcal{L}_D \hat{\rho}(t) = -\frac{1}{2} \sum_k ([\hat{C}_k \hat{\rho}(t), \hat{C}_k^\dagger] + [\hat{C}_k, \hat{\rho}(t) \hat{C}_k^\dagger]) \quad , \quad (2.83)$$

where \hat{C}_k is a Lindblad operator, representing the k th dissipation channel. For the treatment of energy dissipation, we use upward and downward projectors

$$\hat{C}_k \rightarrow \sqrt{\zeta_{m \rightarrow n}} |n\rangle \langle m| \quad . \quad (2.84)$$

In this equation, $\zeta_{m \rightarrow n}$ is a dissipation rate, given as a scaled Einstein coefficient for spontaneous emission

$$\zeta_{m \rightarrow n} = \begin{cases} \frac{4A|\underline{\mu}_{m,n}|^2}{3c^3} \omega_{m,n}^3 & \text{if } m > n \\ 0 & \text{else} \end{cases} , \quad (2.85)$$

where $\omega_{m,n}$ is the energy difference between the CI eigenvalues E_m and E_n , $\underline{\mu}_{m,n}$ is the transition dipole moment $\langle m | \underline{\mu} | n \rangle$, and c is the speed of light in vacuum. A is a scaling factor to model electron-rich environments.

Another type of “relaxation” is pure dephasing, which arises from processes which are not due to energy relaxation, *i.e.*, processes which can be described as elastic scattering events. (In contrast to dissipation, which is due to inelastic scattering.) This type can be implicitly included by a Kossakowski-like model [83, 84], in which Lindblad operators are defined as

$$\hat{C}_k \rightarrow \sqrt{\nu^*} \hat{H}_{el} \quad . \quad (2.86)$$

Here, ν^* is a phenomenological pure dephasing rate. In order to describe also ionization in this model, there is an additional term $-i\hat{W}_{abs}$ to the electronic Hamiltonian \hat{H}_{el} ($\hat{H}_{el} \rightarrow \hat{H}_{el} - i\hat{W}_{abs}$), with the “absorption operator”

$$\hat{W}_{abs} = \sum_k \frac{\Gamma_k}{2} |k\rangle \langle k| \quad . \quad (2.87)$$

In this equation, Γ_k is a ionization rate for the state $|k\rangle$, calculated according to equation (2.70).

Without equation (2.87), the Liouville-von Neumann equation (equation (2.82)) is norm conserving ($\text{Tr}\{\hat{\rho}\} = 1$), but not energy or phase conserving. With equation (2.87) but without the term $\mathcal{L}_D \hat{\rho}$ in equation (2.82), the TD-CI with ionization of Sec. 2.3.3 is regained, which does not conserve the norm. With both equation (2.87) and the term $\mathcal{L}_D \hat{\rho}$ included in equation (2.82), we have an algorithm in which norm, energy, and phase relations are not conserved.

2.5 Laser pulses

In order to induce electronic transitions, laser pulses are used within this work. Here, five different pulses are used: π -pulses, manually optimized pulses (resonant or non-resonant), experimental pulses, pulses derived from optimal control theory (OCT) and pulses obtained from stochastic pulse optimization (SPO).

2.5.1 π -pulses

If a high population in a target state is desired, often π -pulses [85] are applied to the system. These are pulses whose parameters are chosen in a way that the area below the shape function leads to a complete population inversion in an idealized two-level system within the rotating wave approximation (RWA). All π -pulses and most of the other pulses in this work follow the expression:

$$\underline{E}(t) = \underline{f}_0 \cdot s(t) \cdot \cos(\omega(t - t_p)) \quad , \quad (2.88)$$

with the \cos^2 -type shape function

$$s(t) = \begin{cases} \cos^2\left(\frac{\pi}{2\sigma}(t - t_p)\right) & \text{if } |t - t_p| \leq \sigma \\ 0 & \text{else} \end{cases} \quad . \quad (2.89)$$

In these equations, $\underline{E}(t)$ stands for the electric field at time t , ω is the constant carrier frequency of the laser field. t_p is the time where the shape function is maximal, and \underline{f}_0 is the amplitude of the pulse. σ stands for the Full Width at Half Maximum (FWHM) of the pulse, which is – for \cos^2 -pulses – half of the total pulse width. A complete population inversion can be obtained if the π -pulse condition is fulfilled (in a two level system, if the RWA is valid):

$$|\underline{\mu}_{fi} \cdot \underline{f}_0| \int_{-\infty}^{\infty} s(t) dt = \pi \quad , \quad (2.90)$$

with $\underline{\mu}_{fi}$ being the transition dipole moment between the initial state $|i\rangle$ and final state $|f\rangle$. For \cos^2 -pulses the π -pulse condition (equation (2.90)) simplifies to

$$\underline{\mu}_{fi} \cdot \underline{f}_0 = \frac{\pi}{\sigma} \quad . \quad (2.91)$$

Below, we always use electric fields that are parallel to the transition dipole moment, *i.e.* $\underline{\mu}_{fi} \cdot \underline{f}_0 = \mu_{fi} \cdot f_0$.

2.5.2 Optimal control theory (OCT)

As in practice idealized two-level systems do not exist in this work, two-level π -pulses do not lead to a complete population inversion. So, alternatives are needed. One possibility is optimal control theory [86,87]. This theory is capable of computing a suitable pulse iteratively. Here, a modified algorithm by Rabitz [88–90] was used. In this approach, a total objective functional J is defined that should be maximal at the end of the control time t_f :

$$J = \langle \Psi(t_f) | \hat{O} | \Psi(t_f) \rangle - \int_0^{t_f} \alpha(t) |\underline{F}(t)|^2 dt - 2 \operatorname{Re} \left[\int_0^{t_f} \langle \Xi(t) | \frac{\partial}{\partial t} + i(\hat{H}_0 - \hat{\mu}\underline{F}(t)) | \Psi(t) \rangle dt \right] \quad (2.92)$$

In this equation, the first term takes care that the pulse excites the system to the target state $|\Psi_t\rangle$, for example, in which case \hat{O} is a positive target operator, *e.g.*,

$$\hat{O} = |\Psi_t\rangle\langle\Psi_t| \quad (2.93)$$

The second term limits the strength of the laser field, and the third term ensures that the time-dependent Schrödinger equation is obeyed. The positive function $\alpha(t)$ is calculated from

$$\alpha(t) = \frac{\alpha}{g(t)} \quad (2.94)$$

with a penalty factor α that controls the intensity of the laser field and another shape function

$$g(t) = e^{-\left(\frac{t-t_m}{\Delta t_s}\right)^{N_s}} \quad (2.95)$$

The shape function used here is a generalized Gaussian function. t_m is the midtime of the pulse, Δt_s is the pulse width, and N_s is an exponent. All values for these parameters are given later. The third term in equation (2.92) contains a Lagrange multiplier wave function $\Xi(t)$, defined in equation (2.97) below. The optimal laser field can be obtained from the following three coupled equations which follow from the condition that $\delta J = 0$, *i.e.*, J is maximized:

$$i \frac{\partial \Psi(t)}{\partial t} = (\hat{H}_0 - \hat{\mu}\underline{F}(t)) \Psi(t) \text{ with } \Psi(t=0) = \Psi_0 \quad (2.96)$$

$$i \frac{\partial \Xi(t)}{\partial t} = (\hat{H}_0 - \hat{\mu}\underline{F}(t)) \Xi(t) \text{ with } \Xi(t_f) = \hat{O} \Psi(t_f) \quad (2.97)$$

$$\underline{F}(t) = -\frac{1}{\alpha(t)} \operatorname{Im}[\langle \Xi(t) | \hat{\mu} | \Psi(t) \rangle] \quad (2.98)$$

Here, equation (2.96) is used for a propagation forward in time, starting from $t = 0$, and equation (2.97) is used for a propagation backward in time, starting from $t = t_f$.

After several forward and backward propagations, the field converges monotonically to an optimal field, and can be calculated from equation (2.98). The equations (2.96) and (2.97) are time-dependent Schrödinger equations that can be solved in the same manner as equation (2.35). The initial wave function Ψ_0 is usually the ground state wave function.

2.5.3 Stochastic pulse optimization (SPO)

Sometimes, the target can be expressed as a quantity that should be maximized or minimized, but cannot be represented by a target operator \hat{O} . An example is the single electron entropy of a system which shall be minimized photophysically. In this case, a stochastic pulse optimization is useful. In the present work, a similar algorithm to the one in Ref. [91] is used.

The x - ($k = x$) and y -components ($k = y$) of the external electric laser field \underline{E} propagating in z -direction are expressed as a truncated Fourier series using f frequency components:

$$F_k(t) = \frac{\omega}{\sqrt{\pi}} s(t) \sum_{l=0}^{f-1} [a_{k,l} \cos((l\omega_{min} + \omega_{min})t) + b_{k,l} \sin((l\omega_{min} + \omega_{min})t)] \quad \text{with } k = x, y \quad . \quad (2.99)$$

The minimal frequency ω_{min} is calculated as follows:

$$\omega_{min} = \frac{\pi}{t_{max}} \quad . \quad (2.100)$$

Here, t_{max} is the total width of the shape function $s(t)$. This shape function itself is defined as

$$s(t) = \begin{cases} 0 & \text{if } t < 0 \\ \sin^2\left(\frac{\pi t}{2t_{rf}}\right) & \text{if } 0 \leq t < t_{rf} \\ 1 & \text{if } t_{rf} \leq t < (t_{max} - t_{rf}) \\ \sin^2\left(\frac{\pi(t_{max}-t)}{2t_{rf}}\right) & \text{if } (t_{max} - t_{rf}) \leq t < t_{max} \\ 0 & \text{if } t \geq t_{max} \end{cases} \quad . \quad (2.101)$$

The parameter t_{rf} , which is indicated in Fig. 2.1, is the so-called “rise-fall time”. The coefficients $a_{k,l}$ and $b_{k,l}$ are chosen as random initially, but their Euclidean norm N_ω is kept constant:

$$N_\omega = \sum_{l=0}^{f-1} [a_{x,l}^2 + a_{y,l}^2 + b_{x,l}^2 + b_{y,l}^2] \quad . \quad (2.102)$$

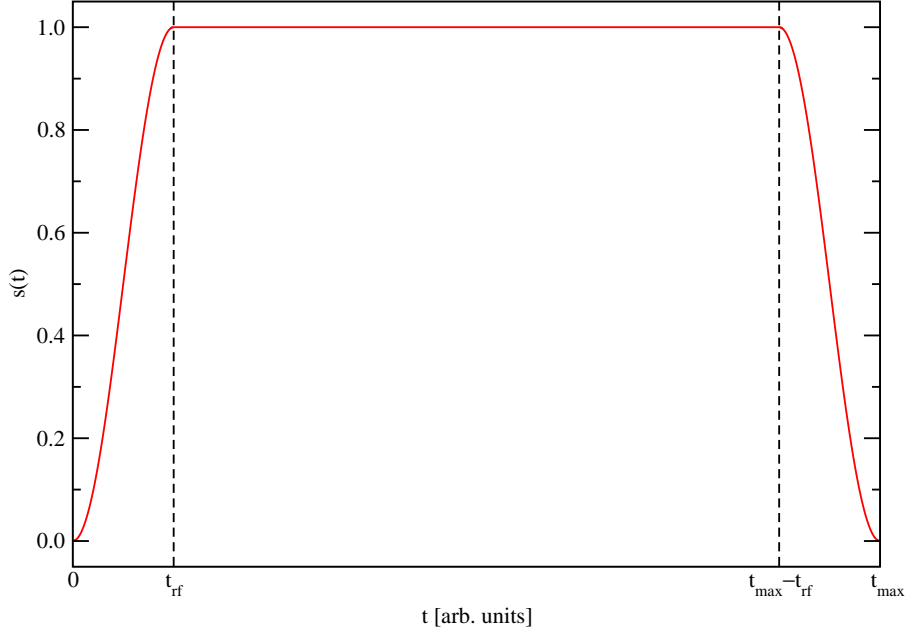


Figure 2.1: Shown is the shape function $s(t)$ of a pulse used within the stochastic pulse optimization algorithm. The “rise fall time” t_{rf} and the total width of the pulse t_{max} are indicated.

N_ω is only connected to the laser fluence in a first approximation as mixed frequency terms arising from the overcomplete basis in frequency space (see equation (2.100)) are neglected. Using these initial conditions and parameters, one can start a propagation. A set of g laser pulses $\{\underline{F}_p(t)\}$ ($p = 1, 2, \dots, g$) is created with

$$\underline{F}_p(t) = \begin{pmatrix} F_x(t) \\ F_y(t) \\ 0 \end{pmatrix} \quad (2.103)$$

where $F_x(t)$ and $F_y(t)$ are calculated according to equation (2.99). For each of these laser pulses, a propagation is performed within the TD-CISD method, the reduced one-electron density matrix is built, and the single electron entropy at the end of the pulse is calculated according to equation (2.80). The propagations are sorted by increasing single electron entropy. These laser fields form the “parent generation”. In a next step, the laser fields for the “child generation” are calculated by varying the coefficients of the truncated Fourier series (equation (2.99)), *i.e.*,

$$\bar{a}_{k,l} = a_{k,l}(1 + R \cdot M) \quad , \quad (2.104)$$

where R is a random number from the interval $[-1; +1]$ and M is a “mutation rate” that is constant during an optimization. A propagation is done for each of

the laser pulses from the “child generation” after renormalization of N_ω and the single electron entropy at the end of the pulse is calculated again. There are now $2g$ single electron entropy values (g from the “parent generation” and g from the “child generation”). The g laser fields leading to the lowest single electron entropy values are taken as a new “parent generation” for another optimization step. After a certain number of steps, the optimization is finished and one obtains a laser field which creates a lower single electron entropy in the respective system.

2.6 Electronic transitions

2.6.1 Processes of interest

With the methods presented here, many optically stimulated processes can be treated, such as stimulated emission and laser excitations. Some of the processes, that can be described with the methods presented in this work, are shown in Fig. 2.2.

Most of these processes can be also described within time-dependent perturbation theory (TD-PT) [28]. In this thesis, in most cases electronic transitions are modeled non-perturbationally using time-dependent configuration interaction theory including photoionization. The influence of photoionization on state-to-state transitions (below or above Koopmans’ ionization potential [77]) or response properties like the dynamic polarizability is evaluated.

2.6.2 Induced dipole moment

If the laser frequency is not resonant, there is still an effect of the electric field on the system. The field leads to a movement of the electrons in the system. As a consequence, there is – in addition to the permanent dipole moment $\underline{\mu}_0$ – a time-dependent induced dipole moment $\underline{\mu}^{ind}(t)$

$$\underline{\mu}(t) = \underline{\mu}_0 + \underline{\mu}^{ind}(t) \quad . \quad (2.105)$$

The induced dipole moment depends only on the current electric field $F(t)$ and can be expanded in a Taylor series

$$\begin{aligned} \mu_q^{ind}(t) = & \sum_{q'} \alpha_{qq'} F_{q'}(t) + \frac{1}{2!} \sum_{q'} \sum_{q''} \beta_{qq'q''} F_{q'}(t) F_{q''}(t) \\ & + \frac{1}{3!} \sum_{q'} \sum_{q''} \sum_{q'''} \gamma_{qq'q''q'''} F_{q'}(t) F_{q''}(t) F_{q'''}(t) + \dots \end{aligned} \quad (2.106)$$

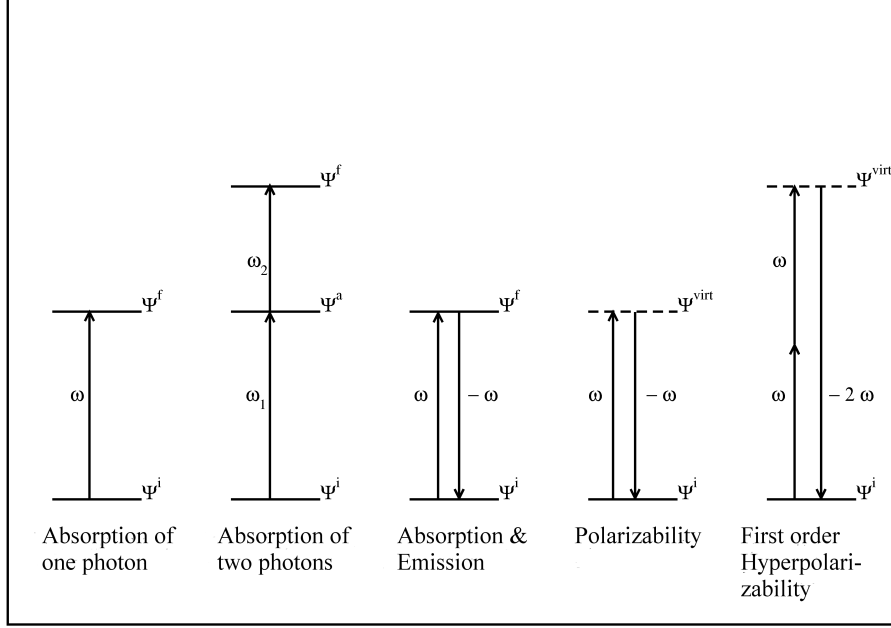


Figure 2.2: Shown are some of the electronic transitions and processes that can be described using TD-CI methods.

with $q, q', q'', q''' = x, y, z$. Here, $\underline{\alpha}$ stands for the polarizability, $\underline{\underline{\beta}}$ is the first order hyperpolarizability, $\underline{\underline{\underline{\gamma}}}$ is the second order hyperpolarizability. $\alpha_{qq'}$ is the element of the polarizability tensor that describes the effect of an electric field polarized along q' on the dipole moment along q . This equation is only valid for constant electric fields, but also a good approximation for weak periodic fields. In this case, all polarizabilities are frequency-dependent (dynamic polarizability). If a periodic electric field with a high intensity is investigated, the induced dipole moment can be calculated from the equation [28, 92]:

$$\begin{aligned}
 \mu_q(t) = & \mu_{0q} + \alpha_{qq'}(0; 0)F_{0,q'} + \alpha_{qq'}(-\omega; \omega)F_{\omega,q'} \cos(\omega t) \\
 & + \frac{1}{2}\beta_{qq'q''}(0; 0, 0)F_{0,q'}F_{0,q''} + \frac{1}{4}\beta(0; \omega, -\omega)F_{\omega,q'}F_{\omega,q''} \\
 & + \beta_{qq'q''}(-\omega; \omega, 0)F_{0,q'}F_{\omega,q''} \cos(\omega t) \\
 & + \frac{1}{4}\beta_{qq'q''}(-2\omega; \omega, \omega)F_{\omega,q'}F_{\omega,q''} \cos(2\omega t) + \dots
 \end{aligned} \tag{2.107}$$

In equation (2.107), the Einstein sum convention has been used, *i.e.*, we sum over terms in which indices q, q', q'', \dots occur twice. Therefore, the electric field is written as a sum of a constant electric field \underline{F}_0 and a periodic electric field \underline{F}_ω with a frequency ω :

$$\underline{F}(t) = \underline{F}_0 + \underline{F}_\omega \cos(\omega t) \quad . \tag{2.108}$$

In equation (2.107), $\alpha(-\omega; \omega)$ stands for the situation when a photon with the frequency ω is absorbed by the molecule, and a photon with the frequency ω is emitted (as a convention, the frequencies of emitted photons are negative). The induced dipole moment has the same frequency as the electric field. The value on the left side of the semicolon of $\alpha(\omega_1; \omega_2)$ stands for the frequency of the emitted photon (and for the frequency of the induced dipole moment), while the value on the right side stands for the frequency of the absorbed photon that is the frequency of the applied laser field.

The frequency dependence of the dynamic polarizability can be calculated perturbationally by the sum-over-states method [93] as described by the equation:

$$\alpha_{qq'}(-\omega; \omega) = \sum_{n \neq 0} \left[\frac{\langle 0 | \hat{\mu}_q | n \rangle \langle n | \hat{\mu}_{q'} | 0 \rangle}{\omega_{n,0} - \omega} + \frac{\langle 0 | \hat{\mu}_{q'} | n \rangle \langle n | \hat{\mu}_q | 0 \rangle}{\omega_{n,0} + \omega} \right] . \quad (2.109)$$

In this equation, $|0\rangle$ stands for the ground state, $|n\rangle$ is a higher electronic state, $\omega_{n,0}$ is the resonant transition frequency between $|0\rangle$ and $|n\rangle$, and ω is the frequency of the electric field.

As a consequence of equation (2.109), there is a pole at each transition frequency. If the induced dipole moment is parallel to the polarization of the laser field ($q = q'$), equation (2.109) simplifies to

$$\alpha_{qq}(-\omega; \omega) = 2 \sum_{n \neq 0} \frac{\omega_{0,n} \mu_{0,n;q}^2}{\omega_{0,n}^2 - \omega^2} . \quad (2.110)$$

If one component of the dipole moment vector is plotted versus one component of the electric field vector, the result is a so called “kennlinie” [94]. This “kennlinie” can be either horizontal (no field dependence), linear (for small electric field strengths, the effect of hyperpolarizabilities can be neglected), or polynomial (for high intensities). If the laser frequency is near a transition frequency, the “kennlinie” becomes more elliptical. At the resonance frequency, it should ideally be a circle due to a phase shift of $\frac{\pi}{2}$ near the transition frequency. The information on polarizabilities and hyperpolarizabilities can be extracted from a polynomial fit to the “kennlinie”. For small intensities where the hyperpolarizabilities are negligible, the polarizability can also be approximated by calculating the ratio of the induced dipole moment at the time where the pulse has its maximal intensity, and the field amplitude:

$$\alpha_{qq'} = \frac{\mu_q^{ind}(t = t_p)}{f_{0,q'}} \quad (2.111)$$

Chapter 3

Molecules in intense laser fields: Treatment of photoionization and applications

Whenever an electric field is applied to an atomic or molecular system, this changes the electronic structure. The fields can lead to induced dipole moments, to electronic transitions, and to photoionization. As already stated, there are two types of photoionization: On the one hand, there is tunneling ionization which occurs also far below the ionization potential. On the other hand, there is above-threshold ionization. The latter occurs when a system is excited above the ionization potential. Such an excitation may have several possible causes. One reason is the excitation using radiation with a sufficiently high frequency. This may be done intentionally when such a laser pulse is used in a pump-probe experiment. The excitation may also be caused by the finite spectral width of a short laser pulse even if the carrier frequency is below the IP. If a pulse is very long, the frequency width is very small. The shorter the pulse is, the wider the frequency range covered by the pulse. The third reason are multi-photon excitations. They become more probable if the laser field is intense. In this case, the system absorbs more than one photon and is thus excited to a high-energy state.

In this chapter, it is attempted to model the above-threshold ionization in molecular systems. For a first system (lithium cyanide molecule), the three algorithms described in Secs. 2.3.1-2.3.3 to calculate the ionization rates Γ_n of the respective states $|n\rangle$ are tested. Using the most suitable of these algorithms, it is also checked

if laser excitations below the ionization potential are still selective. Further, it is attempted to populate an ionizing state with a low ionization rate temporarily. Also, a pump-probe excitation for an electronic wavepacket using the ionization probability as the probe signal is simulated.

Further, pump-probe excitations that have longer delay times are simulated for a second system (benzo[g]-quinolinium-7-hydroxylate molecule). This molecule is expected, in contrast to the former, not to change the geometry much in the involved excited state. Therefore, the applied fixed nuclei approximation should be appropriate in this case. The parameters of the laser excitation are optimized such that the formation of multiply charged ions is not very likely.

Next, the influence of the photoionization on response properties is checked. For this purpose, the frequency-dependent polarizabilities of the hydrogen molecule are calculated with and without photoionization and compared to each other. For the case with photoionization, two algorithms are tested: on the one hand, the polarizabilities are calculated using a quadratic fit of the kenneilinie. On the other hand, the polarizabilities are determined using the sum-over-states formula in a time-independent approach.

Finally, it is attempted to simulate state-to-state transitions including photoionization in an electron-rich environment, *i.e.*, with dissipation. To this end, a direct excitation with a single π -pulse and a pulse sequence for the hydrogen molecule are shown using the algorithm presented in Sec. 2.4.2.

3.1 The lithium cyanide (LiCN) molecule [78]

3.1.1 System states and ionization rates

As a first system for TD-CIS including photoionization, the lithium cyanide molecule was used. This molecule is relatively small (3 atoms, 16 electrons), has a permanent dipole moment along the molecular axis, and excited states which have been shown to be charge transfer states [30, 32, 80].

At the beginning, a geometry optimization of the system was performed at the Hartree-Fock level of theory (RHF [7, 8, 64, 65]/6-31G* [95]) using the GAUSSIAN 03 program package [96]. The optimal bond lengths are $R_{LiC} = 3.68 a_0$ (1.95 \AA , $1 \text{ \AA} = 10^{-10} \text{ m}$) and $R_{CN} = 2.17 a_0$ (1.15 \AA), the bond angle is set to $\theta_{LiCN} = 180^\circ$. The molecule was then oriented with the Li—C bond along the z -axis.

Using this geometry and the GAMESS 07 program package [97], a RHF/6-31G* single point calculation was performed. The one- and two electron integrals were used for a CIS calculation resulting in 186 CIS singlet eigenstates out of 8 occupied spatial MOs (among these 3 frozen core orbitals) and 37 virtual spatial MOs. The energies, dipole moments, and transition dipole moments for all of these eigenstates were determined. Some of the data obtained is shown in Tab. 3.1.

As a first result, the lowest 18 states (S_0 to S_{17}) have excitation energies below the first ionization potential using Koopmans' theorem $IP = 0.39079 E_h$ (10.63 eV, $1 \text{ eV} = 1.602 \times 10^{-19} \text{ J}$). The ground state S_0 has a negative dipole moment along z of $\mu_{0,0,z} = -3.7082 e a_0$ (-9.4253 D , $1 \text{ D} = 3.3356 \times 10^{-30} \text{ C} \cdot \text{m}$) and corresponds to an ionic state Li^+CN^- . The second excited state S_2 ($E_2^{CIS} = 0.2418 E_h$ (6.580 eV) above S_0) has a dipole moment in the opposite direction $\mu_{2,2,z} = +2.7951 e a_0$ ($+7.1044 \text{ D}$). These two states are connected by a sufficiently high transition dipole moment along x ($\mu_{0,2,x} = +0.3082 e a_0$ ($+0.7834 \text{ D}$)). According to group theory, a transition is allowed, if the symmetry of at least one component (x , y , or z) of the direct product $\Psi_f \otimes x(\text{or } y \text{ or } z) \otimes \Psi_i$ spans the totally symmetric representation of the point group. Furthermore, the symmetry of the orbitals involved in the CSF that dominates the transitions is used instead of the symmetry of the CIS eigenstates. The excitation from the electronic ground state to the second excited state is dominated by a HOMO-LUMO transition. Within the $C_{\infty v}$ point group, the HOMO has Π symmetry, the LUMO has Σ^+ symmetry. The third factor in the direct product must have Π symmetry, because only then the resulting symmetry spans the Σ^+ symmetry. This is fulfilled, if a pulse is polarized along x or y , as $\Sigma^+ \otimes \Pi \otimes \Pi \sim \Sigma^+ + \Sigma^- + \Delta$ and contains thus Σ^+ .

The second and the ninth excited state S_9 ($E_9^{CIS} = 0.3028 E_h$ (8.239 eV) above S_0) are connected with an even larger, equally polarized transition dipole moment of $\mu_{2,9,x} = -1.6019 e a_0$ (-4.072 D). As the $S_2 \rightarrow S_9$ excitation is dominated by an electron transition from the LUMO (Σ^+ symmetry) to the LUMO+2 (Π symmetry), a transition is possible if a pulse is polarized along x or y , because then the direct product contains Σ^+ symmetry. These three states (S_0 , S_2 , and S_9) can be used for a simulation of laser-controlled electron dynamics below the ionization potential. All other CIS eigenstates are included as well.

For all states, the ionization rates Γ_n are calculated. The escape length parameter d is for this calculation arbitrarily set to $d = 1 a_0$ (0.529 \AA) in order to enable a

comparison between the results for different ionization rate models. The ionization rates for the LiCN molecule with all of the three algorithms of Secs. 2.3.1-2.3.3 are shown in Fig. 3.1. There, one can see that the ionization rate within the eigenstate model gives on the one hand, a set of non-ionizing states (the ionization rate is $\Gamma = 0 \frac{E_h}{\hbar}$ for all states below the ionization potential (IP) according to Koopmans' theorem [77]). On the other hand, the ionization rates for states whose excitation energies are above IP increase monotonically due to the $\sqrt{E_n^{CIS} - IP}$ dependence of the ionization rate. This behavior is not desirable, as the ionization rate for some high-energetic state might also be lower than the ionization rates of neighboring states. For the CSF model, the ionization rates do not increase monotonically. There is, however, no set of non-ionizing states below the IP except the ground state. As the lifetimes of the excited states are very short (the shortest in the range of $2 \frac{\hbar}{E_h}$ (48 as)), selective excitations are rather impossible. The combined model has both: a set of non-ionizing states below the IP and a non-monotonic behavior above IP. Hence, the combined model is used for the following simulations.

In order to simulate electron dynamics including photoionization within the TD-CIS method and the combined model, an optimal value for the escape length d is needed. This value can be obtained either by propagating a pulse sequence or by applying the same pulse to different initial states. In both cases, the escape length is varied and the loss of norm is calculated at the end of the propagation. For a “worst case scenario”, giving an upper bound for the effects of ionization, a value of d which yields the largest loss of norm is chosen. Here, a π -pulse sequence consisting of four non-overlapping pulses is used. The pulses are chosen to enforce the transitions

$$S_0 \rightarrow S_2 \rightarrow S_9 \rightarrow S_2 \rightarrow S_0 \quad (3.1)$$

below the ionization potential. As already mentioned, the transition dipole moments for these transitions are reasonably high. The first pulse is x -polarized with the parameters $t_p = 2000 \frac{\hbar}{E_h}$ (48.4 fs), $\sigma = 2000 \frac{\hbar}{E_h}$ (48.4 fs), $\hbar\omega = 0.2418 E_h$ (6.57 eV), $f_0 = 0.0051 \frac{E_h}{e a_0}$ ($2.6 \frac{GV}{m}$, $1 GV = 10^9 V$). The second pulse is also x -polarized and has the following parameters: $t_p = 6000 \frac{\hbar}{E_h}$ (145.1 fs), $\sigma = 2000 \frac{\hbar}{E_h}$ (48.4 fs), $\hbar\omega = 0.0610 E_h$ (1.66 eV), $f_0 = 0.0010 \frac{E_h}{e a_0}$ ($510 \frac{MV}{m}$, $1 MV = 10^6 V$). The third pulse is identical to the second one with $t_p = 10000 \frac{\hbar}{E_h}$ (241.9 fs) and the fourth pulse is the same as the first one, but with $t_p = 14000 \frac{\hbar}{E_h}$ (338.6 fs). The whole sequence ends at $t_f = 16000 \frac{\hbar}{E_h}$ (387.0 fs). For a TD-CIS propagation without ionization, this sequence results in a final population of the state S_0 of $P_0(t_f) = 0.987$. The

S_n	$E_{n,exc}^{CIS}$ [E_h]	$\mu_{n,n,z}$ [ea_0]	$\mu_{0,n,x}$ (ea_0)	$\mu_{2,n,x}$ [ea_0]	τ_n [$\frac{\hbar}{E_h}$]
0	0.00000	-3.7082	0.0000	+0.3082	∞
1	0.23898	-1.5832	0.0000	+0.0449	∞
2	0.24180	+2.7951	+0.3082	0.0000	∞
\vdots	\vdots	\vdots	\vdots	\vdots	\vdots
9	0.30278	+1.2341	0.0000	-1.6019	∞
\vdots	\vdots	\vdots	\vdots	\vdots	\vdots
17	0.38254	-1.5390	0.0000	+0.0901	∞
IP	0.39079	—	—	—	—
18	0.39230	+3.2742	0.0000	+0.1417	17.233
\vdots	\vdots	\vdots	\vdots	\vdots	\vdots
69	0.98349	+2.8164	0.0000	-0.7255	22.436
\vdots	\vdots	\vdots	\vdots	\vdots	\vdots
185	5.25264	-1.9455	0.0000	-0.0014	0.4657

Table 3.1: Shown are the excitation energies $E_{n,exc}^{CIS}$, the permanent dipole moments along z , $\mu_{nn,z}$, the transition dipole moments from the ground state, $\mu_{0,n,x}$ and from the second excited state, $\mu_{2,n,x}$ along x , and the lifetimes with respect to photoionization, τ_n , for some states S_n within the lithium cyanide molecule, all determined in a CIS [69]/6-31G* [95] calculation. The states S_{18} , S_{69} , and S_{185} are above the ionization potential (IP) [77] and thus not stable.

time-dependent populations $P_i(t)$ and the norm $N(t) = \sum_{i=0}^{185} P_i(t)$ are calculated for the whole propagation time using the heuristic ionization model and different values of d . After a time of $t_{final} = 26000 \frac{\hbar}{E_h}$ (628.9 fs), the norm does not change any more. Then, a loss of norm $\bar{N}(t) = 1 - N(t)$ is calculated for different values of d and the obtained values are compared to each other. This is shown in Fig. 3.2.

In the figure, it is seen that the loss of norm becomes maximal for $d \approx 1 a_0$. There, one observes a loss of norm of $\bar{N}(t_{final}; d \approx 1 a_0) \approx 0.13$ (while the target state population is $P_0(t_{final}) = 0.864$). The loss of norm decreases for larger and for smaller values for the “escape length”. If $d \gg 1 a_0$, the distance the classical electron has to travel is too large, so ionization does not occur. If the escape length is too small, ionization is also not probable. This can be understood from considering the

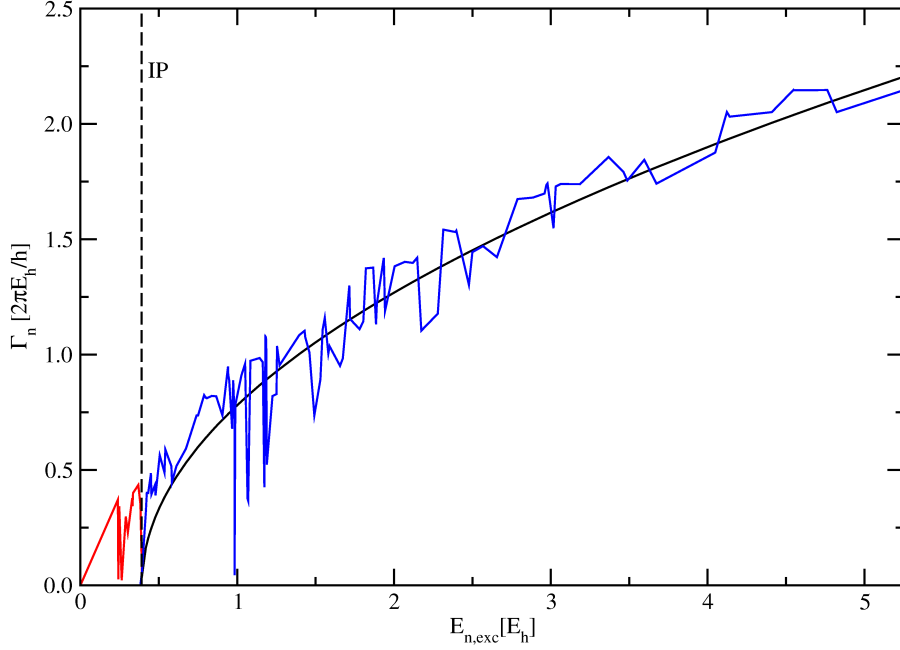


Figure 3.1: Shown are the ionization rates Γ_n with respect to the ionization energy $E_{n,exc}$ for all CIS states $|n\rangle$ within the LiCN molecule. The black line indicates the ionization rates according to the eigenstate algorithm of Sec. 2.3.1, which behaves as $\Gamma_n \sim (E_n^{CIS} - IP)^{\frac{1}{2}}$ according to equation (2.65). The red line stands for the CSF algorithm of Sec. 2.3.2, and the blue line is the ionization rate within the combined model (Sec. 2.3.3). The vertical black dashed line indicates the ionization potential (IP) according to Koopmans' theorem [77]. Above IP, the CSF model and the combined model have the same ionization rates, below IP, the ionization rates of both the eigenstate and the combined algorithm are zero.

situation of absorbing potentials in real space. There, two major errors exist: the transmission through the potential and the reflection from the absorbing potential. For small d values, the “absorbing potentials” ($-\frac{i}{2}\Gamma_n$) become unphysically large, so a large part of the population is reflected back to stable, non-ionizing states, which explains the small loss of norm for small d values. In the following, the value $d = 1 a_0$ is chosen in order to simulate a *worst case scenario*.

As the combined model for photoionization within the TD-CIS method does not contain a continuum by itself, but a set of discrete states above IP with finite lifetimes, it should be checked, if the broadening of these discrete states leads to a quasi-continuum. For this purpose, the density of states ρ_{DOS} is calculated as a sum of normalized Lorentzians of width Γ_n and the center at the excitation energy

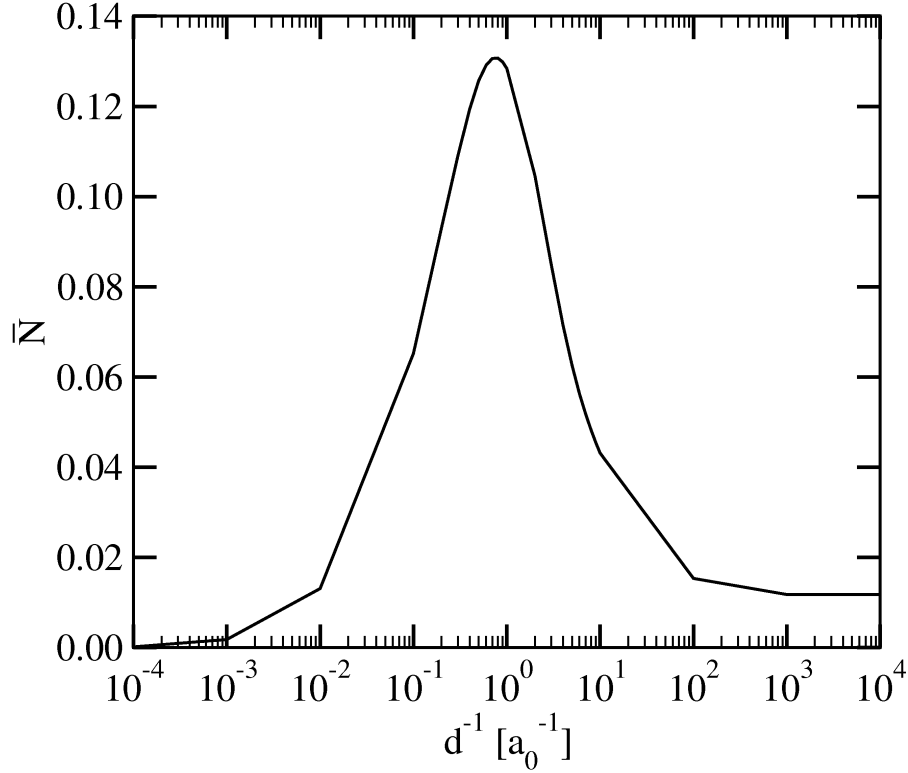


Figure 3.2: Shown is the loss of norm \bar{N} for different values of the inverse escape length parameter d^{-1} during a π -pulse sequence (see equation (3.1)) in the LiCN system.

of the discrete state S_n according to

$$\rho_{DOS}(E) = \frac{1}{\pi} \sum_n \frac{\frac{\Gamma_n}{2}}{(E - E_n^{CIS})^2 + (\frac{\Gamma_n}{2})^2} \quad (3.2)$$

and plotted in Fig. 3.3.

There, it is shown that most of the discrete states above the ionization potential (indicated by the left vertical dashed line) cannot be individually resolved, because they are energetically broadened. Only the states S_{18} and S_{69} have low ionization rates ($\Gamma_{18} = 0.0580 \frac{E_h}{h}$ ($2.4 \times 10^{15} \text{ s}^{-1}$), $\Gamma_{69} = 0.0446 \frac{E_h}{h}$ ($1.8 \times 10^{15} \text{ s}^{-1}$)), and therefore a peak at the corresponding energy (for S_{69} this is indicated by the right vertical dotted line). The discrete states below the ionization potential are delta functions, indicated by vertical lines representing a discrete non-ionizing state each. Furthermore, the density of states below IP is not exactly zero. This effect is a consequence of the broadening of ionizing states above IP.

We have just seen that the state S_{69} is only slowly ionizing. The reasons for this behavior can be understood from the nature of the CSFs forming this eigenstate. The major contribution comes from an excitation from MO 4 (the first non-1s orbital)

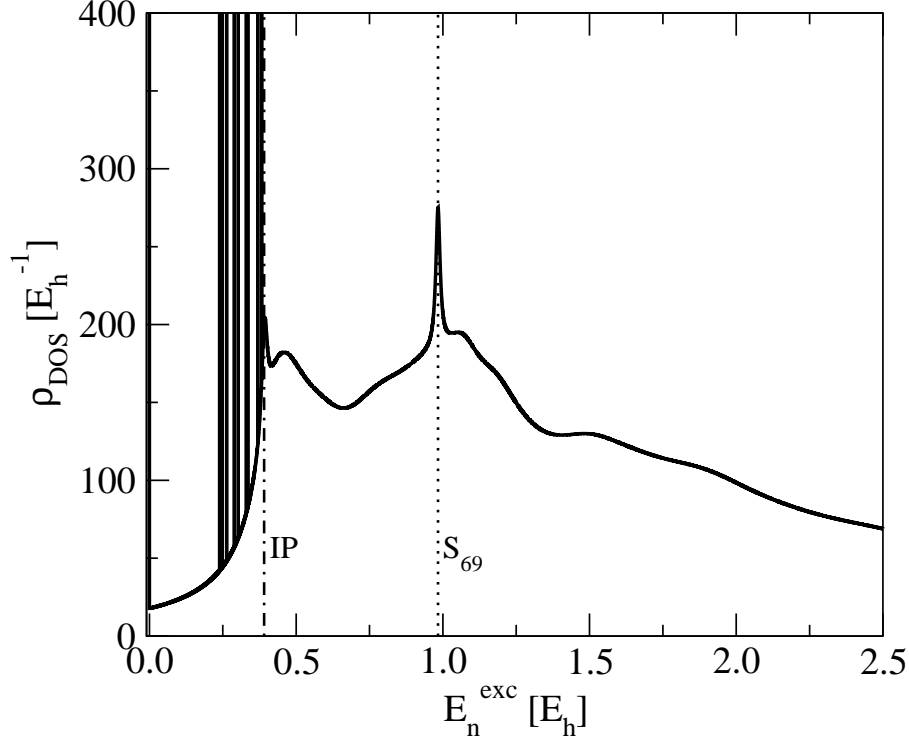


Figure 3.3: Shown is the density of states ρ_{DOS} according to equation (3.2). The non-ionizing states are indicated by vertical lines representing delta functions. Also, the ionization potential according to Koopmans' theorem (IP) and the sixty-ninth excited state (S_{69}), that has a remarkably low ionization rate, are indicated in this plot. The escape length is set to $d = 1 a_0$.

to MO 9 (the lowest unoccupied molecular orbital or LUMO), with a coefficient of $D_{4,69}^9 = -0.673632$. The energy difference of these two orbitals is $\Delta\varepsilon = \varepsilon_9 - \varepsilon_4 = 1.1169 E_h$ (30.4 eV), corresponding to a high-energy transition. Nevertheless, the LUMO has a negative orbital energy ($\varepsilon_9 = -0.0141 E_h$ (-0.38 eV)), so, this excitation does not contribute to the ionization rate (see equations (2.68) and (2.70)).

3.1.2 Transitions to non-ionizing states

As a first example of the effects of ionization, transitions to formally non-ionizing states are studied. For this purpose, the π -pulse sequence from equation (3.1) is used. The pulses have exactly the same parameters as described in the previous section. The escape length parameter is set to $d = 1 a_0$. We wish to see if these transitions are still selective and if the target states can be populated with sufficient probability even if ionization is considered. The time-dependent populations of some important states and the norm, *i.e.*, the sum of the populations of all states, are

shown in Fig. 3.4. From this figure, one can see that every π -pulse (indicated by the arrows at the top of the plot) leads to an almost complete population inversion. The norm only decreases slightly with each pulse, leading to a total loss of norm of $\bar{N}(t_{final}) \approx 0.13$. The larger part of this loss happens during the first and the last pulse, *i.e.*, during the transition from the ground state S_0 to the excited state S_2 and back. The reason for this is the higher possibility of multi-photon excitations due to the higher field intensity or maximal laser power ($P_{|0\rangle \leftrightarrow |2\rangle} = 9.12 \times 10^{15} \frac{\text{W}}{\text{m}^2}$ versus $P_{|2\rangle \leftrightarrow |9\rangle} = 3.51 \times 10^{14} \frac{\text{W}}{\text{m}^2}$, with $P = \frac{1}{2}c_0\varepsilon_0|\underline{f}_0|^2$) for the first and fourth pulse. However, this scheme shows that below-threshold excitations are still possible, selective, and efficient, even in a case of a strongly ionizing system.

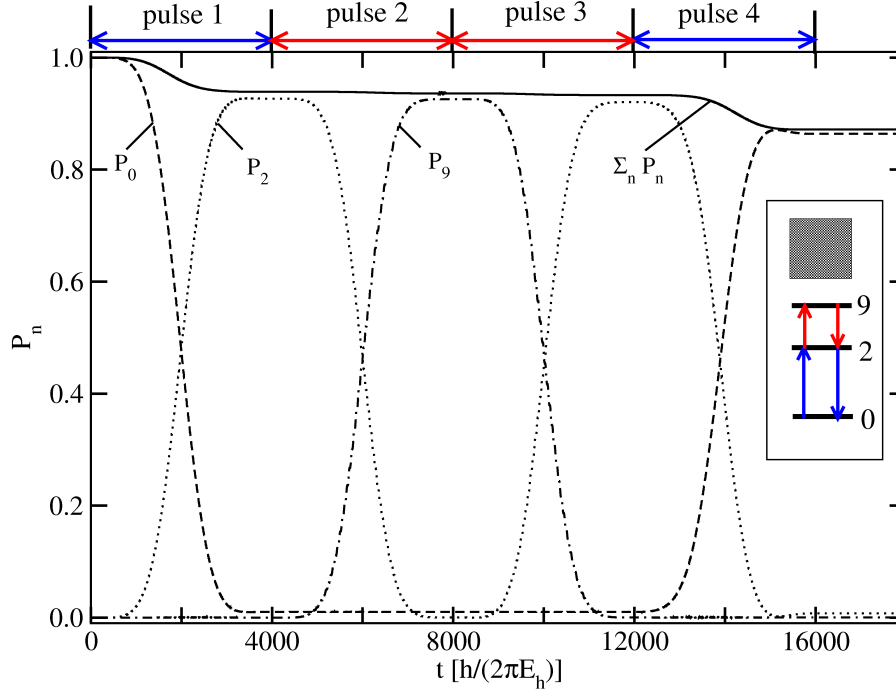


Figure 3.4: Shown is the temporal evolution of the populations P_n of the ground state (P_0), the second excited state (P_2), the ninth excited state (P_9), and the sum of all populations ($\sum_n P_n$) during a sequence of four non-overlapping π -pulses (see equation (3.1)) inducing transitions between states below the ionization potential within the LiCN molecule. The pulses are indicated by the arrows on top of the plot as well as in the inset. The escape length is set to $d = 1 a_0$.

3.1.3 Transitions to ionizing states

In Sec. 3.1.2 it was shown that the broadening of the ionizing states does not form an “ideal” continuum but some resonances appear, *e.g.*, for states S_{18} and S_{69} which

have relatively long lifetimes. In this section we try to populate these states (at least temporarily). It should also be checked if these excitations are selective, *i.e.*, if other, neighboring states are also populated or not.

The state S_{69} cannot be populated using a single π -pulse with a reasonable intensity as the transition dipole moment from the ground state to the sixty-ninth excited state is too low ($\underline{\mu}_{0,69} = (0.000, 0.000, -0.089)^\dagger \text{ ea}_0 ((0.000, 0.000, -0.226)^\dagger \text{ D})$). Therefore, a pulse sequence is used instead. Only the last pulse should target an ionizing state because transitions between ionizing states with high ionization rates are difficult (photoionization is faster than an electronic transition). Here, a sequence of two π -pulses is used. The first, x -polarized pulse has the parameters: $t_p = 4000 \frac{\hbar}{\text{E}_h}$ (96.8 fs), $\sigma = 4000 \frac{\hbar}{\text{E}_h}$ (96.8 fs), $\hbar\omega = 0.2418 \text{ E}_h$ (6.6 eV), $f_0 = 0.0025 \frac{\text{E}_h}{\text{ea}_0}$ ($1.3 \frac{\text{GV}}{\text{m}}$) and is used to enforce a transition from the electronic ground state S_0 to the second excited state S_2 ($\mu_{2,69;x} = -0.7255 \text{ ea}_0$ (-1.844 D), see Tab. 3.1). The second pulse is also x -polarized and induces a $S_2 \rightarrow S_{69}$ transition with the following parameters: $t_p = 8062.5 \frac{\hbar}{\text{E}_h}$ (195.0 fs), $\sigma = 62.5 \frac{\hbar}{\text{E}_h}$ (1.5 fs), $\hbar\omega = 0.7417 \text{ E}_h$ (20.2 eV), $f_0 = 0.0693 \frac{\text{E}_h}{\text{ea}_0}$ ($35.6 \frac{\text{GV}}{\text{m}}$).

In this scheme, the first pulse is twice as long as the one used in Sec. 3.1.2. Thus the laser power is reduced from $9.12 \times 10^{15} \frac{\text{W}}{\text{m}^2}$ to $2.19 \times 10^{15} \frac{\text{W}}{\text{m}^2}$ and the risk of multi-photon excitations decreases. The time-dependent populations of the ground state S_0 , the intermediate state S_2 , and the target state S_{69} are shown in Fig. 3.5 (only for the second pulse, because the first pulse is selective even for shorter pulse durations as demonstrated in Sec. 3.1.2). In this figure, one can see that the population of the sixty-ninth excited state increases up to $P_{69}^{max} = 0.12$. Then, the population decreases back to 0. The low maximal population in the target state S_{69} seems to indicate an unselective excitation. However, in the same time, the population of the second excited state decreases from 0.964 to 0.310 and the norm decreases from 0.969 to 0.314, *i.e.*, the remaining population is mostly in the second excited state. This indicates that no states except the intermediate and target states are populated significantly. So, the second pulse should be selective as well. Another result that fits to this conclusion, is a final population of 0.97 in the state S_{69} in the case of no photoionization ($\frac{1}{d} = 0$).

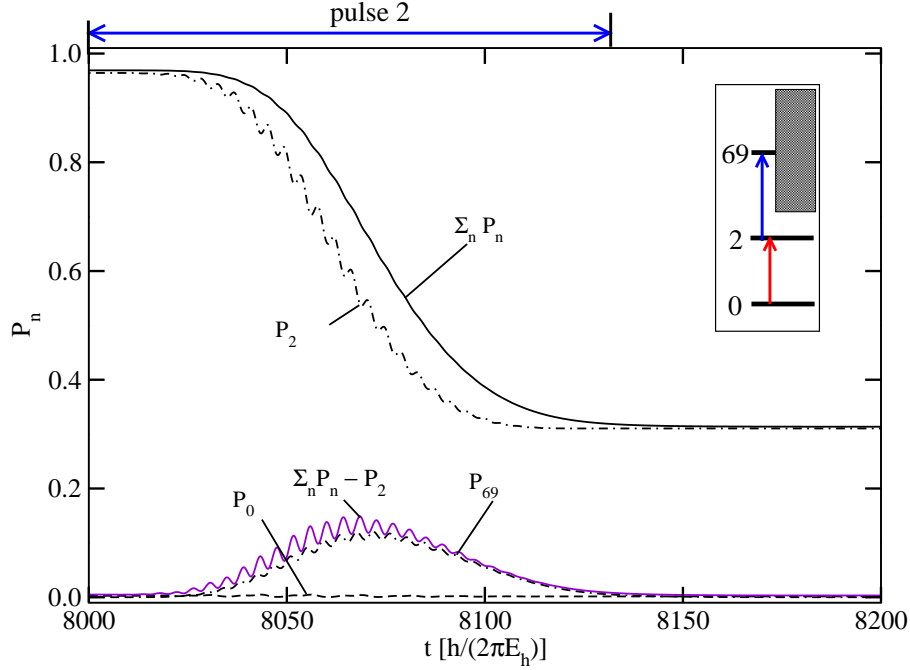


Figure 3.5: Shown is the temporal evolution of the populations P_n of the ground state (P_0), the second excited state (P_2), the sixty-ninth excited state (P_{69}), the sum of all states ($\sum_n P_n$), and the difference between the sum of all states and the population of the second excited state ($\sum_n P_n - P_2$) during a π -pulse excitation from S_2 to S_{69} within the LiCN molecule. The pulse is indicated by the arrow on top of the plot. The escape length is set to $d = 1 a_0$.

3.1.4 Creation of electronic wavepackets

After these state-to-state excitations, it could also be interesting to excite electronic wavepackets selectively. For these excitations, a superposition of the ground state S_0 and the ninth excited state S_9 is created which are connected by a high transition dipole moment along z of $\mu_{0,9;z} = -0.9580 e a_0$ (-2.43 D). This transition dipole moment has two advantages: on the one hand, this state can be easily accessed using a resonant pulse. On the other hand, the resulting wavepacket has an oscillating dipole moment with a high amplitude. Therefore, a z -polarized pulse with the following parameters is used: $t_p = 1000 \frac{\hbar}{E_h}$ (24.2 fs), $\sigma = 1000 \frac{\hbar}{E_h}$ (24.2 fs), $\hbar\omega = 0.3028 E_h$ (8.2 eV), $f_0 = 0.0011 \frac{E_h}{e a_0}$ ($566 \frac{MV}{m}$). This pulse is not a π -pulse (in fact it is a 0.335π -pulse). The resulting wavepacket has two major contributions coming from S_0 (population $P_0 = 0.721$) and S_9 ($P_9 = 0.273$). The total norm decreases to 0.993. The resulting dipole moment in the interval $t \in [2000; 2100] \frac{\hbar}{E_h}$ ([48.4; 50.8] fs) is shown in the upper left panel of Fig. 3.6. There, the dipole moment is also

Fourier transformed to frequency space (lower left panel of Fig. 3.6), showing that there is one main frequency peak at the transition frequency $\omega_{0,9}$, which means, the wavepacket consists mainly of these two states.

If the initial wavefunction $\Psi(t=0)$ consists of a superposition of two eigenfunctions Ψ_1 and Ψ_2 with respective real coefficients C_1 and C_2 , the time-dependent wavefunction is

$$\Psi(t) = C_1 \cdot e^{-iE_1t/\hbar} \Psi_1 + C_2 e^{-iE_2t/\hbar} \Psi_2 \quad . \quad (3.3)$$

The (time-dependent) expectation value of an arbitrary Hermitian operator \hat{A} for such a wavepacket is calculated as follows:

$$\langle \hat{A} \rangle(t) = \langle C_1 \cdot e^{-iE_1t/\hbar} \Psi_1 + C_2 e^{-iE_2t/\hbar} \Psi_2 | \hat{A} | C_1 \cdot e^{-iE_1t/\hbar} \Psi_1 + C_2 e^{-iE_2t/\hbar} \Psi_2 \rangle \quad . \quad (3.4)$$

This can be simplified to

$$\langle \hat{A} \rangle(t) = C_1^2 \langle \Psi_1 | \hat{A} | \Psi_1 \rangle + C_2^2 \langle \Psi_2 | \hat{A} | \Psi_2 \rangle + 2C_1 C_2 \text{Re}(e^{i(\omega_{12}t + \theta)} \langle \Psi_1 | \hat{A} | \Psi_2 \rangle) \quad . \quad (3.5)$$

In this equation, θ is an additional phase shift. The exponential function is transformed into a cosine function by using Euler's formula:

$$\langle \hat{A} \rangle(t) = |C_1|^2 \langle \Psi_1 | \hat{A} | \Psi_1 \rangle + |C_2|^2 \langle \Psi_2 | \hat{A} | \Psi_2 \rangle + 2|C_1 C_2| \cos(\omega_{12}t + \theta) \text{Re} \langle \Psi_1 | \hat{A} | \Psi_2 \rangle \quad (3.6)$$

This means, the amplitude of an oscillation is defined by the mixed integral $\langle \Psi_1 | \hat{A} | \Psi_2 \rangle$, while the frequency is given by the resonance frequency between the two populated states, ω_{12} . The pure integrals, $\langle \Psi_1 | \hat{A} | \Psi_1 \rangle$ and $\langle \Psi_2 | \hat{A} | \Psi_2 \rangle$ shift the expectation value. In our case, the dipole moment can be calculated as:

$$\langle \hat{\mu}_z \rangle(t) = C_0^2 \mu_{0,0,z} + C_9^2 \mu_{9,9,z} + 2C_0 C_9 \mu_{0,9,z} \cos(\omega_{0,9}t + \theta) \quad . \quad (3.7)$$

Using the values $C_0^2 = 0.721$ and $C_9^2 = 0.273$ for the populations, $\mu_{0,0,z} = -3.7082 \text{ ea}_0$ and $\mu_{9,9,z} = +1.2341 \text{ ea}_0$ for the dipole moments (see Tab. 3.1), $\mu_{0,9,z} = +0.9580 \text{ ea}_0$ for the transition dipole moment, $\omega_{0,9} = 0.30278 \frac{E_h}{\hbar}$ for the resonance frequency, and $C_0 \cdot C_9 = \sqrt{C_0^2 \cdot C_9^2} = 0.4437$ for the mixed term, the dipole moment of the created wavepacket is well reproduced (there is an additional phase shift of $\theta = -0.9\pi$).

3.1.5 Pump-probe spectra for electronic wavepackets

The wavepacket from Fig. 3.6 can be excited with a single probe pulse above the ionization potential. The probe pulse is delayed by a delay time Δt_p , which is

defined as the time delay between the maxima of the pump and the probe pulses: $\Delta t_p = t_{p,Probe} - t_{p,Pump}$. The probe pulse is x -polarized with the parameters: $t_p = 1000 \frac{\hbar}{E_h} + \Delta t_p$ (24.2 fs + Δt_p), $\sigma = 50 \frac{\hbar}{E_h}$ (1.2 fs), $\hbar\omega = 0.2500 E_h$ (6.8 eV), $f_0 = 0.0600 \frac{E_h}{e a_0}$ (30.8 $\frac{GV}{m}$). Thus, the probe pulse is very short (the frequency width is very large) and the intensity very high (the maximal laser power is about $P = 1.26 \times 10^{18} \frac{W}{m^2}$), so, multi-photon excitations could be promoted.

Such pump-probe simulations are usually done for a set of different delay times. Here, the delay time Δt_p was varied within the interval $\Delta t_p \in [-950; +1650] \frac{\hbar}{E_h}$ ($\Delta t_p \in [-23.0; +39.9]$ fs). The loss of norm was then calculated for the observation time $t_{observ} = 7000 \frac{\hbar}{E_h} + \Delta t_p$ (169.3 fs + Δt_p). The loss of norm starts at $\bar{N}(\Delta t_p = -950 \frac{\hbar}{E_h}) = 0.528$ and oscillates in an interval [0.378; 0.582]. Some of these oscillations (for delay times within the interval $\Delta t_p \in [1000; 1100] \frac{\hbar}{E_h}$ ($\Delta t_p \in [24.2; 26.6]$ fs)) are plotted in the upper right panel of Fig. 3.6. This oscillation is similar to the one observed for the dipole moment. A further analysis can be done if the loss of norm is expressed by a Fourier transformation in order to obtain a signal in frequency space. This is done in the lower right panel of Fig. 3.6. From this plot, it can be seen that the frequency of the loss of norm is equal to the oscillation frequency of the dipole moment of the wavepacket and thus identical to the transition frequency between the two states forming the wavepacket. The oscillating dipole moment reflects the oscillating position expectation value of the electrons ($\langle \Psi(t) | \sum_{i=1}^N r_i | \Psi(t) \rangle$ is a function of time). This changes the properties of the system such that the amount of ionized species depends on the time when the probe pulse has an effect on the wavepacket. As pump-probe techniques are used to visualize transient properties that cannot be measured directly, *i.e.*, in a “single shot” experiment, in a sufficiently high time resolution, this model seems to resemble the expected result of a pump-probe experiment. This means, the combined model seems to be at least qualitatively a suitable description of photoionization and related phenomena.

However, some critical points have to be made. The maximal observation time was $t_{observ,max} = 8650 \frac{\hbar}{E_h}$ (209.2 fs). On these timescales, one cannot neglect nuclear motion in molecules, especially if they contain light atoms. Another point is, that our heuristic model treats ionization processes only phenomenologically. Still, the simulations result in trends which one would intuitively expect from a pump-probe experiment.

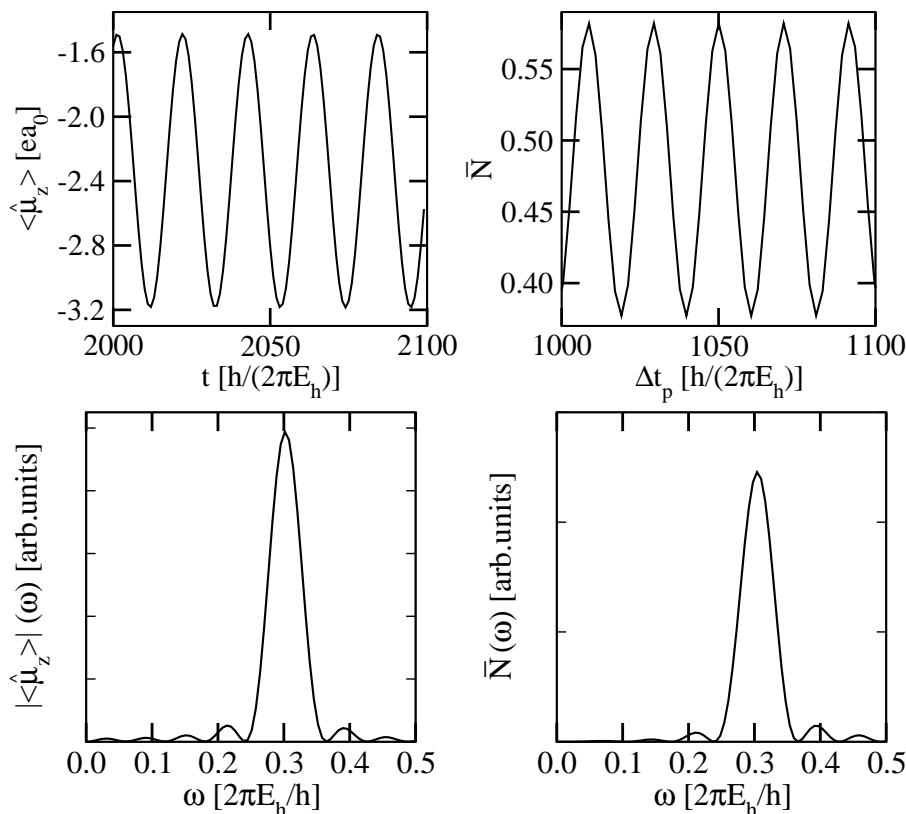


Figure 3.6: Shown is in the upper left panel the expectation value for the z -component of the oscillating dipole moment $\langle \hat{\mu}_z \rangle$ of a wavepacket consisting of states S_0 and S_9 of the LiCN system. In the lower left panel, the Fourier transform of the dipole moment (as a function of the frequency ω) is plotted. In the upper right panel, the loss of norm \bar{N} is plotted as a function of the delay time Δt_p as the probe signal. In the lower right panel, the Fourier transform of the loss of norm is shown. The escape length is set to $d = 1 a_0$.

3.2 A more rigid molecule

3.2.1 System states and ionization rates

The simulations for lithium cyanide in the previous section have shown the capability of the heuristic ionization model to describe pump-probe spectra. One major critical aspect was, that one cannot work within the fixed nuclei approximation on long timescales, in particular since some of the excited states of LiCN are unbound. Therefore, another model molecule is considered in this section, which allows only small geometry changes in the excited state. The model we chose is the benzo[g]-*N*-methyl-quinolinium-7-hydroxylate (BMQ7H) molecule. This molecule is planar

(apart from the methyl hydrogen atoms which are out of plane), and the ring structure should stabilize the molecular geometry. At the beginning, a geometry optimization (RHF/6-31G* [95]) was done using the GAUSSIAN 03 program package [96] resulting the molecular geometry shown in Fig. 3.7.

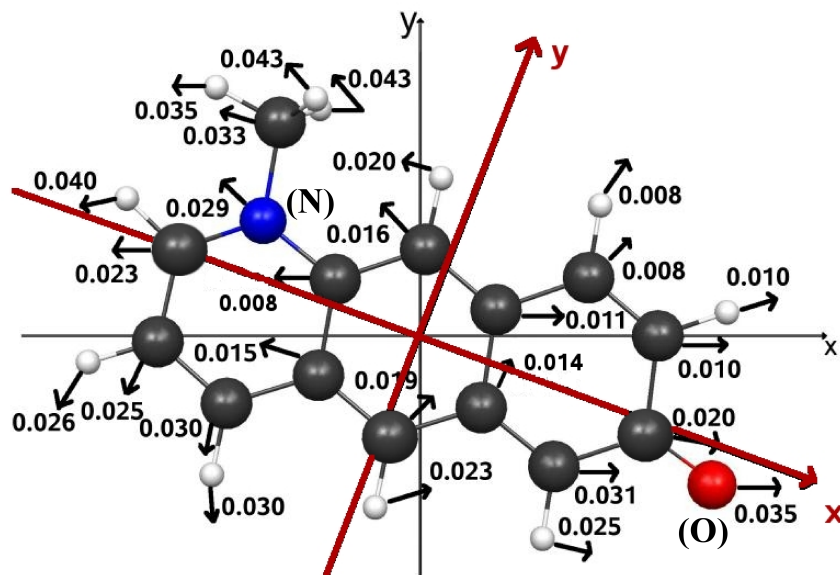


Figure 3.7: Shown is the ground state geometry of the molecule (black: carbon, white: hydrogen, blue: nitrogen, red: oxygen). The arrows indicate the displacement of the atoms when the system is excited to the fifth excited state, S_5 . All displacement values are given in Å. The thick red coordinate system is the one used for the calculations, the thin black one is used to align the ground state and the excited state geometries. (This leads to lower displacement values.)

For this geometry, a RHF/6-31G* [95] single point calculation was performed within the GAMESS 07 program package [97] in order to obtain the one- and two-electron integrals. These integrals were then used in a CIS calculation resulting in 8074 states out of 55 occupied spatial molecular orbitals (among these 16 frozen core orbitals) and 207 virtual spatial molecular orbitals. For these states, all excitation energies, dipole moments, and transition dipole moments were calculated. Some of these properties are given in Tab. 3.2.

From this table, one can see that the state S_5 (dominated by a HOMO-1 \rightarrow LUMO or $\pi \rightarrow \pi^*$ transition) seems to be very promising for a wavepacket consisting of S_0 and this state. The transition dipole moment from S_0 along x is very large, $\mu_{0,5;x} = -4.2228 \text{ ea}_0$ (-10.73 D), so the state should be accessible photophysically.

S_n	E_{exc}^{CIS} [E _h]	$\mu_{n,n}$ [ea ₀]		$\mu_{0,n}$ [ea ₀]		τ_n [$\frac{\hbar}{E_h}$]
		x	y	x	y	
0	0.0000	−6.1989	+1.4896	−6.1989	+1.4896	∞
1	0.0853	−2.3567	+0.5484	+1.7900	+0.8783	∞
2	0.1460	−4.0516	+1.7139	+0.2008	−0.3530	∞
3	0.1785	−3.8602	+0.3822	−0.3415	+0.1524	∞
4	0.1849	−1.8331	+0.8978	+0.0002	+0.0000	∞
5	0.1949	−3.3692	+1.6684	−4.2228	+0.4371	∞
IP	0.2057	—	—	—	—	—
6	0.2209	−3.5881	+1.1521	−0.2249	−0.5507	4.5544
7	0.2385	−5.7727	+0.6058	+1.1622	+0.2025	2.6158
8	0.2497	−5.1800	+1.0830	+0.9609	−0.0764	3.0435
9	0.2635	−4.4692	+2.4778	−1.9719	−0.7301	3.4412
10	0.2669	−1.6135	+1.0987	+0.0003	+0.0001	3.1447
\vdots	\vdots	\vdots	\vdots	\vdots	\vdots	\vdots
8073	6.5701	−15.8005	+2.9631	−0.0003	+0.0015	0.4342

Table 3.2: Shown are the excitation energies E_{exc}^{CIS} , the x - and y -components of the permanent dipole moments $\mu_{n,n}$ and the transition dipole moments for the excitation from the ground state $\mu_{0,n}$, and the lifetimes τ_n for some of the calculated CIS states S_n in the BMQ7H molecule. Also, the ionization potential according to Koopmans' theorem (IP) [77] is indicated. All values are obtained from a CIS [69]/6-31G* [95] calculation.

Also, the coupling ensures a high amplitude in the oscillating dipole moment of the wavepacket. This can be explained using group theory. The point group of the BMQ7H molecule is nearly C_s (apart from the methyl hydrogen atoms). The HOMO-1 and the LUMO both have A'' symmetry. The direct product $A'' \otimes A''$ gives A' which is the totally symmetric representation of this point group. The transition dipole moment is sufficiently high for the axes that have also A' symmetry, as $A' \otimes A' \sim A'$. This is the case for x and for y , which explains the results of Tab. 3.2.

The transition dipole moments from the ground state to neighboring states (S_1

to S_4 and S_6 to S_{10}) are much smaller than for the transition to the target state. Further, the fifth excited state is still below the ionization potential and has thus an infinite lifetime. Finally, the dipole moment changes along the principal axis x from $\mu_{0,0;x} = -6.1989 \text{ ea}_0$ (-15.76 D) to $\mu_{5,5;x} = -3.3692 \text{ ea}_0$ (-8.56 D), *i.e.*, the target state is a charge transfer state. For this state, a geometry optimization was performed (CIS/6-31G*) using the GAUSSIAN 03 program package in order to see how much the equilibrium geometries of the ground state and the target state differ from each other. In Fig. 3.7, the displacements within the xy -plane from the ground state to the fifth excited state are indicated by displacement vectors and the assigned values denote the displacements of the respective atoms, given in Å. There, it is seen that the maximum displacement is 0.043 Å. Therefore it seems, that the displacements within the xy -plane are insignificant. The maximal displacement perpendicular to the molecular plane is $2 \times 10^{-4} \text{ Å}$ and thus even smaller and also negligible. Also, the shift in the excitation energy is rather small. While the excitation energy for the ground state geometry is 0.1949 E_h (5.30 eV), the excitation energy at the equilibrium geometry of the fifth excited state is 0.1889 E_h (5.14 eV), the difference being only 0.006 E_h (0.16 eV).

One first thing that should be investigated is the optimal value for the escape length parameter d for this system. Therefore, the loss of norm is calculated for different initial states (all non-ionizing states). In these simulations, an intense x -polarized laser pulse with the following parameters is applied: $t_p = 12.4 \frac{\hbar}{\text{E}_h}$ (300 as), $\sigma = 12.4 \frac{\hbar}{\text{E}_h}$ (300 as), $\hbar\omega = 0.8000 \text{ E}_h$ (21.8 eV), $f_0 = 0.0100 \frac{\text{E}_h}{\text{ea}_0}$ ($5.1 \frac{\text{GV}}{\text{m}}$). After a control time of $t_{final} = 50 \frac{\hbar}{\text{E}_h}$ (1.21 fs), the loss of norm is calculated and plotted with respect to the reciprocal escape length parameter in Fig. 3.8. There, one can see that for all investigated excited states a maximal loss of norm is achieved when the escape length is set to $d = 1 \text{ a}_0$ (0.529 Å) while the ground state tends to higher escape lengths (lower reciprocal escape lengths). The optimal value for the ground state would be $d = 1 \times 10^{+1} \text{ a}_0$ (5.29 Å). As the loss of norm for a situation when the pulse is applied to the ground state is still rather high for $d = 1 \text{ a}_0$ (0.529 Å), this value should be a good choice in order to obtain a model with a strongly ionizing system. Furthermore, one sees in Fig. 3.8 that the loss of norm is significantly higher for the ground state as initial state than for the excited states as initial states. This counterintuitive result will be analyzed and discussed later.

It can be also interesting to see if the combined model results in a continuum

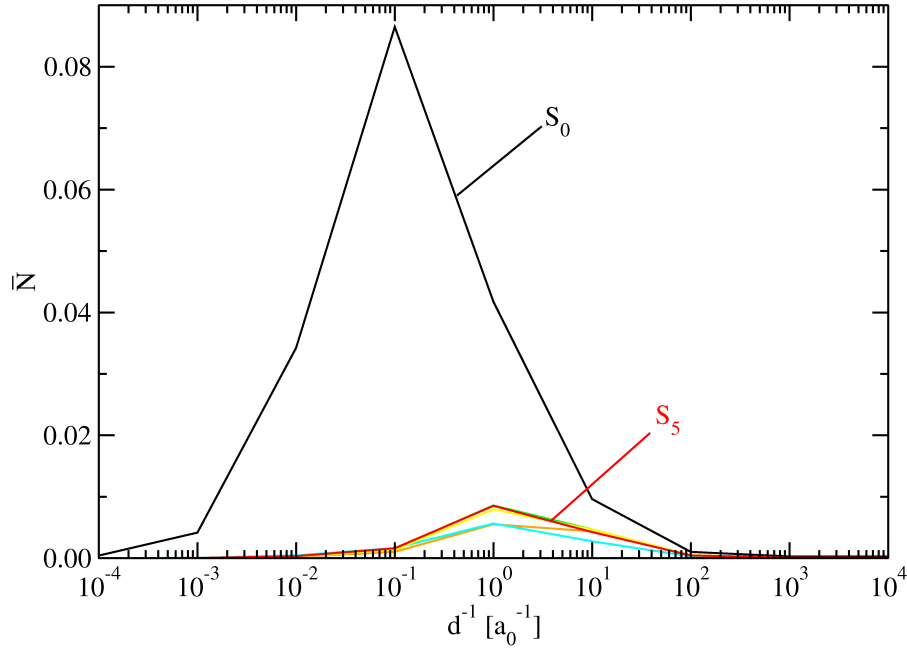


Figure 3.8: Shown is the loss of norm \bar{N} as a function of the inverse escape length parameter d^{-1} when an intense laser pulse (for details see text) is applied to different non-ionizing initial states of the BMQ7H system. The states that will be used to form an electronic wavepacket are highlighted. The other states are S_1 (orange), S_2 (green), S_3 (cyan), and S_4 (yellow).

above the ionization potential. For this purpose, the ionization rates and the density of states are plotted in Fig. 3.9. In the upper panel, one can see by the oscillations in the generally ascending curve that the ionization rate tends to higher values for higher excited states, but there are still states with lower ionization rates compared to other, neighboring states. The effect does not lead to such a weakly ionizing state as S_{69} in lithium cyanide because the ionizing states are not dominated by electron transitions from low-energy occupied orbitals to virtual orbitals below the vacuum energy. In the lower panel, it is shown that a continuum is formed above the ionization potential. As there are no extremely weakly ionizing states above the ionization potential, no state can be individually resolved as a resonance here.

3.2.2 Creation of electronic wavepackets

Next, a wavepacket consisting mainly of the electronic ground state S_0 and the fifth excited state S_5 will be created using \cos^2 -shaped laser pulses. In this case, a “suboptimal” pulse is used in order to show that such pulses are also capable of

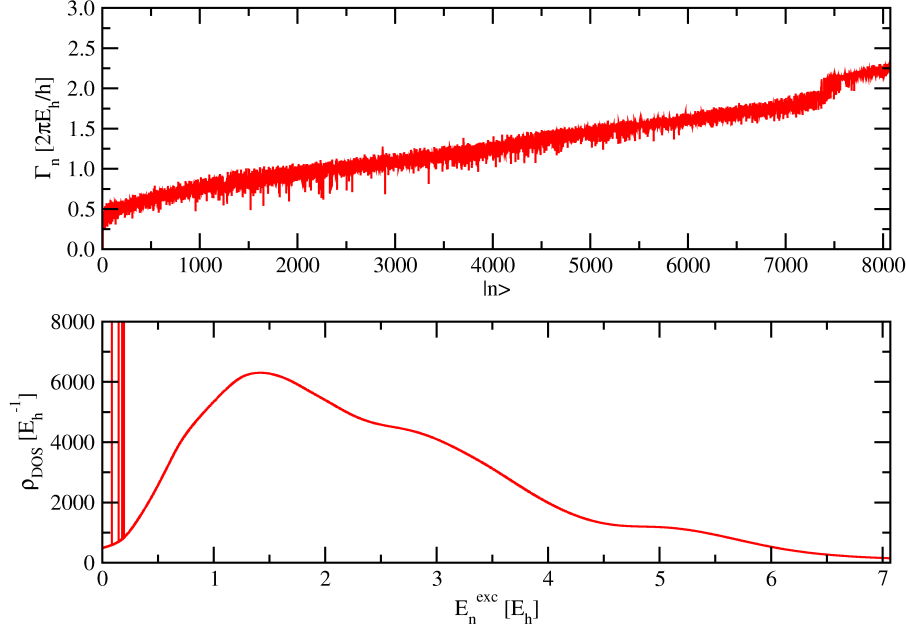


Figure 3.9: Shown are in the upper panel the ionization rates Γ_n for all CIS [69]/6-31G* [95] eigenstates $|n\rangle$ of the BMQ7H molecule with the escape length $d = 1 a_0$. The states $|0\rangle$ to $|5\rangle$ are non-ionizing. In the lower panel, the density of states ρ_{DOS} according to equation (3.2) is plotted. The discrete states for $E_n^{exc} < IP$ are indicated by vertical lines, representing delta functions.

exciting a target selectively and because most experimental pulses are not exactly resonant. Such a non-resonant pulse, as shown in panel (a) of Fig. 3.10, is used here. The pulse is x -polarized with the parameters: $t_p = 125 \frac{\hbar}{E_h}$ (3.02 fs), $\sigma = 125 \frac{\hbar}{E_h}$ (3.02 fs), $\hbar\omega = 0.1837 E_h$ (5.0 eV), $f_0 = 0.0060 \frac{E_h}{ea_0}$ (3.1 $\frac{GV}{m}$). The resulting time-dependent populations are plotted in panel (b) of Fig. 3.10. The applied field leads to a population of 0.256 in the ground state and 0.599 in the fifth excited state. The sum of the populations of all states is 0.862, the maximal population in another state is 6.9×10^{-3} (in the third excited state).

The electronic wavepacket created in this way shows oscillations of the dipole moment along the coordinates x (panel (c) of Fig. 3.10) and y (panel (d)). There, it is shown that both dipole moments are oscillating with a similar main frequency, which reflects the transition frequency from the ground state to the fifth excited state. Both dipole components show a second oscillation with a longer period, which is most clearly seen in the plot of $\langle \hat{\mu}_y \rangle$. Also seen is that the amplitude for the main oscillation is higher in the case of $\langle \hat{\mu}_x \rangle$ (waving between $-7.01 ea_0$ (-17.82 D) and $-0.21 ea_0$ (-0.53 D)), than for $\langle \hat{\mu}_y \rangle$ (oscillating between $0.98 ea_0$

(2.49 D) and 1.80 ea_0 (4.57 D)), which reflects the larger component of the transition dipole moment, along x (see Tab. 3.2).

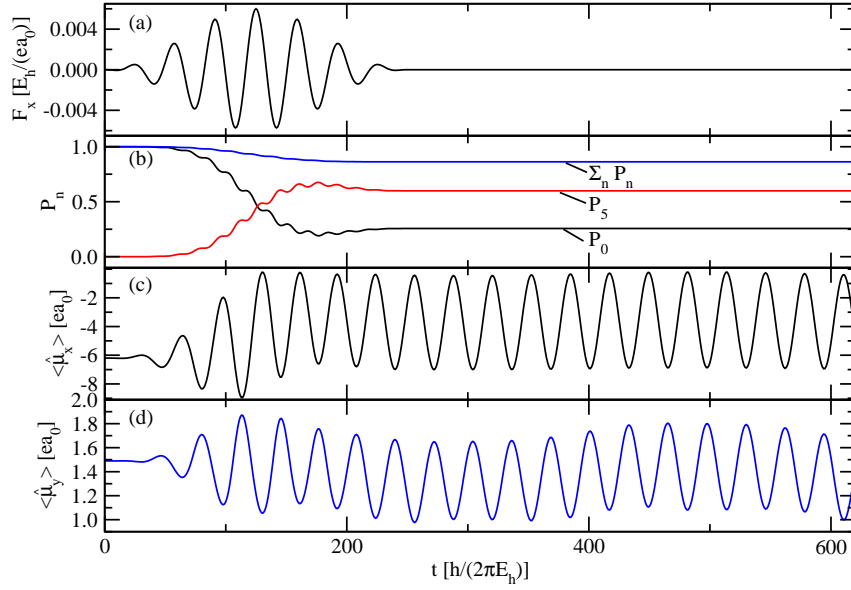


Figure 3.10: Shown is in panel (a) the x -component of the electric field F_x of a non-resonant laser pulse that creates for the BMQ7H system an electronic wavepacket, mainly consisting of states S_0 and S_5 (for details see text). In panel (b), the time-evolution of the populations P_n of these states (P_0 and P_5 , respectively) and of the norm ($\sum_n P_n$) are shown. Panel (c) shows the x -component of the expectation value $\langle \hat{\mu}_x \rangle$ of the resulting dipole moment and panel (d) shows its y -component $\langle \hat{\mu}_y \rangle$.

An alternative analysis is provided by Fourier transforming the dipole moments after the laser pulse is off. This is shown in Fig. 3.11. There, it is seen that the main frequency is exactly the transition frequency $\hbar\omega_{0,5} = 0.1949 E_h$ (5.30 eV). A second frequency $\hbar\omega = 0.0164 E_h$ (0.45 eV) appears for both components which fits to the transition between the states S_3 and S_5 (however, note that the third excited state has a population of 6.9×10^{-3} and is thus weakly populated). The transition dipole moment between these states is $\underline{\mu}_{3,5} = (0.77, 0.56, 0.00)^\dagger \text{ ea}_0$ $((1.96, 1.42, 0.00)^\dagger \text{ D})$. This means there is a coupling between the two states along x and y , but none along z , explaining the weak signal. In the Fourier analysis of the dipole moment along coordinate y shows a third frequency as a weak signal. This frequency has an energy $\hbar\omega = 0.0489 E_h$ (1.33 eV), belonging to the transition between the second and fifth excited state. The small population of 3.5×10^{-4} in the state S_2 and the coupling elements $\underline{\mu}_{2,5} = (0.04, 0.55, 0.00)^\dagger \text{ ea}_0$ $((0.10, 1.40, 0.00)^\dagger \text{ D})$ explain this behavior, *i.e.*, both states are populated, there is a sufficiently high coupling along y , and

almost no coupling along x (and none along z).

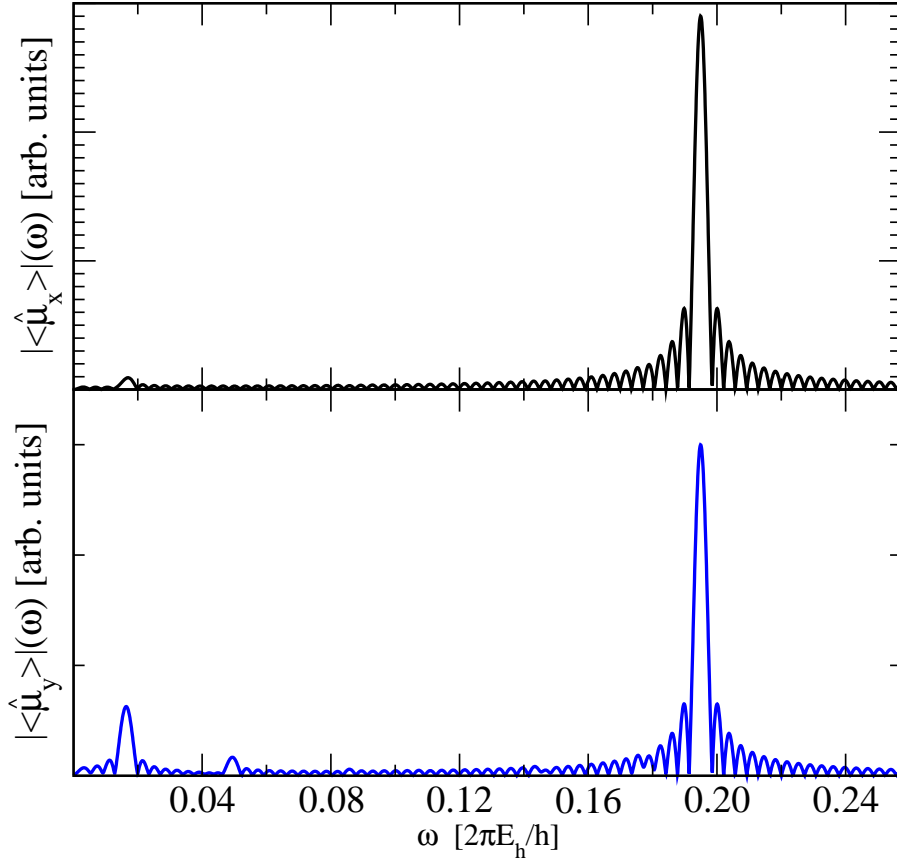


Figure 3.11: Shown are the Fourier transforms of the time-dependent dipole moment along the coordinates x ($|\langle\hat{\mu}_x\rangle|(\omega)$, upper panel) and y ($|\langle\hat{\mu}_y\rangle|(\omega)$, lower panel) for the BMQ7H system.

3.2.3 Pump-probe spectra

Similar to LICN, the electronic wavepacket of the previous section for BMQ7H can also be used for a pump-probe simulation. To this end, a short probe laser pulse is employed: $t_p = 125 \frac{\hbar}{E_h} + \Delta t_p$ ($3.02 \text{ fs} + \Delta t_p$), $\Delta t_p = t_{p,probe} - t_{p,pump}$, $\Delta t_p \in [-112.6; 757.8] \frac{\hbar}{E_h}$ ($[-2.72; 18.33] \text{ fs}$), $\sigma = 12.4 \frac{\hbar}{E_h}$, $\hbar\omega = 0.3675 E_h$ (10.0 eV), $f_0 = 0.1 \frac{E_h}{e a_0}$ ($51.4 \frac{\text{GV}}{\text{m}}$). In two sets of calculations, probe pulses polarized along x and y are tested.

First, the wavepacket is probed with an x -polarized pulse and the loss of norm is calculated after a propagation time of $t_{observ} = 1000 \frac{\hbar}{E_h} + \Delta t_p$ ($24.2 \text{ fs} + \Delta t_p$). The loss of norm as a function of the delay time between the maxima of the pump and the probe pulse is shown in the upper left panel of Fig. 3.12. For the minimal value,

$\Delta t_p = -112.6 \frac{\hbar}{E_h}$ (-2.72 fs), a loss of norm of about 0.83 is observed. For longer delay times, the loss of norm as the probe signal decreases and oscillates within an interval $\bar{N}(\Delta t_p) \in [0.717; 0.807]$. On a first view, two different frequencies can be seen: a high-amplitude and high-frequency motion on the one hand, and on the other hand an oscillation with a lower amplitude and lower frequency as an envelope for the first oscillation. A deeper analysis is done via the Fourier transformation of the loss of norm as shown in the upper right panel of Fig. 3.12. According to this figure, one obtains two frequencies: the major signal has a frequency of $\omega = 0.195 \frac{E_h}{\hbar}$ ($\hbar\omega = 5.3$ eV). This fits exactly to the transition frequency between the ground state and the fifth excited state. This frequency is also present in the dipole moment along the coordinate x of the original wavepacket. The minor signal is at a frequency of $\omega = 0.016 \frac{E_h}{\hbar}$ ($\hbar\omega = 0.44$ eV), which is the transition frequency between states S_3 and S_5 .

The wavepacket can also be probed with an y -polarized pulse (shown in the lower left panel of Fig. 3.12). For the minimal delay time, $\Delta t_p = -112.6 \frac{\hbar}{E_h}$ (-2.72 fs), one obtains a loss of norm of about 0.90. A maximum of 0.93 is seen at a delay time $\Delta t_p = -59.9 \frac{\hbar}{E_h}$ (-1.4 fs). After that, the loss of norm decreases and oscillates finally in an interval $\bar{N}(\Delta t_p) \in [0.564; 0.652]$. A first analysis shows that there are three visible frequencies in these oscillations. The first one is the main carrier frequency that has the highest frequency and a high amplitude. The second one is at a lower frequency that can be seen in the oscillations of the upper envelope. The third corresponds to a frequency between the two previously mentioned ones, and is visible in the oscillations in the lower envelope. A Fourier transform of the time evolution of the loss of norm is shown in the lower right panel of Fig. 3.12. There, it can be seen that the major contribution comes from a frequency of $\omega = 0.195 \frac{E_h}{\hbar}$ ($\hbar\omega = 5.3$ eV). This is exactly the frequency between the two states forming the major part of the original wavepacket (S_0 and S_5). Two other contributions are at $\omega = 0.050 \frac{E_h}{\hbar}$ ($\hbar\omega = 1.4$ eV) (close to the transition frequency $\omega_{2,5}$) and at $\omega = 0.019 \frac{E_h}{\hbar}$ (0.5 eV) (close to $\omega_{3,5}$).

These results lead to the following question: Why is the loss of norm maximal at minimal, negative delay times? This corresponds to an excitation of the electronic ground state using the probe pulse, since the pump pulse has not been applied yet. Since the probe pulse energy (10 eV) is higher than that of the pump pulse (5 eV), higher-energy states are populated initially. Intuitively, one would expect

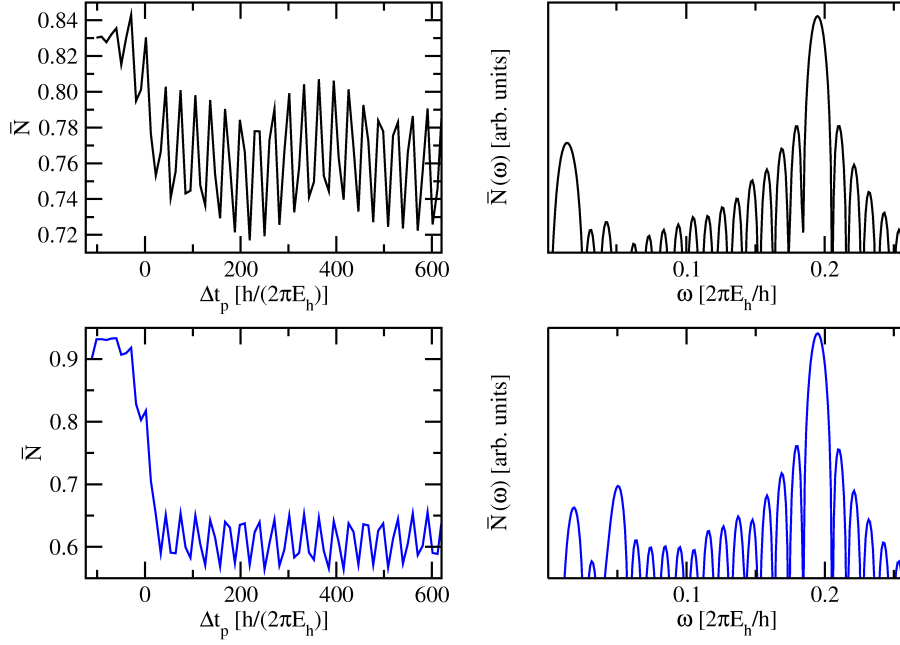


Figure 3.12: Shown is in the upper left panel the loss of norm \bar{N} as a function of the delay time Δt_p when an x -polarized probe pulse is applied to the wave packet generated in Sec. 3.2.2. In the lower left panel, the same is done using a y -polarized probe pulse. The Fourier transforms $\bar{N}(\omega)$ of the respective loss of norm are shown in the upper right (x) and lower right (y) panel. The escape length was set to $d = 1 a_0$ for all calculations.

that \bar{N} should increase for higher initial energies, because then high-energy final continuum states with a larger ionization rate can be reached. However, the results of the pump-probe simulation and the ones obtained for the “ d -scan” for different initial states (see Fig. 3.8) are at variance with the expected result. Second, the loss of norm obtained here is very high. One could argue that in a system with such a high ionization probability, the formation of multiply charged ions cannot be neglected. However, our ionization model does not allow for the formation of multiply charged ions. To avoid artefacts of the model, the intensity of the probe pulse should be decreased such that the ionization rate is still measurable but the formation of multiply charged ions can be neglected.

For further investigation, a frequency scan was done. A probe pulse with varying frequency (but otherwise parameters) was applied to the six non-ionizing states S_0 - S_5 as initial states. Three different pulse frequencies were tested: $\hbar\omega_1 = 0.40 E_h$ (10.9 eV), $\hbar\omega_2 = 0.80 E_h$ (21.8 eV), and $\hbar\omega_3 = 1.20 E_h$ (32.7 eV). The loss of norm is calculated and then plotted with respect to the frequency in Fig. 3.13. There, it it

shown that the loss of norm depends on the frequency of the probe pulse, decreasing with higher pulse energies. Using a pulse with a higher frequency, higher states which have higher ionization rates can be populated temporarily. Another result is the larger loss of norm if the pulses are applied to a system in the electronic ground state, compared to any other non-ionizing initial state. This result disagrees again with expectations.

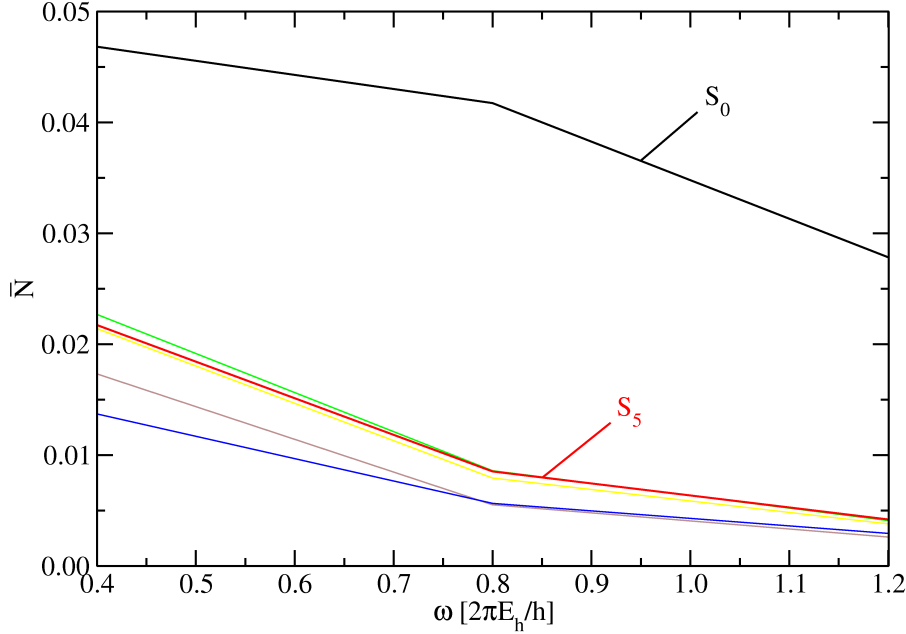


Figure 3.13: Shown is the loss of norm \bar{N} for different initial, non-ionizing states at different pulse frequencies ω within the BMQ7H system. The escape length is set to $d = 1 a_0$. The states forming the target wavepacket, *i.e.*, S_0 and S_5 , are highlighted. The other states are S_1 (brown), S_2 (green), S_3 (blue), and S_4 (yellow).

If the loss of norm decreases for higher probe laser pulse frequencies, there are two possible explanations for this phenomenon. Either the target continuum states have a low ionization rate, or they cannot be populated from the initial states efficiently due to a small transition dipole moment. The latter hypothesis can be tested by comparing transition dipole moments from the ground state and the fifth excited state to all higher states. This is done in Fig. 3.14. There, one can see that the transition dipole moments from the ground state are generally larger than the transition dipole moments from the fifth excited state. This may be rationalized by the simple estimates

$$\langle \hat{\underline{\mu}}_{0,f} \rangle = \langle \Psi_0 | \hat{\underline{\mu}} | \Psi_f \rangle \approx \langle \Psi_0 | \hat{\underline{\mu}} | \Psi_a^r \rangle = - \sum_i e \langle a | \underline{r}_i | r \rangle \quad (3.8)$$

for the transition dipole moment from the ground state Ψ_0 to a final state Ψ_f (expressed in an approximation as a single CSF Ψ_a^r), and

$$\langle \hat{\underline{\mu}}_{5,f} \rangle = \langle \Psi_5 | \hat{\underline{\mu}} | \Psi_f \rangle \approx \langle \Psi_b^s | \hat{\underline{\mu}} | \Psi_a^r \rangle \approx \underline{0} \quad (\text{if } b \neq a \text{ and } s \neq r) \quad (3.9)$$

for the transition dipole moment from the fifth excited state Ψ_5 (also approximated as a single CSF) to a final state.

The second effect emerging from Fig. 3.14 is that the transition dipole moments decrease for transitions to higher excited states. A simple model based on a particle in a one-dimensional box may provide an explanation. For an electron with charge e in a box of length L , the transition dipole moment for transitions from state n to m or vice versa is given as

$$-e \langle \Psi_n | x | \Psi_m \rangle = \begin{cases} \frac{8eL}{\pi^2} \cdot \frac{mn}{(n+m)^2(n-m)^2} & \text{if } (m-n) \bmod 2 = 1 \\ 0 & \text{else} \end{cases} \quad (3.10)$$

where Ψ_n and Ψ_m are the two eigenstates. The transition dipole moment, *e.g.*, from the lowest eigenstate ($m = 1$) to higher states is thus

$$\mu_{1,n} \propto \frac{n}{(n+1)^2(n-1)^2} \quad (3.11)$$

For high-energy target states with large n , this can be simplified to

$$\lim_{n \rightarrow \infty} \frac{n}{(n+1)^2(n-1)^2} = \frac{1}{n^3} \quad (3.12)$$

which also shows the decreasing behavior of transition dipole moments from a defined initial state to all higher target states. Analogous investigations for bound \rightarrow continuum transitions have been also done for the hydrogen atom [98], showing similar behavior. This tells us that the higher states can only be poorly addressed. The other possible explanation (a low ionization rate) is falsified by the upper panel of Fig. 3.9, showing that ionization rates increase with higher final state energy.

In order to decrease the loss of norm and thus the probability of formation of multiply charged ions, the electric field amplitude of the probe pulse is set to $f_{0,probe} = 0.015 \frac{E_h}{E_{a0}}$ ($7.7 \frac{GV}{m}$) which corresponds to 15% of the field amplitude of the probe pulse used before. In this case, the initial loss of norm (at the delay time $\Delta t_p = -112.6 \frac{\hbar}{E_h}$) is about 0.223 and decreases to oscillations of $\bar{N}(\Delta t_p) \in [0.185; 0.206]$ (shown in the left panel of Fig. 3.15). A Fourier transform of these oscillations shows that both frequencies which were observed in the first simulation are still present (right panel of Fig. 3.15).

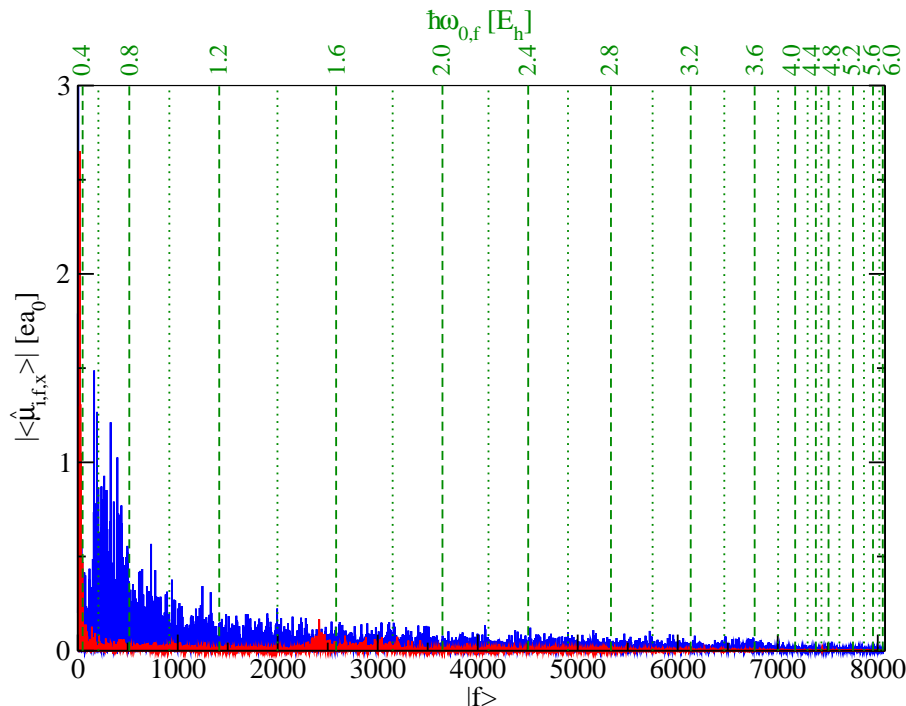


Figure 3.14: Shown are the absolute values of the x -components of the transition dipole moments $|\langle\hat{\mu}_{i,f,x}\rangle|$ for the ground state ($|0\rangle$, blue) and the fifth excited state ($|5\rangle$, red) as initial states $|i\rangle$ to all higher states $|f\rangle$ for the BMQ7H system. The green dashed and dotted vertical lines and the numbers at the top indicate the excitation energies (from the ground state) $\hbar\omega_{0,f}$.

To summarize Secs. 3.1 and 3.2, the calculations have shown that the combined model is a first approximation for the treatment of photoionization using the time-dependent configuration interaction singles method and atom-centered basis sets. It was shown that state-to-state excitations below the ionization potential are still selective, albeit somewhat effected by ionization if laser pulses as considered here were used. Even state-to-state excitations to long-lived target states above the ionization potential are still possible. The ion signal can be used for the probing of electronic wavepackets by pump-probe spectroscopy. The pump-probe simulations lead to results one would intuitively expect. The fact that excited initial states lead to lower ionization probabilities than the ground state can be explained by an analysis of the transition dipole moments for the BMQ7H model system. Nevertheless, one has to remark that the formation of multiply charged ions and the ionization of pre-ionized matter was not considered. The amount of multiple-ionization can be suppressed by using less intense probe pulses, which still lead to clear pump-probe signals.

In the next section, it will be shown that photoionization has not only effects on

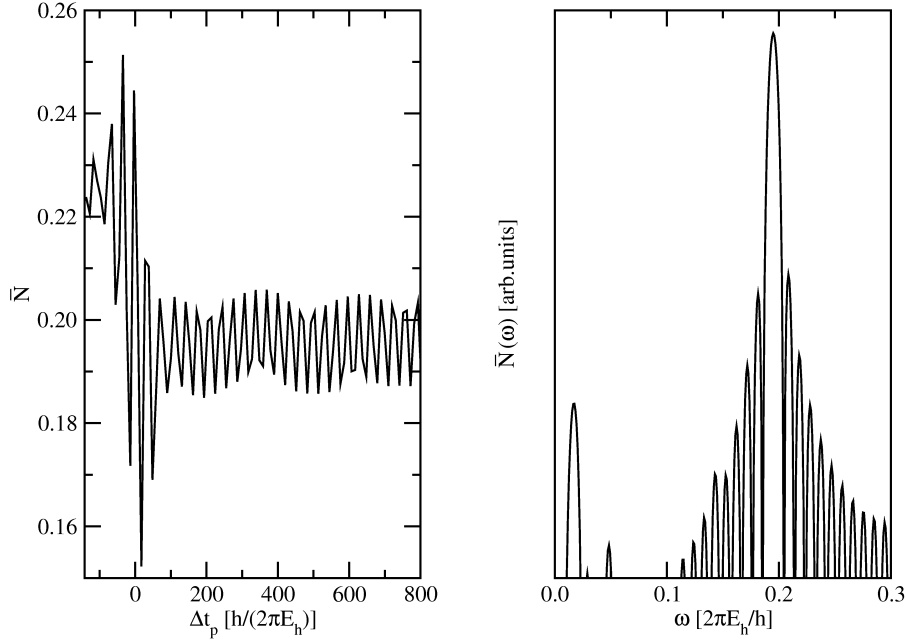


Figure 3.15: Shown is in the left panel the loss of norm \bar{N} for the BMQ7H system after the application of a x -polarized probe pulse with a reduced intensity. In the right panel, the Fourier transform $\bar{N}(\omega)$ of the oscillations in the left panel is shown. The escape length is set to $d = 1 a_0$.

the selectivity of state-to-state excitations or pump-probe excitations, but also on molecular response properties like an induced dipole moment.

3.3 Dynamic polarizabilities for H₂ [78]

In this section, the effect of photoionization on dynamic polarizabilities is investigated. If one applies an external electric field to a system, the electrons begin to move, which changes the dipole moment. According to equation (2.107), one can get information concerning the elements of the polarizability tensor and elements of the higher-order hyperpolarizability tensors. This information can be obtained either as an approximation for weak fields using equation (2.111), or better, by performing a polynomial fit to the Kennlinie [94]. In this work, a quadratic fit is used in order to correct polarizabilities by hyperpolarizability effects.

In the case without photoionization, one expects that the polarizability increases with pulse frequency until the first resonance is reached. At a resonant frequency there is a pole according to the perturbative sum-over-states formula (equation (3.13)). For a higher frequency the polarizability increases again from infinite neg-

ative up to infinite positive values at the next dipole-allowed transition frequency. In the case with photoionization, this behavior is damped.

3.3.1 The H_2 molecule as a test system

In the following, the hydrogen molecule is chosen as a suitable test molecule as it was already investigated using similar methods [32, 99]. Since only two electrons are present, the CISD method corresponds to the Full-CI result in this case. It was shown, that the dynamic polarizabilities calculated by means of TD-CIS and TD-CISD do not differ significantly for the non-ionizing case [32]. Therefore, we restrict to the TD-CIS case in what follows. As a first step, a single point calculation for the hydrogen molecule (oriented along the z -axis, bond length $R_{HH} = 1.39 a_0$ (0.734 Å)) with RHF/cc-pVTZ [100] using the GAMESS 07 program package [97] was performed. The one- and two-electron integrals were taken for a CIS calculation, resulting in excitation energies, permanent dipole moments, and transition dipole moments for 30 CIS states out of 30 molecular orbitals (among these one occupied orbital). Some of the data are given in Tab. 3.3. This table shows that there is only one excited state below the ionization potential. The second excited state is a dark state (for excitation from the ground state, independent of the polarization of the electric field) and should not show up as a pole in the plot for the dynamic polarizability. The third excited state is the first accessible state above the ionization potential.

S_n	E_{exc}^{CIS} [E_h]	$\mu_{0,n,z}$ [ea_0]
0	0.0000	0.0000
1	0.5031	-1.2765
IP	0.5964	—
2	0.6305	0.0000
3	0.9215	+0.6381

Table 3.3: Shown are the excitation energies from the ground state E_{exc}^{CIS} and the transition dipole moments along z for the excitation from the ground state, $\mu_{0,n,z}$ for some of the calculated CIS singlet states S_n in the H_2 molecule. The data was calculated on the CIS [69]/cc-pVTZ [100] level of theory. Additionally, the ionization potential (IP) [77] is indicated.

Laser pulses with different frequencies are applied to the system. The data for all (z -polarized) pulses are the following: $t_p = 2000 \frac{\hbar}{E_h}$ (48.4 fs), $\sigma = 2000 \frac{\hbar}{E_h}$ (48.4 fs), $f_0 = 0.005 \frac{E_h}{e a_0}$ (2.57 $\frac{GV}{m}$). The pulse frequency is varied within the interval $\hbar\omega \in [0.40; 1.00] E_h$ ([10.88; 27.21] eV) in steps of $\hbar\Delta\omega = 0.001 E_h$ (0.03 eV).

The dynamic polarizability in a non-ionizing system is shown as the red dots in Fig. 3.16. The result for the non-ionizing system is as expected. The polarizability increases up to the first excited state S_1 . There is a pole and the sign changes. Then, the polarizability increases again until the transition frequency to the third excited state S_3 is reached. There one finds a second pole, the sign changes again. It has been shown that for TD-CI propagations the resolution of poles at transition frequencies depends on the pulse length. The longer the pulse duration, the better the pole is resolved [99]. Due to this and due to the non-perturbative nature of TD-CI, one does not find real poles with TD-CI in contrast to the sum-over-states formula (equation (2.110)). This can be more clearly seen in the right panel of Fig. 3.16.

For the ionizing system, two different approaches were tested. The first one is the same one as without photoionization, but with a reciprocal escape length of $d^{-1} = 1 a_0^{-1}$ instead of $d^{-1} = 0$ (no ionization). The dipole moment as a function of the electric field is fitted to a quadratic function. The coefficient of the linear term is the polarizability. The other approach is the use of a modified sum-over-states (SOS) formula [93]. Accordingly, the real part of the polarizability tensor elements $\alpha_{qq'}^R$ can be calculated from the transition dipole moment components from ground state to all other states $|n\rangle$, $\mu_{0n,q}$ and $\mu_{n0,q'}$, the transition frequencies ω_{n0} and the ionization rates Γ_n of states $|n\rangle$:

$$\alpha_{qq'}^R(-\omega, \omega) = \sum_{n \neq 0} \left(\frac{\mu_{0n,q} \mu_{n0,q'} (\omega_{n0} - \omega)}{(\omega_{n0} - \omega)^2 + (\frac{1}{2}\Gamma_n)^2} + \frac{\mu_{0n,q} \mu_{n0,q'} (\omega_{n0} + \omega)}{(\omega_{n0} + \omega)^2 + (\frac{1}{2}\Gamma_n)^2} \right) . \quad (3.13)$$

This equation is a result of perturbation theory including dissipation [99], according to which

$$\alpha_{qq'}^R(-\omega, \omega) = \sum_{n \neq 0} \left(\frac{\mu_{0n,q} \mu_{n0,q'} (\omega_{n,0} - \omega)}{(\omega_{n,0} - \omega)^2 + (\gamma_{n,0})^2} + \frac{\mu_{0n,q} \mu_{n0,q'} (\omega_{n,0} + \omega)}{(\omega_{n,0} + \omega)^2 + (\gamma_{n,0})^2} \right) . \quad (3.14)$$

Here, $\gamma_{n,0}$ is a dephasing rate (between the states $|0\rangle$ and $|n\rangle$), which can be written as [81]

$$\gamma_{n,0} = \frac{1}{2} \sum_m (\Gamma_{0 \rightarrow m} + \Gamma_{n \rightarrow m}) + \gamma_{nm}^* . \quad (3.15)$$

Here, γ_{nm}^* is a term which describes a “pure dephasing”. In the case without dissipation, but with photoionization, there is no effect analogous to pure dephasing, thus $\gamma_{nm}^* = 0$. Furthermore, ionization of state $|n\rangle$ can formally be treated as energy relaxation, described by transition rates $\Gamma_{n \rightarrow m}$. The rate for the transition from $|0\rangle$ to $|m\rangle$, $\Gamma_{0 \rightarrow m}$ is assumed to be zero here, because $|0\rangle$ is non-ionizing. The remaining sum term $\sum_m \Gamma_{n \rightarrow m}$, on the other hand, can be interpreted as the ionization rate Γ_n of state $|n\rangle$. The resulting total “dephasing rate” is therefore $\gamma_{n,0} = \frac{1}{2}\Gamma_n$, which was used in equation (3.13).

The curve for the ionizing system using the quadratic fit approach to TD-CIS is plotted as the black line in Fig. 3.16, the one using equation (3.13) is plotted as a blue solid line. One can see that both curves resemble each other as the black curve is mostly covered by the blue one for pulse frequencies $\hbar\omega \geq IP$. Also, it is shown that below the ionization potential the polarizability behaves similar for all three models near the transition frequency to the first excited state S_1 , *i.e.*, TD-CI with and without ionization, and SOS with ionization. Closer inspection shows that the modified SOS formula (equation (3.13)) predicts a pole (since $\Gamma_1 = 0$), while the two TD-CIS methods with finite pulses predict damped poles instead. The differences between TD-CIS with and without ionization are marginal. The second excited state S_2 is – as expected – a dark state and does not produce a pole for any of the three methods. At the transition frequency to the third excited state, there is a damped pole for the approach without photoionization, which is completely washed out for the SOS and the TD-CIS approaches, which include photoionization.

In Fig. 3.17, the dynamic polarizability is shown for the H_2 molecule assuming weaker ionization rates, which can be simulated by choosing a large d value, $d = 1 \times 10^2 a_0$. Also, the pulse length is reduced ($\sigma = 250 \frac{\hbar}{E_h}$ instead of $\sigma = 2000 \frac{\hbar}{E_h}$) in order to show the effects of the pulse length. From the figure, one can see that the poles are damped already at the transition frequency to the non-ionizing first excited state S_1 . This is due to the fact that short pulses lead to less resolved poles in the dynamic polarizability. Also in this example, ionization plays only a minor role for $\hbar\omega < IP$.

We also study the damping at the transition frequency from the ground state to the third excited state. A closer look on the populations can lead to a reasonable explanation why excited states above IP do not produce a pole in the case with photoionization. If the populations of all states at the end of the propagation

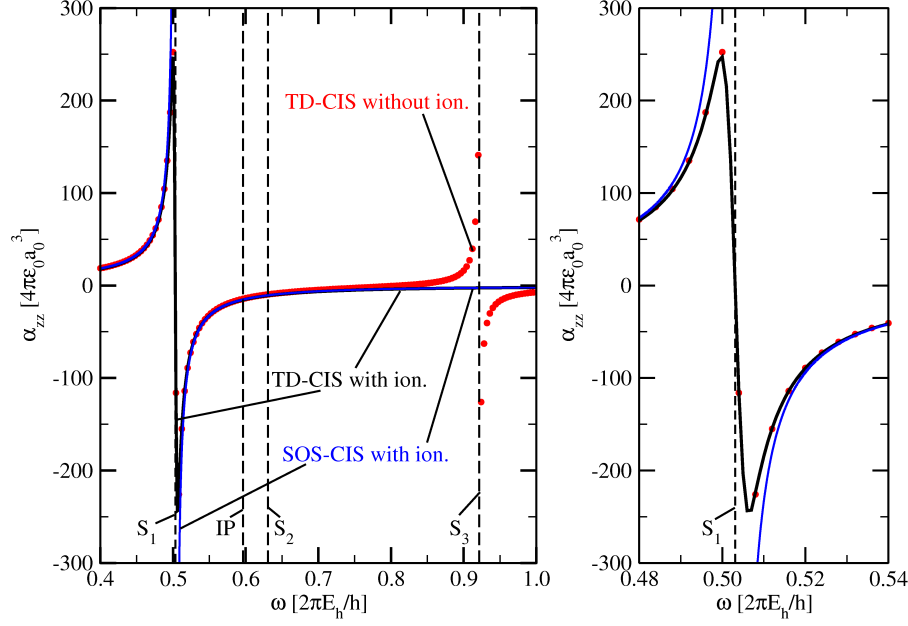


Figure 3.16: Shown is the dynamic polarizability α_{zz} as a function of the frequency ω calculated by three different approaches: the red dots represent a TD-CIS method without photoionization using a quadratic fit of the "kennlinie" [94]. The black curve results from TD-CIS with photoionization, using the same quadratic fit. The blue curve is calculated by means of the SOS formula (equation (3.13)) [93], which includes photoionization. For the methods with photoionization, the escape length parameter is set to $d = 1 a_0$. In the left panel, this is done for a large frequency range ($[0.4; 1.0] \frac{E_h}{h}$). The behavior at the transition frequency for the first excited state (S_1) is plotted in detail on the right. The vertical dashed black lines indicate the transition frequencies to excited states in the frequency range plotted here (S_1, S_2, S_3), and the first ionization potential according to Koopmans' theorem (IP) [77].

(at $t_{final} = 4000 \frac{h}{E_h}$ (96.8 fs)) are compared for a propagation close to the transition frequency $\omega_{3,0}$, once with and once without photoionization, there are significant differences. The main populations in a system without photoionization are in the third excited state ($P_3 = 0.429$), in the ground state ($P_0 = 0.374$) and in the tenth excited state ($P_{10} = 0.197$). The main populations using our model for photoionization are in the ground state ($P_0 = 0.989$), the remaining part is ionized ($\bar{N}(t_{final}) = 0.011$). The other states that are well populated in the non-ionizing case, are unpopulated if ionization is included. Even the maximal populations in these states are very small, *e.g.*, the third excited state ($P_3^{max} = 8.6 \times 10^{-6}$ at $t = 1970 \frac{h}{E_h}$) (47.7 fs) or the tenth excited state ($P_{10}^{max} = 1.4 \times 10^{-10}$ at $t = 1980 \frac{h}{E_h}$) (47.9 fs)). A pole can

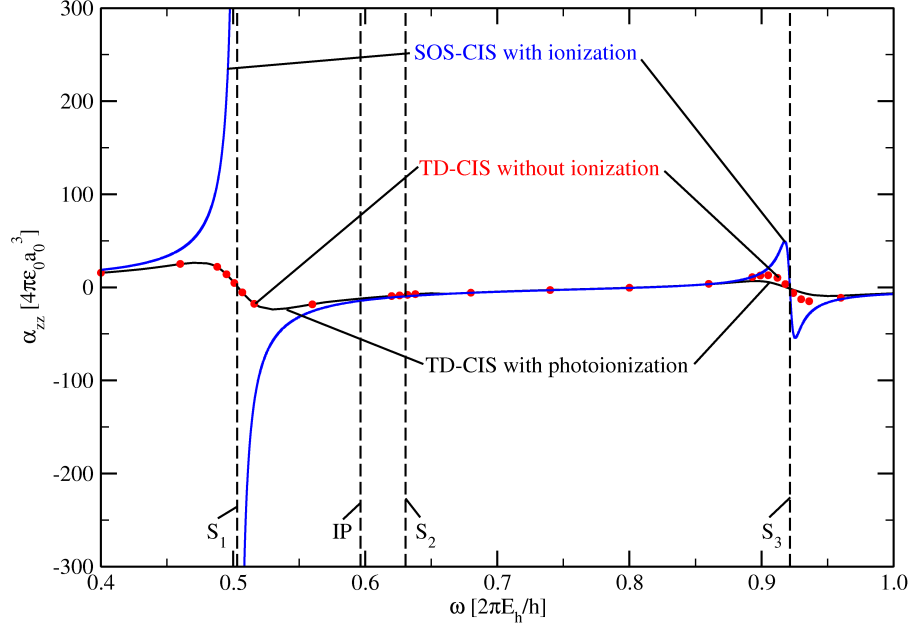


Figure 3.17: Shown is the dynamic polarizability α_{zz} as a function of the frequency ω for a system using lower ionization rates ($d = 1 \times 10^2 a_0$) and shorter pulse lengths (see text), otherwise analogous to Fig. 3.16, left.

only exist if a population transfer to another state occurs and this population is remaining in this state for an infinite time. If the lifetime is finite but long the curve is damped [99]. This can also be seen if the left panel of Fig. 3.16 and Fig. 3.17 are compared to each other. The shorter the lifetime becomes, the more damped is the curve. For an ultrashort lifetime of the third excited state ($\tau_3 = 1.3 \frac{\hbar}{E_h}$ (30.8 as)), the pole is damped so much that the curve is nearly horizontal at this frequency. For $d = 1 \times 10^2 a_0$, an ionization rate of $\Gamma_3 = 7.86 \times 10^{-3} \frac{E_h}{\hbar}$ is obtained. The lifetime increases to $\tau_3 = 127.1 \frac{\hbar}{E_h}$ (3.08 fs) and the curve is only damped to a double peak.

This behavior can be explained by equation (3.13). There, it is said, that the polarizability depends on the transition dipole moments to all higher states, the transition frequencies, and the ionization rates Γ_n . If the ionization rate becomes large with respect to the other frequency term in the denominator, equation (3.13) simplifies to (with $q = q' = z$):

$$\alpha_{zz}^R(-\omega, \omega) \approx \sum_{n \neq 0} \left(\frac{\mu_{0n,z}^2(\omega_{n0} - \omega)}{(\frac{1}{2}\Gamma_n)^2} + \frac{\mu_{0n,z}^2(\omega_{n0} + \omega)}{(\frac{1}{2}\Gamma_n)^2} \right) = \sum_{n \neq 0} \frac{8\mu_{0n,z}^2\omega_{n0}}{\Gamma_n^2} \quad (3.16)$$

and is thus not frequency-dependent.

We finally note that around S_3 , the three models lead to different damped poles according to Fig. 3.17. TD-CIS with finite pulse width and with photoionization

shows the strongest damping, followed by TD-CIS with finite pulse width and without photoionization, and finally SOS with photoionization. Thus, both finite pulse width and photoionization influence polarizabilities, in particular around poles above IP.

3.4 State-to-state excitations in a dissipative environment [79]

Besides finite pulse width and ionization, also dissipation affects electron dynamics. In Ref. [79], several molecules are investigated, *e.g.*, the hydrogen molecule (H_2) and the BMQ7H molecule. In this section, we focus on the results for the H_2 molecule. We simulated several state-to-state excitations of the hydrogen molecule in the presence of photoionization and dissipation. For this purpose, the model presented in Sec. 2.4.2 is used.

3.4.1 System states and ionization rates

The hydrogen molecule is treated as a toy model for this theory. Therefore, a first calculation is done, at the CIS(D) [101] level of theory using Dunning’s aug-cc-pVQZ basis. In CIS(D) the contribution of double excitations to the energies are added perturbatively. Still, we use the same ionization rates as in CIS using the same basis. If a state has a CIS energy above IP but a CIS(D) energy below it, the state is counted as non-ionizing. The excitation energies, dipole moments, and lifetimes with respect to ionization are shown in Tab. 3.4.

From this table, one can see that there are five non-ionizing excited states on the CIS(D)/aug-cc-pVQZ level. In contrast, we have only one non-ionizing excited state for CIS/6-31G*. This is due to the fact, that we use another method and another basis now. Two of the excited states, namely the first and the fifth excited state, can be populated using a single z -polarized π -pulse. The fifth excited state can also be populated stepwise, *i.e.*, by a pulse sequence using the first and the second excited state as intermediate states.

For the dynamical simulations, the lifetimes of the excited states with respect to dissipation are scaled to the femtosecond regime, *e.g.*, $1/\zeta_{1 \rightarrow 0} = 45 \text{ fs}$ to model an electron-rich environment, *e.g.*, a surface.

S_n	E_n^{exc} [E_h]	$\mu_{0,n,z}$ [ea_0]	$\mu_{1,n,z}$ [ea_0]	$\mu_{2,n,z}$ [ea_0]	τ_n [$\frac{\hbar}{E_h}$]	$\zeta_{5 \rightarrow n}$ [$\frac{E_h}{\hbar}$]
0	0.0000	0.0000	+0.9949	0.0000	∞	5.0×10^{-4}
1	0.4705	+0.9949	0.0000	-2.9641	∞	2.0×10^{-30}
2	0.4844	0.0000	-2.9641	0.0000	∞	1.6×10^{-5}
3	0.5152	0.0000	0.0000	0.0000	∞	7.0×10^{-30}
4	0.5152	0.0000	0.0000	0.0000	∞	8.0×10^{-30}
5	0.5683	-0.7236	0.0000	-2.2665	∞	—
IP	0.5945	—	—	—	—	—
6	0.6219	0.0000	+1.7695	0.0000	2.1443	—
\vdots	\vdots	\vdots	\vdots	\vdots	\vdots	\vdots
9	0.6464	0.0000	-1.4500	0.0000	2.0329	—
\vdots	\vdots	\vdots	\vdots	\vdots	\vdots	\vdots
91	9.5969	0.0000	0.0000	0.0000	0.3207	—

Table 3.4: Shown are the excitation energies $E_{n,exc}$, the transition dipole moments along z from the ground state, $\mu_{0,n,z}$, from the first excited state, $\mu_{1,n,z}$, and the second excited state, $\mu_{2,n,z}$, and the lifetimes with respect to photoionization, τ_n , for some states S_n in the H_2 molecule. Also, the dissipation rates from the fifth excited state to all lower states, $\zeta_{5 \rightarrow 0}$, are shown. The data was obtained in a CIS(D) calculation using Dunning’s aug-cc-pVQZ basis.

3.4.2 Laser-driven state-to-state excitations

3.4.2.1 Direct excitation

First, it is attempted to populate S_5 directly, *i.e.*, with a single π -pulse. This pulse is z -polarized, with the parameters: $\sigma = t_p = 496.1 \frac{\hbar}{E_h}$ (12.0 fs), $\hbar\omega = 0.5683 E_h$ (15.46 eV), $f_{0,z} = 0.0044 \frac{E_h}{ea_0}$ (2.25 $\frac{GV}{m}$). The resulting populations for some states of the hydrogen molecule are shown in Fig. 3.18, once without photoionization and without any coupling to an environment (panel (a)), once without photoionization in a dissipative environment (panel (b)), once with photoionization, but without a coupling to the environment (panel (c)), and once with photoionization in a dissipative environment (panel (d)).

In Fig. 3.18, it can be seen that the excitation is selective, if the molecule is not

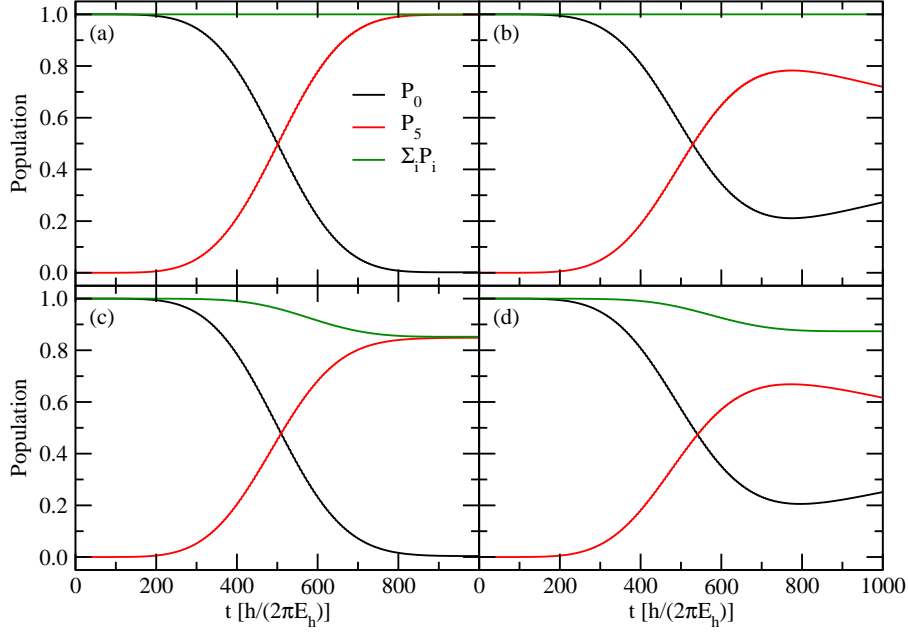


Figure 3.18: Shown are the population of the ground state, P_0 , the population of the fifth excited state, P_5 , and the norm, $\sum_i P_i$, for the H_2 molecule during a π -pulse excitation. This is done for a free molecule in vacuum without photoionization in panel (a), for a molecule in a dissipative environment in panel (b), for a molecule in vacuum with photoionization in panel (c), and for a molecule in a dissipative environment with photoionization in panel (d).

coupled to an environment. In this case, the excitation leads to a complete population inversion (despite some ionization losses, if photoionization is considered). If the molecule is coupled to a dissipative environment, a population inversion does not take place, as the population is transferred back to the electronic ground state. In the case where both photoionization and a coupling to an electron-rich environment are considered, the effects seem to be treated independently. The loss of norm at the end of the propagation is slightly reduced in panel (d), as the relaxation to the ground state reduces the possibility of multi-photon excitations. So, dissipation also has effects on photoionization.

As already stated above, it is also possible to perform a stepwise population of our target state. For this purpose, a π -pulse sequence is used targeting the states

$$S_0 \rightarrow S_1 \rightarrow S_2 \rightarrow S_5 \quad . \quad (3.17)$$

The parameters of the pulses are chosen as follows. The first pulse is polarized along z , with $\hbar\omega = 0.4705 E_h$ (12.8 eV), $t_p = \sigma = 248.0 \frac{\hbar}{E_h}$ (6.0 fs), $f_{0,z} = 0.0127 \frac{E_h}{\text{ea}_0}$

($6.53 \frac{\text{GV}}{\text{m}}$). The second pulse is equally polarized with $\hbar\omega = 0.0139 E_h$ (0.378 eV), $t_p = 992.2 \frac{\hbar}{E_h}$ (24.0 fs), $\sigma = 496.1 \frac{\hbar}{E_h}$ (12.0 fs), $f_{0,z} = 0.0022 \frac{E_h}{ea_0}$ ($1.13 \frac{\text{GV}}{\text{m}}$). The third pulse is also z -polarized with $\hbar\omega = 0.0839 E_h$ (2.28 eV), $t_p = 1736.3 \frac{\hbar}{E_h}$ (42.0 fs), $\sigma = 248.0 \frac{\hbar}{E_h}$ (6.0 fs), $f_{0,z} = 0.0839 \frac{E_h}{ea_0}$ ($43.1 \frac{\text{GV}}{\text{m}}$).

The resulting population dynamics for all four considered cases (molecule in vacuum with and without photoionization, molecule coupled to an electron-rich environment with and without photoionization) is shown in Fig. 3.19. One can see that the last pulse is not selective for the free molecule in vacuum without photoionization. The target state S_5 has a final population of about $P_5(t_{final}) = 0.317$ (with $t_{final} = 2000 \frac{\hbar}{E_h}$), while the ninth excited state has an even higher population ($P_9(t_{final}) = 0.536$). This happens due to the high intensity of the third pulse. Population in the fifth excited state is transferred to the ninth excited state by the same pulse which populates the state S_5 (the transition dipole moment is $\mu_{5,9,z} = -2.7076 ea_0$ (-6.88 D)). In a dissipative environment, the population in the target state S_5 and the even higher populated S_9 are lower than in the case of the molecule in vacuum ($P_5(t_{final}) = 0.189$ and $P_9(t_{final}) = 0.332$). The reason for this is the finite lifetime of all excited states, that transfers the population back to the electronic ground state ($P_0(t_{final}) = 0.377$). If all electronic states above the ionization potential are assigned a finite lifetime due to photoionization, the selectivity of the third pulse increases up to $P_5(t_{final}) = 0.834$. This is almost a complete population inversion, as the norm is reduced to $N(t_{final}) = 0.844$. The ninth excited state remains unpopulated and does not play any role here. In the description with photoionization and a coupling to an electron-rich environment, the selectivity of the last pulse increases also compared to the case with dissipation but without photoionization. The final target state population is $P_5(t_{final}) = 0.485$. This confirms that photoionization can lead to improved pulse selectivities. Another effect is that the norm is here at $N = 0.873$, which is a bit higher than in the case without the coupling to a dissipative environment. This behavior was also visible for the direct excitation in Fig. 3.18. Dissipation leads to a lower loss of norm.

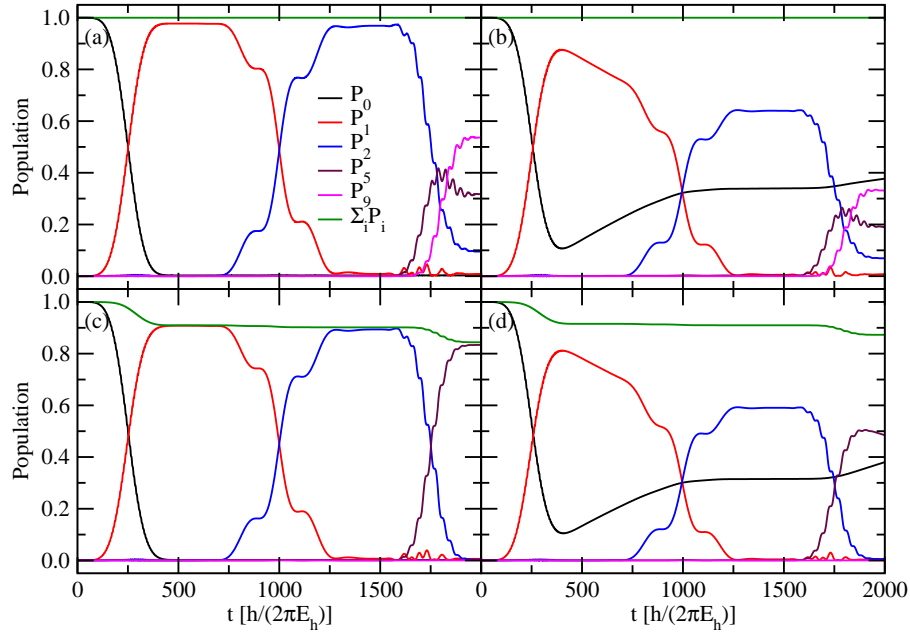


Figure 3.19: Shown is the temporal evolution of the populations of the ground state, P_0 , the first excited state, P_1 , the second excited state, P_2 , the fifth excited state P_5 , the ninth excited state P_9 , and the sum of the populations of all states, $\sum_i P_i$, of the H_2 molecule during a series of four non-overlapping π -pulses along the path $S_0 \rightarrow S_1 \rightarrow S_2 \rightarrow S_5$. In panel (a), this is simulated for the free molecule in vacuum without photoionization. In panel (b), the molecule is coupled to an electron-rich environment. In panel (c), the population dynamics for a molecule in vacuum with photoionization is shown. Panel (d) shows the time-evolution of the populations for a molecule coupled to a dissipative environment with photoionization.

Chapter 4

Treatment of correlation and calculation of the single electron entropy

In this chapter, electron correlation and correlation effects are investigated. Whenever two or more electrons are close to each other in a molecule, electron correlation leads to a lower energy compared to the uncorrelated wavefunction. An uncorrelated method, *e.g.*, Hartree-Fock, does only account for the interaction between an electron and the average field arising from all the other electrons. Correlated methods like the complete active space self-consistent field method (CASSCF) or configuration interaction methods (CI, with at least double excitations) decrease the ground state energy because they include more than one Slater determinant (unlike HF).

As a measure for the electron correlation, the single electron entropy (SEE) of a molecule can be calculated from a reduced one electron density matrix [102]. Here, one electron density matrices are used, as the entropy for N electron density matrices representing a pure state, *i.e.*, a state which is determined by a single wavefunction, is always equal to zero. The SEE is zero for a Hartree-Fock ground state wavefunction but it increases quickly when the wavefunction is propagated using a correlated method. This leads also to the question if the SEE can be lowered if the system is excited photophysically, *i.e.*, if the electrons can be decorrelated at will. In this chapter, it is attempted to control the single electron entropy using laser pulses. As the SEE is suggested to be a correlation measure, its control is a possibility to generate a Hartree-Fock state from a correlated state.

This chapter is organized as follows: In Sec. 4.1.1, the relation between the correlation energy and the suggested correlation measures is checked for a minimal basis model of H_2 . In Sec. 4.1.2, the potential energy curves of the H_2 molecule for two wavefunction-based correlated methods (CISD and MCTDHF) are calculated and on the one hand, compared to each other, on the other hand, they are compared to uncorrelated method (RHF). The RHF state is then propagated in real time, and the entropy is obtained as well as another suggested correlation measure, the quantum impurity (QI). These two measures are compared to each other using an extended basis set in Sec. 4.1.3. In Sec. 4.2, we consider the control of the SEE. First, the Hartree-Fock ground state is used as a target wavefunction in a calculation using the optimal control theory, starting from the correlated ground state. It was attempted to decrease the SEE to a value much lower than the one of the CISD ground state. In a further section, Sec. 4.2.1.3, it is proved that a stochastic laser pulse optimization algorithm is more appropriate to achieve low single electron entropies. In Sec. 4.2.2, we report on attempts to generate a low SEE which are stable over longer time intervals. In the following, the terms “entropy” and “SEE” are used synonymous with the single electron entropy.

4.1 Correlation and entropy: Foundations

4.1.1 Minimal basis model of H_2

Within the minimal basis (MB) model for H_2 , two spatial orbitals ψ_1 and ψ_2 are considered. These are used to test the relation between the correlation energy E_{corr} , the single electron entropy S , and the quantum impurity Ω .

The H_2 Full-CI ground state is, in intermediate normalization,

$$\Phi_0 = \Psi_0^{HF} + A|2\bar{2}\rangle \quad (4.1)$$

with the Hartree-Fock ground state

$$\Psi_0^{HF} = |1\bar{1}\rangle \quad (4.2)$$

and the doubly excited determinant $|2\bar{2}\rangle$. Single excitations do not contribute to the correlated ground state due to symmetry. In the H_2 minimal basis model, the coefficient A and the correlation energy E_{corr} can be calculated analytically

according to [63]:

$$A = -\frac{K_{12}}{E_{corr} - 2\Delta} \quad , \quad (4.3)$$

$$E_{corr} = \Delta - \sqrt{\Delta^2 + K_{12}^2} \quad (4.4)$$

with $2\Delta = 2(\varepsilon_2 - \varepsilon_1) + J_{11} + J_{22} - 4J_{12} + 2K_{12}$. In these equations, ε_i is the energy of orbital i , $J_{ij} = \langle ij|ij \rangle$ is a Coulomb integral, and $K_{ij} = \langle ij|ji \rangle$ is an exchange integral. All orbital energies and two-electron integrals depend on the internuclear distance R_{HH} . In Fig. 4.1, the correlation energy $E_{corr}(R_{HH})$, the coefficient $A(R_{HH})$, the RHF energy

$$E_{RHF} = 2h_{11} + J_{11} \quad , \quad (4.5)$$

where h_{11} is a one-electron integral, and the Full-CI (FCI) energy

$$E_{FCI} = E_{RHF} + E_{corr} \quad (4.6)$$

are shown, all calculated for the STO-3G basis set. For very large bond lengths ($R \rightarrow \infty$), one can treat the hydrogen molecule as two single hydrogen atoms. It follows, that the orbital energies are equal ($\varepsilon_2 - \varepsilon_1 = 0$) and $K_{12} = -\frac{1}{2}J_{11}$; as a consequence, Δ becomes zero. The correlation energy in the long-range limit is

$$\lim_{R_{HH} \rightarrow \infty} E_{corr} = -K_{12} = -0.3873 \text{ E}_h \quad (4.7)$$

and the respective coefficient

$$\lim_{R_{HH} \rightarrow \infty} A(R_{HH}) = -1 \quad , \quad (4.8)$$

i.e., the ground state is an equal mixture of $|1\bar{1}\rangle$ and $|2\bar{2}\rangle$.

We now come to the other suggested correlation measures, *i.e.*, the entropy

$$S = -k_B \text{Tr}\{\underline{\underline{\gamma}} \ln \underline{\underline{\gamma}}\} \quad (4.9)$$

and the quantum impurity

$$\Omega = 1 - \frac{1}{2} \text{Tr}\{\underline{\underline{\gamma}}^2\} \quad . \quad (4.10)$$

For functions of matrices as its natural logarithm, please refer to Appendix A. In the minimal basis model for the H_2 molecule, the one-matrix for the correlated ground state Φ_0 in the basis of Hartree-Fock spin orbitals $\chi_i(\underline{x}_j)$ ($i, j = 1, 2$), is

$$\gamma_{ij} = \int d\underline{x}_1 d\underline{x}'_1 \chi_i^*(\underline{x}_1) \gamma(\underline{x}_1, \underline{x}'_1) \chi_j(\underline{x}'_1) \quad (4.11)$$

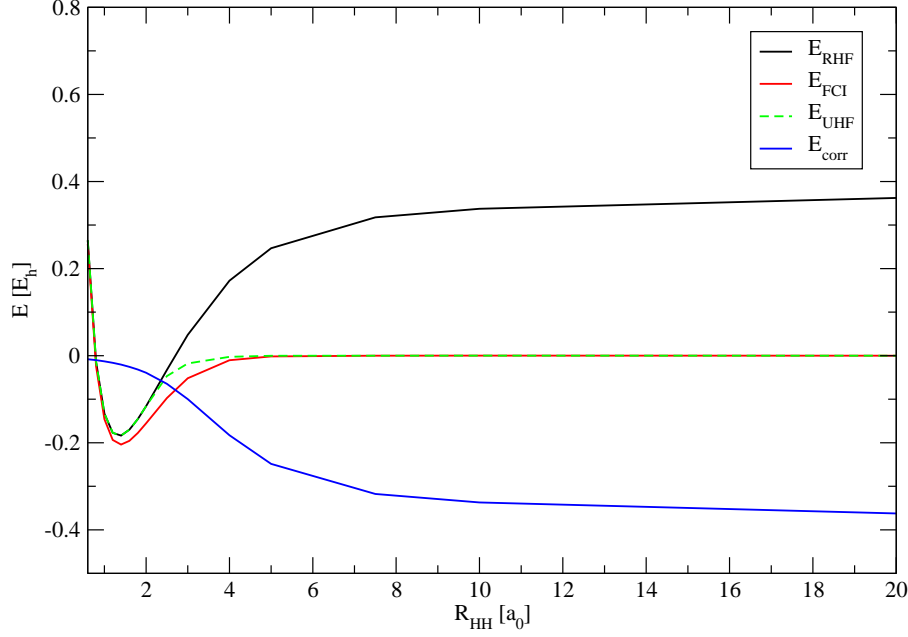


Figure 4.1: Shown are the RHF energy, E_{RHF} , the Full-CI energy, E_{FCI} , and the correlation energy, E_{corr} , as a function of the interatomic distance, R_{HH} , for the H_2 molecule using a minimal basis set (STO-3G).

with

$$\gamma(\underline{x}_1, \underline{x}'_1) = 2 \int d\underline{x}_2 \Phi_0(\underline{x}_1, \underline{x}_2) \Phi_0^*(\underline{x}'_1, \underline{x}_2) \quad , \quad (4.12)$$

can be calculated analytically as

$$\gamma_{ij} = \delta_{i1}\delta_{1j} + \delta_{i\bar{1}}\delta_{\bar{1}j} + A^2\delta_{i2}\delta_{2j} + A^2\delta_{i\bar{2}}\delta_{\bar{2}j} \quad (4.13)$$

resulting in

$$\underline{\underline{\gamma}} = \begin{pmatrix} 1 & 0 & 0 & 0 \\ 0 & 1 & 0 & 0 \\ 0 & 0 & A^2 & 0 \\ 0 & 0 & 0 & A^2 \end{pmatrix} \quad . \quad (4.14)$$

After renormalization ($\text{Tr}\{\underline{\underline{\gamma}}\} = 2$), the one-matrix gives

$$\underline{\underline{\gamma}} = \frac{1}{1+A^2} \begin{pmatrix} 1 & 0 & 0 & 0 \\ 0 & 1 & 0 & 0 \\ 0 & 0 & A^2 & 0 \\ 0 & 0 & 0 & A^2 \end{pmatrix} \quad . \quad (4.15)$$

The single electron entropy is then also given analytically as

$$\frac{S}{k_B} = -\frac{2}{1+A^2} \left[\ln \left(\frac{1}{1+A^2} \right) + A^2 \ln \left(\frac{A^2}{1+A^2} \right) \right] \quad . \quad (4.16)$$

For the two considered limiting cases, namely the Hartree-Fock wavefunction ($A = 0$) and the Full-CI solution at an infinite bond length ($A = -1$), the calculated single electron entropies according to the von Neumann definition are $S = 0$ (HF) and $S = 2k_B \ln(2) \approx 1.38k_B$ (Full-CI).

Also, the quantum impurity Ω can be calculated analytically as

$$\Omega = 1 - \frac{1 + A^4}{(1 + A^2)^2} \quad , \quad (4.17)$$

which is $\Omega = 0$ for $A = 0$ (Hartree-Fock), and $\Omega = \frac{1}{2}$ for $A = -1$ (Full-CI, $R \rightarrow \infty$).

The correlation measures are both shown in Fig. 4.2.

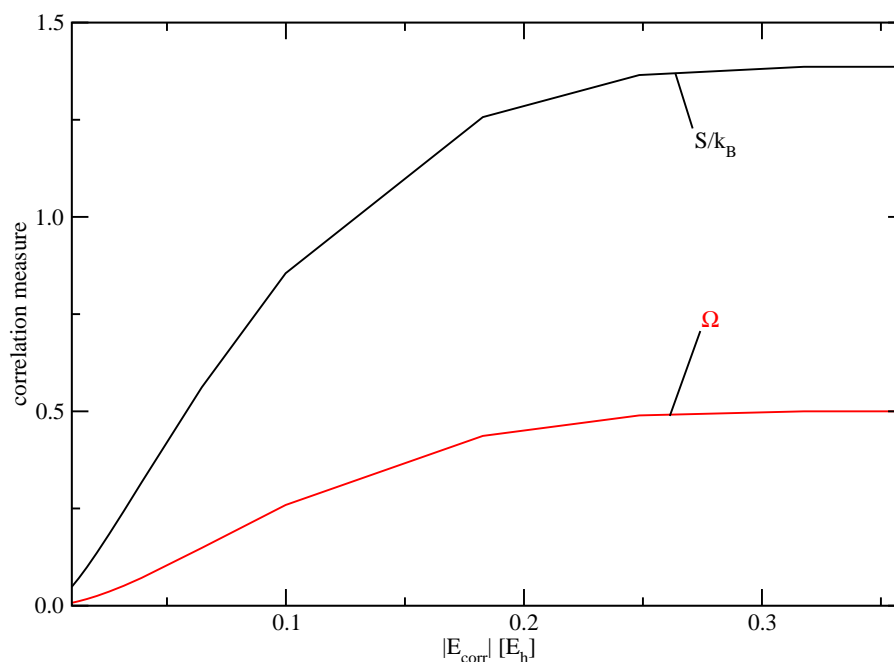


Figure 4.2: Shown are the single electron entropy S (in units of Boltzmann's constant k_B) and the quantum impurity Ω as a function of the modulus of the correlation energy, $|E_{\text{corr}}|$, for the H_2 molecule using the STO-3G basis set.

From Fig. 4.2, one can see, that both suggested correlation measures increase monotonically with higher $|E_{\text{corr}}|$, suggesting that S and Ω can indeed be used as useful correlation measures.

4.1.2 Extended basis sets

We now consider the hydrogen molecule H_2 using an extended basis set. We also consider different methods to obtain potential energy curves, namely restricted Hartree-Fock (RHF), unrestricted Hartree-Fock (UHF), MCTDHF (for two electrons within

two or more, up to ten orbitals), and Full-CI at different interatomic distances. For RHF and UHF, the energies are obtained from GAMESS 07 [97] calculations. For Full-CI, they are obtained from a CISD program [30]. Finally, the MCTDHF results are obtained from a MCTDHF program [103] that uses sorted one- and two-electron integrals out of a GAMESS 07 RHF calculation. In the MCTDHF calculation, the wavefunction is propagated in imaginary time as long as necessary to reach the ground state energy. This algorithm is described in Appendix B. The basis set is aug-cc-pVTZ [100] for all calculations, that is, we have 50 molecular orbital for H_2 .

The results of these calculations are plotted in the upper panel of Fig. 4.3. There, one can again see, that the RHF energy is much too high for large interatomic distances. The energy does not reach the theoretical value for two free hydrogen atoms ($-0.5 E_h$ per atom). The well-known reason is that RHF considers doubly occupied or non-occupied spatial orbitals [63]. In the case of dissociation of the hydrogen molecule, an UHF wavefunction with two singly occupied orbitals is a more appropriate description. The MCTDHF and CISD energies include dissociation correctly but their energies near the equilibrium distance $R_{HH}^0 = 1.388 a_0$ (0.734 \AA) are lower than the UHF energy. Also, the correlation energy, defined here as $E_{corr} = E_{correlated\ method} - E_{RHF}$ [104] is plotted in the lower panel of Fig. 4.3. There, it is shown that the effect of correlation is maximal at large distances, *i.e.*, $R_{HH}^{max} \approx 9.4 a_0$ (5.0 \AA), corresponding to an extended bond length. One can determine the regions where different types of correlation dominate. For interatomic distances of $R_{HH} \in [0.8; 2.5] a_0$ ($[0.4; 1.3] \text{ \AA}$), there is a small difference between MCTDHF methods (with at least 6 orbitals in the active space), and the CISD result. That is the region where dynamic correlation dominates which is well described by CISD, but insufficiently described by MCTDHF. A special case is MCTDHF(N, K) (with N as the number of all electrons and K being the number of all molecular orbitals), which is the same as TD-Full-CI. In a second region ($R_{HH} \in [2.5; 7.6] a_0$ ($[1.3; 4.0] \text{ \AA}$)), the CISD and MCTDHF curves are very close to each other. There, non-dynamic or static correlation is dominant. Here, a small number of doubly excited configurations is enough to correct for the ionic nature of the HF determinant. This type is well described by all of the multi-determinant methods.

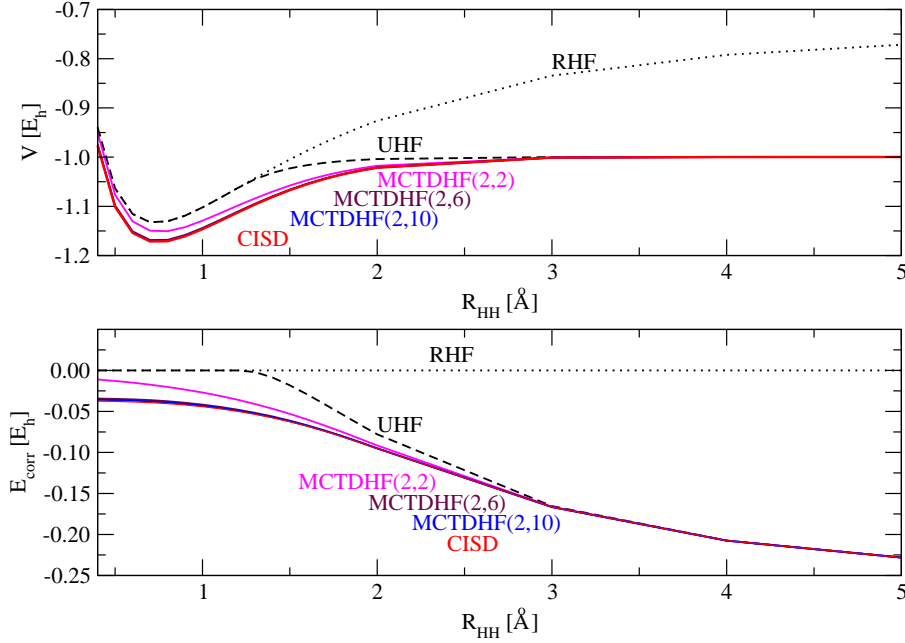


Figure 4.3: Shown are in the upper panel the potential energy curve V for the ground state of the hydrogen molecule with respect to the interatomic distance R_{HH} . For this quantity, several different methods are used, such as RHF (black dotted line), UHF (black dashed line), MCTDHF(2,2) (magenta solid line), MCTDHF(2,6) (maroon solid line), MCTDHF(2,10) (blue solid line), and CISD (red solid line). Recall, that the notation MCTDHF(2, M) denotes two electrons in an active space of M spatial orbitals. In the lower panel the correlation energy E_{corr} is plotted against the interatomic distance. As an uncorrelated reference, the RHF potential energy curve is used [104]. The basis set for all methods is aug-cc-pVTZ [100].

4.1.3 Dynamical aspects

In this section, entropy and quantum impurity as two different measures for the correlation during the propagation of a wavefunction for small molecular systems are calculated. The results of these measures are compared to each other. One can also see from the time-evolution of the SEE, how fast the SEE builds up, starting from an uncorrelated state.

For the calculation of the SEE, it is necessary to compute from the time-dependent wavefunction (either from MCTDHF or from TD-CI), a reduced one electron density matrix. From this density matrix, the SEE is calculated directly via equation (2.80). An alternative estimate for the electron correlation is the quantum impurity Ω , defined in equation (4.10)

For a single Slater determinant, Ω is always 0, while for a state consisting of more than one determinant, $\Omega > 0$.

In a first set of calculations, the different measures for the correlation, *i.e.*, SEE and QI, will be compared to each other. The hydrogen molecule is used as a model system again. For this molecule, a RHF/6-31G** [95] calculation (H-H bond along z , $R_{HH} = 1.380 a_0$ (0.730 Å)) was performed using the GAMESS 07 program package [97], *i.e.*, we have ten molecular orbitals. The one- and two-electron integrals are then used for a MCTDHF(2,10) calculation on the one hand and for a TD-CISD calculation on the other hand. As both methods account for all excitations within all 10 molecular orbitals, both correspond to TD-Full-CI and should be identical. Both of the time-dependent wavefunctions are transformed to the reduced density matrix representation. From this reduced one electron density matrix, the time-dependent SEE is then calculated for TD-CISD, for MCTDHF(2,10) the SEE and Ω are calculated. Both calculations start from the RHF ground state wavefunction.

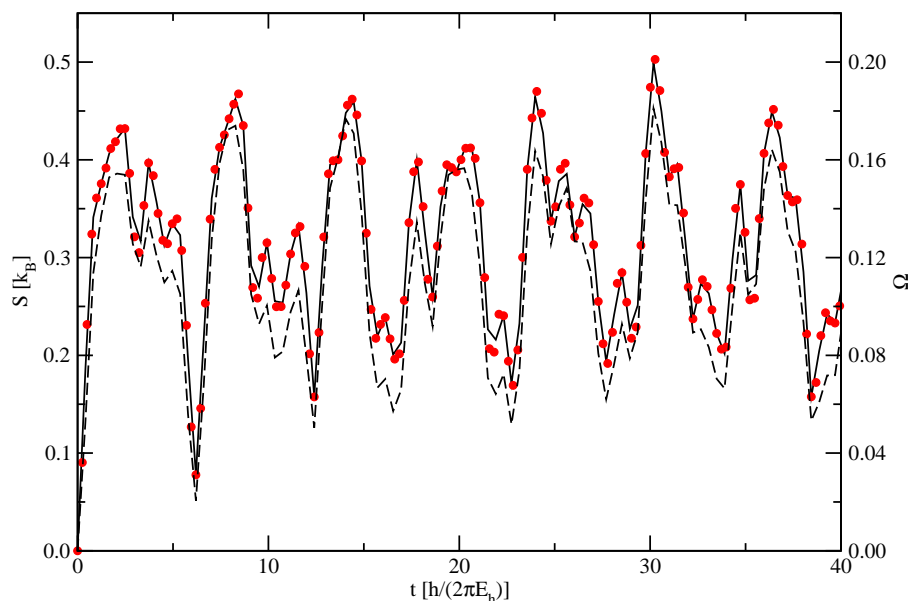


Figure 4.4: Shown is the time-evolution of the SEE S for the H_2 molecule using different methods and the 6-31G** basis set, starting from the RHF ground state. The black curves represent quantities based on the MCTDHF(2,10) method. The dashed line is the QI Ω according to equation (4.10), the solid line represents the entropy calculated by means of equation (2.80). The red dots indicate a SEE calculated with the TD-CISD method and equation (2.80).

These SEEs are shown in Fig. 4.4. On a first view, one sees that the two

methods TD-CISD and MCTDHF (red dots and black solid line) lead to the same SEE ($S \in [0.08; 0.53] \text{ k}_B$), as they should. The QI based on equation (4.10) shows qualitatively the same time-dependence. We will focus on the SEE in the following. However, note, that SEE and QI agree in general very well, *e.g.*, all minima and maxima occur at the same times.

Another effect that can be seen from Fig. 4.4 is that the initial SEE, *i.e.*, $S_0 = 0$, increases very fast. It rises from zero to a first maximum within an initial rise time of $t_{ir} \approx 2.5 \frac{\hbar}{E_h}$ (60 as). This can be interpreted as the time the electrons need to correlate. One may also calculate a “correlation length” as $r_c = v_{el} \cdot t_{ir} \approx 1 \frac{\hbar}{m_e a_0} \cdot 2.5 \frac{\hbar}{E_h} = 2.5 a_0$.

In general, the time-evolution of the SEE shows oscillations. These oscillations can be explained as follows. The RHF initial state Ψ_0^{HF} can be written as a linear combination of correlated states Φ_n , *i.e.*,

$$\Psi_0^{HF} = \sum_n C_n \Phi_n \quad . \quad (4.18)$$

For instance, in the H_2 minimal basis model using CID (CI doubles), we have two eigenstates Φ_0 and Φ_1 contributing to Ψ_0^{HF} according to equation (4.18). The time-evolution of the wavefunction is given as

$$\Psi(t) = e^{-E_1 t/\hbar} \cdot [C_0 \cdot e^{i\omega_{10} t} \Phi_0 + C_1 \Phi_1] \quad (4.19)$$

where $\omega_{10} = \frac{E_1 - E_0}{\hbar}$ derives from the correlated energies E_1 and E_0 of Φ_1 and Φ_0 . It can be shown that in this model, both the entropy S and the quantum impurity Ω oscillate, starting from $S = 0$ and $\Omega = 0$, with a single period

$$T = \frac{2\pi}{\omega_{10}} \quad . \quad (4.20)$$

If, as in Fig. 4.4, several CISD states Φ_n form a wavepacket, the HF state Ψ_0^{HF} , this leads to a reduced one electron density matrix of the form

$$\gamma(\underline{x}_1, \underline{x}_{1'}) = 2 \sum_n \sum_m C_n C_m^* e^{-i\omega_{nm} t} \int d\underline{x}_2 \cdot \{\Phi_n(\underline{x}_1, \underline{x}_2) \cdot \Phi_m^*(\underline{x}_{1'}, \underline{x}_2)\} \quad . \quad (4.21)$$

Expressing this density matrix in the basis of HF orbitals leads to a complicated oscillatory behavior of properties such as S or Ω .

The oscillations in the SEE lead to another characteristic time. If the oscillations are Fourier transformed, the frequency with the largest signal, ω_c , is used to calculate a main oscillation period T according to

$$T = \frac{2\pi}{\omega_c} \quad . \quad (4.22)$$

In a model with only two populated states coupled to each other, as in the H_2 minimal basis model, the initial rise time t_{ir} and the oscillation time T are connected such that the oscillation time is approximately twice the initial rise time:

$$T = 2t_{ir} \quad . \quad (4.23)$$

For more complicated systems, this is usually not fulfilled, which is why we work with two characteristic times t_{ir} and T in what follows. The oscillation time is often dominated by the CISD ground state and a single excited state with a high population, *i.e.*, large coefficient C_n in equation (4.18). Within the initial rise time, however, a part of an oscillation is described in order to reach a first maximum on an ultrashort timescale. The initial rise time is thus often shorter than half of the oscillation time.

4.2 Correlation and entropy: Control

4.2.1 Creation of a Hartree-Fock state in CISD space

In this section, it is attempted to create a Hartree-Fock ground state, *i.e.*, the lowest state in energy with $S = 0 \text{ k}_\text{B}$, from the CISD correlated ground state Φ_0 . That is, we ask ourselves if it is possible to create an uncorrelated state by optical means, which otherwise is only a theoretical construct. For this purpose, first the Hartree-Fock ground state is represented by a superposition of CISD eigenstates as in equation (4.18). This representation is then used as a target wavefunction to excite the HF state photophysically using different laser pulse optimization algorithms. Since the Hartree-Fock ground state has an initial single electron entropy of 0, the creation of the RHF ground state is also a first example for controlling the single electron entropy using laser pulses.

4.2.1.1 Representation of the Hartree-Fock ground state in CISD space

We first express the Hartree-Fock ground state in the space of CISD eigenstates. For this purpose, one has to do a CISD calculation based on a RHF calculation. The first row of the coefficient matrix $\underline{\underline{D}}$ (consisting of all coefficient vectors \underline{D}_i according to equation (2.27)) contains the coefficients of all states contributing to

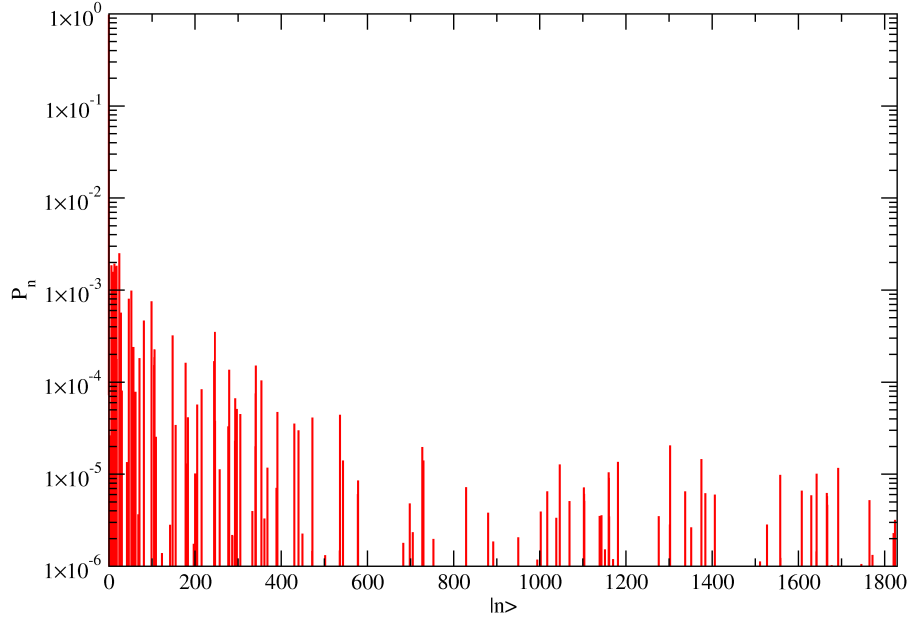


Figure 4.5: Shown are the populations P_n of all CISD states $|\Phi_0^{CISD}\rangle = |n\rangle$ contributing to the Hartree-Fock ground state.

the Hartree-Fock ground state:

$$\Phi_n^{CISD} = \sum_{\alpha=0}^{n_{st}-1} (\underline{D})_{\alpha,n} |\alpha\rangle \quad , \quad (4.24)$$

with Φ_n^{CISD} being the n -th CISD state, and $|\alpha\rangle$ stands for a determinant contributing to the total CISD wavefunction. This state can be projected on the Hartree-Fock ground state determinant $|0\rangle$:

$$\langle 0 | \Phi_n^{CISD} \rangle = \sum_{\alpha=0}^{n_{st}-1} (\underline{D})_{\alpha,n} \langle 0 | \alpha \rangle = (\underline{D})_{0,n} = D_{0,n} \quad . \quad (4.25)$$

From these coefficients, it follows that

$$|0\rangle = |\Psi_0^{HF}\rangle = \sum_n D_{0,n} |\Phi_n^{CISD}\rangle \quad , \quad (4.26)$$

which is analogous to equation (4.18), but specialized to CISD, *i.e.*, $C_n = D_{0,n}$ and $\Phi_n = \Phi_n^{CISD}$. The populations in all CISD states are obtained as $P_n = |D_{0,n}|^2$.

As an example, this is done for a hydrogen molecule (H_2 , aligned along z , $R_{HH} = 0.74 a_0$ (1.40 \AA)) using Dunning's cc-pVQZ basis set [100]. There, one obtains 1830 CISD states out of 1 occupied and 59 virtual MOs. The populations of a superposition of CISD states forming the Hartree-Fock ground state are shown in Fig. 4.5. From this figure, one can see, that the major portion is in the CISD

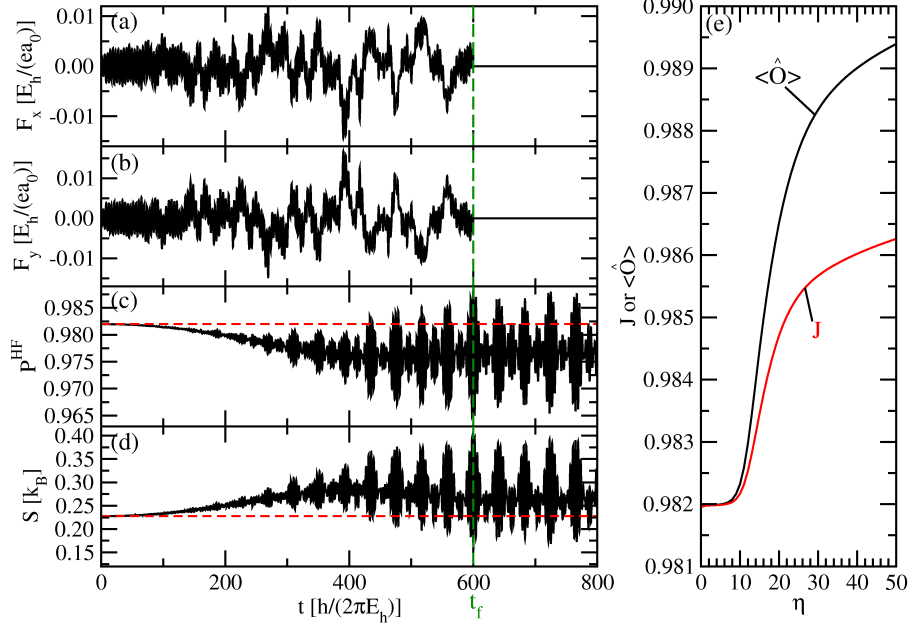


Figure 4.6: Shown are in the two upper panels the electric field polarized along x (F_x , panel (a)) and y (F_y , panel (b)). In panel (c), the time-dependent population of the Hartree-Fock ground state P^{HF} is shown. In panel (d), the resulting SEE S is plotted. This data was obtained for the hydrogen molecule oriented parallel to the z -axis at the TD-CISD level of theory using Dunning's cc-pVQZ basis set. Additionally, the end of the laser pulse t_f is indicated by the vertical green dashed line, and the horizontal red dashed lines indicate the values for the CISD ground state. In panel (e), the evolution of the target operator value $\langle \hat{O} \rangle$ and the total objective functional J is shown after η OCT iterations, after the control time t_f .

ground state (about 0.982). The other states with a relatively high population are the twenty-fourth (population $P_{24} \approx 2.5 \times 10^{-3}$) and the thirteenth excited state ($P_{13} \approx 1.9 \times 10^{-3}$). Other states with a low excitation energy are unpopulated, such as the first ($P_1 = 0$) or the second excited state ($P_2 \approx 2.6 \times 10^{-5}$).

This superposition can be used as the target wavefunction in a pulse optimization process according to the optimal control theory.

4.2.1.2 Optimal control theory

In this section, it is attempted to find a suitable laser pulse in order to excite the previously characterized Hartree-Fock ground state. For this purpose, this state is used as the target state in an OCT calculation, *i.e.*, $\hat{O} = |\Psi_0^{HF}\rangle\langle\Psi_0^{HF}|$ in equation

(2.93). From group theory (the point group of H_2 is $D_{\infty h}$), it is known that both the Hartree-Fock ground state and the CISD ground state have Σ_g^+ symmetry. As x and y have Π_u symmetry, and z has Σ_u^+ symmetry, it can be easily seen, that none of the elements of the direct product $\Psi_0^{HF} \otimes x$ (or y or z) $\otimes \Phi_0^{CISD}$ spans the totally symmetric representation of the point group, *i.e.*, the Hartree-Fock ground state cannot be populated from the CISD ground state using a single linearly polarized laser pulse. Thus, the initial pulse polarized along x and y is randomly created using the parameters (see equation (2.95)): $t_m = 300 \frac{\hbar}{E_h}$ (7.3 fs), $\Delta t_s = 600 \frac{\hbar}{E_h}$ (14.5 fs), $N_s = 12$, $\hbar\omega_{min} = 0.001 E_h$ (0.027 eV), $\hbar\omega_{max} = 1.04 E_h$ (28.3 eV), $f_{max} = 3 \times 10^{-4} \frac{E_h}{ea_0}$ ($154 \frac{MV}{m}$). This field is propagated using 60000 time steps of $\Delta t = 0.01 \frac{\hbar}{E_h}$ (0.24 as), *i.e.*, for a control time of $t_f = 600 \frac{\hbar}{E_h}$ (14.5 fs). After 50 iterations with a penalty factor $\alpha = 0.15$ (see equation (2.94)), an optimized field is obtained, which is shown in Figs. 4.6 (a) and (b). The initial wavefunction (the CISD ground state Φ_0^{CISD}) is propagated using the optimized field for 80000 time steps. In panel (c) of Fig. 4.6, the target state population $P^{HF}(t)$

$$P^{HF}(t) = |\langle \Psi_0^{HF} | \Psi(t) \rangle|^2 \quad (4.27)$$

is plotted. The resulting SEE is shown in panel (d) and the convergence of the total objective functional J and the target operator value $\langle \hat{O} \rangle$ (both of equation (2.92)) is plotted in panel (e). (Note, that full convergence is not achieved according to Fig. 4.6 (e).)

From Fig. 4.6 (e) it is noted that after a control time t_f , the target state (HF) population has increased from the initial value of 0.982, to about 0.989 after 50 iterations. From Fig. 4.6 (d), one can further anticipate that this moderate increase of P^{HF} , is accompanied by a local minimum of the SEE; we find $S(t_f) = 0.153 k_B$, starting from $S_0^{CISD} = 0.228 k_B$ for the correlated ground state. However, from this figure, one can also see that the SEE is not permanently lower than the one of the CISD ground state, but oscillates in a range of $S \in [0.153; 0.396] k_B$. Hence, the SEE is only temporarily lower than the SEE of the CISD ground state, at the control time t_f , and oscillates on ultrashort timescales afterwards. Averaged over the time in the $t > t_f$ regime, the single electron entropy even increases to $S_{av} = 0.271 k_B$. After t_f , also the target state population oscillates, in a range of $P^{HF} \in [0.965; 0.989]$. Optimal control theory is thus a method that is capable of decreasing the entropy at a certain time, but not permanently. In the next section, we try to decrease the single electron entropy directly using a stochastic pulse optimization algorithm and

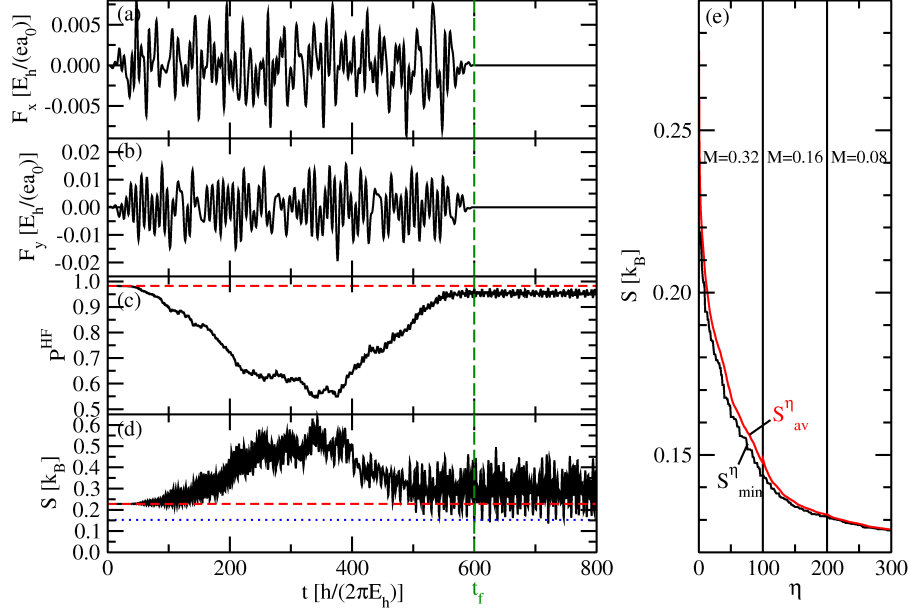


Figure 4.7: Shown is in the panels (a) and (b) the electric field polarized along x (F_x) and y (F_y). In panel (c), the time-evolution of the RHF ground state population P^{HF} is plotted. The curve in panel (d) represents the resulting SEE S . This data is obtained for the H_2 molecule oriented along z in a SPO algorithm using the TD-CISD level of theory and Dunning’s cc-pVQZ basis. The red dashed lines in the panels (c) and (d) indicate the initial value obtained for the CISD ground state, the blue dotted line in panel (d) is the minimal value obtained for OCT in Sec. 4.6. The vertical green dashed line indicates the end of the pulse t_f . In panel (e), the convergence of the minimal entropy S_{min}^η (at the control time) and the average entropy S_{av}^η (also at the control time) for each generation η are shown. The vertical lines indicate the regions where different mutation rates M are used.

not indirectly by increasing the population of the Hartree Fock ground state.

4.2.1.3 Stochastic pulse optimization

Using the stochastic pulse optimization (SPO) algorithm, no defined target state is needed. Instead, the SEE at the end of the pulse serves as the “fitness value” which should be lowered iteratively.

A set of 100 randomly generated pulses polarized along x and y with the parameters (according to equations (2.99)-(2.104)) $\hbar\omega = 0.010 E_h$ (0.285 eV), $f = 99$, $t_{max} = 600 \frac{\hbar}{E_h}$ (14.51 fs), $t_{rf} = 50 \frac{\hbar}{E_h}$ (1.2 fs) is used for an initial propagation and sorted by the lowest SEE at the end of the pulse. A “child generation” is formed by

modifying the old pulses in the described algorithm (initial mutation rate $M = 0.32$). Further propagations are made using the new pulses, sorting them by the SEE, and taking only the 100 laser fields with the lowest SEE for the new “parent generation”. After 100 “generations”, the SEE has decreased to $S_{min}^{SPO}(M = 0.32) = 0.144 \text{ k}_B$. The entropy oscillates after the end of the control pulse at $t = t_f$, with an average of $S_{av}^{SPO}(M = 0.32) = 0.281 \text{ k}_B$. A further optimization is performed using a mutation rate of $M = 0.16$. This lowers the SEE again to $S_{min}^{SPO}(M = 0.16) = 0.132 \text{ k}_B$ and an average of $S_{av}^{SPO}(M = 0.16) = 0.297 \text{ k}_B$. The results of a last optimization process using a mutation rate of $M = 0.08$ are shown in Fig. 4.7. A propagation with the optimized field given in the panels (a) and (b) of Fig. 4.7 results in an oscillating population in the Hartree-Fock ground state (shown in panel (c) of Fig. 4.7) within the interval $P^{HF}(t > t_f) \in [0.934; 0.972]$ and an average population of $P_{av}^{HF} = 0.953$. This population never exceeds the Hartree-Fock state population for the CISD ground state ($P_{CISD}^{HF} = 0.982$, shown as the red dashed line in panel (c)). The resulting SEE (shown in panel (d) of Fig. 4.7), however, oscillates within an interval $S^{SPO}(t > t_f) \in [0.127; 0.495] k_B$ with an average of $S_{av}^{SPO}(t > t_f) = 0.300 \text{ k}_B$ and goes thus temporarily below the entropy value for the CISD ground state ($S^{CISD} = 0.228 \text{ k}_B$, indicated by the red dashed line) and the minimal value obtained using optimal control theory ($S_{min}^{OCT} = 0.181 \text{ k}_B$, indicated by the blue dotted line). As the oscillations of the SEE are still very fast, further investigations were carried out in order to obtain a low SEE with a longer “preservation time” (in Sec. 4.2.2).

4.2.2 Low SEEs with longer characteristic times

As one could see in the previous section, a low SEE (obtained photophysically or by propagating the Hartree-Fock ground state) is increasing to a maximal SEE within an ultrashort time of about $2.5 \frac{\hbar}{E_h}$ (60 as). In this section, it is first proved that this time can be extended if either high-energetic states (Sec. 4.2.2.1) or low-populated states (Sec. 4.2.2.2) are cut off. After the cutoff procedure, the Hartree-Fock ground state is no longer exactly represented by a linear combination of CISD states. The renormalized wavefunction is then propagated without a laser field and the resulting single electron entropy is calculated. An appropriate wavefunction is later used as a target function within an OCT calculation (Sec. 4.2.2.3).

Two characteristic time measures are considered: on the one hand, the initial

rise time t_{ir} as the delay time to the first maximum of the SEE, and on the other hand, the main oscillation time T according to equation (4.22).

4.2.2.1 Neglect of high-energy eigenstates: Energy-cutoff criterion

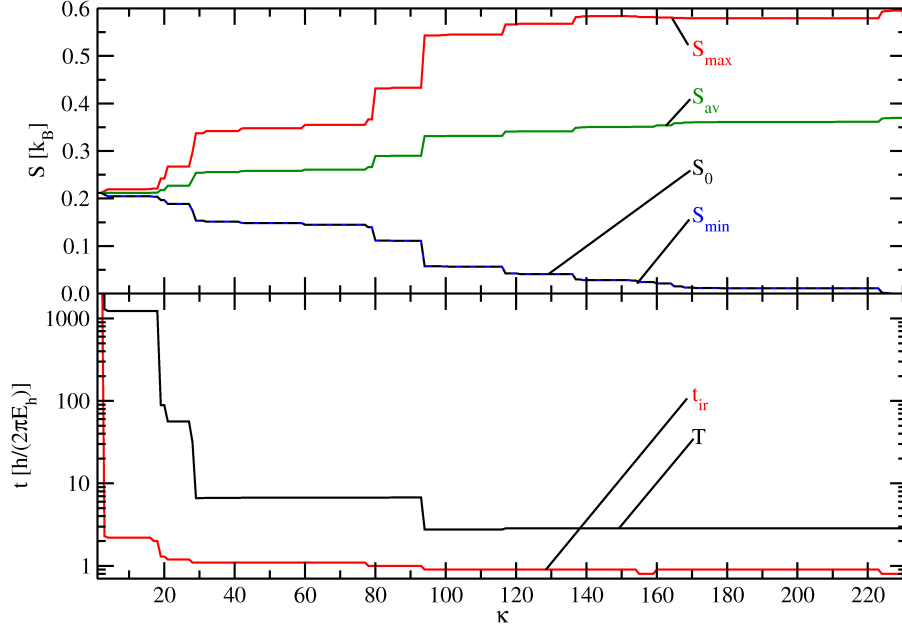


Figure 4.8: Shown are in the upper panel the maximal SEEs (S_{max} , red line), the minimal SEEs (S_{min} , blue line), the SEEs at the beginning of each propagation (S_0 , dashed black line), and the average SEEs (S_{av} , green line) if only populations in the lowest κ CISC eigenstates of the Hartree-Fock ground state (in CISC state representation) are taken into account within the helium dimer using the 6-31G** basis set. In the lower panel the main oscillation periods T (determined by Fourier transformation) and the initial rise times t_{ir} of these entropies are shown. For $\kappa = 1$ and $\kappa = 2$, there are no oscillations, so the oscillation period and the initial rise time are infinitely large.

In a first investigation, the Hartree-Fock ground state wavefunction in the space of CISC eigenstates was modified in the way that coefficients in high-energy states are neglected. The resulting wavefunction is renormalized and propagated without laser field, and the resulting SEE is calculated. First, the number of states taken into account is varied in order to check the appropriateness as a wavefunction with a low SEE and a long oscillation period of the entropy.

As a first model, the helium dimer (oriented along z , interatomic distance

$R_{HeHe} = 2.74 a_0$ (1.45 \AA) is used. A CISD calculation with the 6-311G** basis set [95] results in 231 states out of 2 occupied and 10 virtual MOs. The Hartree-Fock ground state can then be represented as a superposition of all these CISD eigenstates. Next, different “cut off” and renormalized wavefunctions are created and propagated in time (the propagation ends at $t_{end} = 200 \frac{\hbar}{E_h}$ (4.8 fs)). To this end, one takes only the populations within the κ lowest eigenstates into account (with $\kappa \in [1; 231]$). For $\kappa = 1$, the CISD ground state is obtained whose SEE is greater than 0 but constant. For $\kappa = 231$, the Hartree-Fock ground state is the initial wavefunction. Its SEE is (by definition) 0 at the beginning but increases on an ultrafast timescale. For intermediate values of κ , there might be wavefunctions for which the resulting SEE has a long oscillation period and a long initial rise time, and a value between the initial entropy level of the HF ground state and the constant level for the CISD ground state. It is a challenge to find a state that has a low SEE (lower than the CISD ground state) with a high initial rise time and a high oscillation period. In a second step, such a state may be excited photophysically.

The parameters of the SEEs for these “approximate” HF wavefunctions are shown in Fig. 4.8. In the upper panel, one can see the minimal entropy S_{min} , the maximal entropy S_{max} , the average entropy S_{av} , and the initial entropy S_0 (equal to S_{min}) for every approximate wavefunction with κ states. In the lower panel, the two characteristic times t_{ir} and T are shown. On a first view, one can also see that the oscillation time does not change significantly if the populations of the highest 137 states are set to zero (from $\kappa = 231$ to $\kappa = 94$). This is also valid for the initial rise times t_{ir} that has even lower values. These “truncated HF wavefunctions” have still the same behavior concerning the stability of their low single electron entropy. At the same time, the SEE interval changes slightly from $[S_{min}, S_{max}] = [0.000; 0.595] k_B$ to $[S_{min}, S_{max}] = [0.058; 0.543] k_B$. But it is hard to populate a wavefunction with contributions of at least 94 eigenstates – even for the case that some of these states are numerically unpopulated – using laser pulses. Also, the “lifetime” should be longer than about $2.9 \frac{\hbar}{E_h}$ (69.2 as). Longer oscillation periods are achieved if only the populations in the lowest 21 states are taken into account, but then the SEE interval becomes much smaller ($[0.189; 0.267] k_B$, $T = 56.5 \frac{\hbar}{E_h}$ (1.36 fs), $t_{ir} = 1.2 \frac{\hbar}{E_h}$ (29.0 as)). Also, it can be seen, that the SEE interval, the oscillation periods, and the initial rise times do not change significantly when κ is changed in rather large intervals (like for $\kappa \in [94; 231]$ or $\kappa \in [29; 93]$, or even for low energy states like

$\kappa \in [4; 18]$). This means that many states are not important with respect to the SEE, even within the low-energy state manifold. Therefore, one might obtain a low-entropy target wavefunction for an OCT excitation consisting of only a few CISD eigenstates, if not an energy-cutoff criterion is applied, but a population cutoff criterion instead. This is done in the next section (Sec. 4.2.2.2).

4.2.2.2 Neglect of lowly populated eigenstates: Population-cutoff criterion

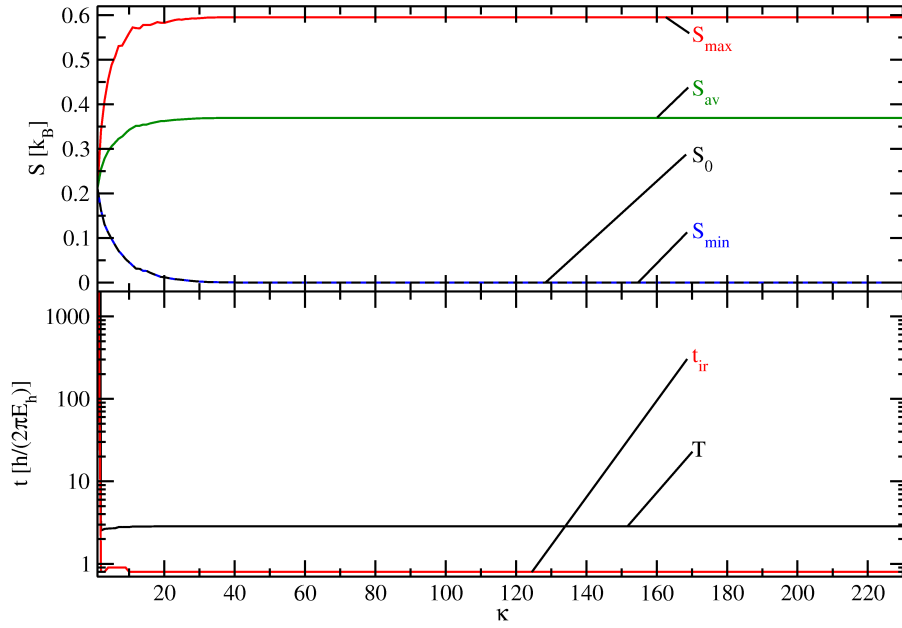


Figure 4.9: Shown are in the upper panel the maximal SEEs (S_{max} , red line), the minimal SEEs (S_{min} , blue line), the SEEs at the beginning of each propagation (S_0 , black dashed line), and the average SEEs (S_{av} , green line) if only populations in the κ CISD eigenstates with the highest population of the Hartree-Fock ground state (in CISD state representation) are taken into account within the helium dimer using the 6-31G** basis set. In the lower panel the initial rise times t_{ir} and the main oscillation periods T of these SEEs are shown. For $\kappa = 1$, there are no oscillations, so the oscillation period is infinitely large.

If the populations of the CISD eigenstates for the Hartree-Fock ground state are sorted according to their absolute value and the CI coefficients for the lowly populated states are set to zero, one obtains another type of “approximate wavefunction”, for which only κ states are taken into account. After renormalization,

this wavefunction can also be used in order to calculate a low SEE with a longer oscillation period. The resulting parameters (maximal SEE S_{max} , minimal SEE S_{min} and average SEE S_{av}) are shown in Fig. 4.9 together with the oscillation period T and the initial rise time t_{ir} for various values of κ . In Fig. 4.9, one can see that the oscillation period is small ($T \approx 2.8 \frac{\hbar}{E_h}$ (68 as)) for any value of κ (except for $\kappa = 1$). The same behavior is observed for the initial rise time, that is even shorter ($t_{ir} = 0.8 \frac{\hbar}{E_h}$ (19 as)). The SEE range $[S_{min}, S_{max}]$ does not change for $\kappa > 40$. For lower numbers of states taken into account, the SEE range becomes smaller exponentially. The initial SEE value, that is usually equal to the minimal value, does not change either for $\kappa > 40$, but increases dramatically for lower values. Hence, these “approximate HF wavefunctions” do not lead to long oscillation periods, long initial rise times, and low SEEs.

The oscillation period and the initial rise time seem to correlate with the population of the respective CISD states. All oscillations of the SEE arising from a coupling between the ground state to any populated higher state have a higher amplitude. Other higher populated states are the ninety-third state ($P_{93} = 3.6 \times 10^{-3}$) with an excitation energy of $E_{93} = 3.88 E_h$ and the seventy-ninth excited state ($P_{79} = 2.0 \times 10^{-3}$, with $E_{79} = 3.73 E_h$). For oscillations with a lower frequency, we need at least two higher populated states with a low energy difference. To this end, the CISD ground state cannot be used, as the excitation energy to the first excited state $E_1 = 1.36 E_h$ is very high.

As these “truncated HF wavefunctions” do not seem to be appropriate in order to excite a Hartree-Fock-like state with a low SEE and a long oscillation period, another molecule is tested. The methane molecule using the 6-31G* [95] basis set is the new test system (one C-H bond along z , $R_{CH} = 2.04 a_0$ (1.08 Å), $\theta_{HCH} = 109.46^\circ$, $\phi_{HCHH} = 120.0^\circ$). For this molecule, only the “partial wavefunctions” using the states with the highest populations are employed (population-cutoff criterion). First, these wavefunctions are propagated in time without the use of a laser field. Some of the resulting SEEs are shown in Fig. 4.10. There, it is clearly shown that all “truncated HF wavefunctions” lead to entropies that are temporarily below the constant level for the CISD ground state ($\kappa = 1$). It is also seen, that the time evolution of the “approximate HF wavefunctions becomes more complicated, if more CISD states are involved. For $\kappa = 1$, there are no oscillations; for $\kappa = 2$, one oscillation is obtained, with $T = 2t_{ir}$ (green line in Fig. 4.10). For even higher

values $\kappa \geq 3$, more oscillations are obtained, the initial rise time is no more a simple function of the main oscillation time. One of these “approximate HF wavefunctions” is now used as the target function in an OCT calculation.

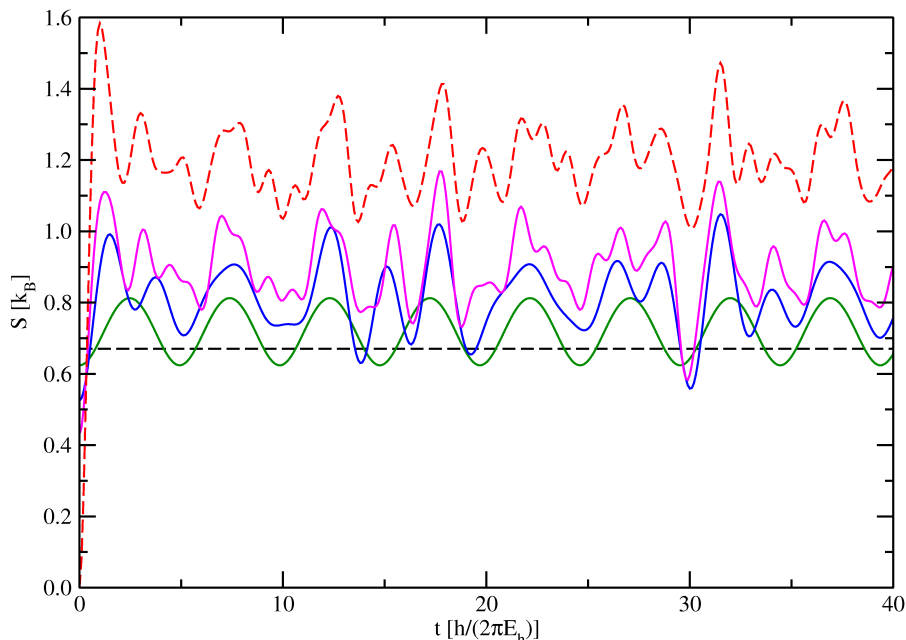


Figure 4.10: Shown are the resulting SEEs when different “truncated HF wavefunctions” within the methane molecule using the 6-31G* basis set are propagated in time. The black dashed line indicates the pure CISD ground state ($\kappa = 1$), the green line a wavefunction with two states taken into account ($\kappa = 2$). The blue curve is for $\kappa = 5$, the magenta curve indicates the SEE for $\kappa = 10$. Finally, the red dashed line stands for the exact Hartree-Fock ground state ($\kappa = 2701$).

4.2.2.3 OCT excitation of “approximate HF wavefunctions”

In this section, it is attempted, for CH_4 , to excite a previously defined renormalized “approximate HF wavefunction” including only those CISD states with the highest population using laser pulses generated by optimal control theory. For this purpose, a wavefunction using the 10 most populated eigenstates of the Hartree-Fock ground state in CISD representation (corresponding to the magenta curve in Fig. 4.10) is the target function. The initial pulse is randomly chosen with energies in the range $\hbar\omega = [0.001; 5.500] E_h$ ($[0.027; 149.663] \text{ eV}$). The electric field has components along all Cartesian coordinates. The shape function of equation (2.95) has the parameters: $t_m = 125 \frac{\hbar}{E_h}$ (3.02 fs), $\Delta t_s = 220 \frac{\hbar}{E_h}$ (5.32 fs), $N_s = 12$. After 20 iterations using

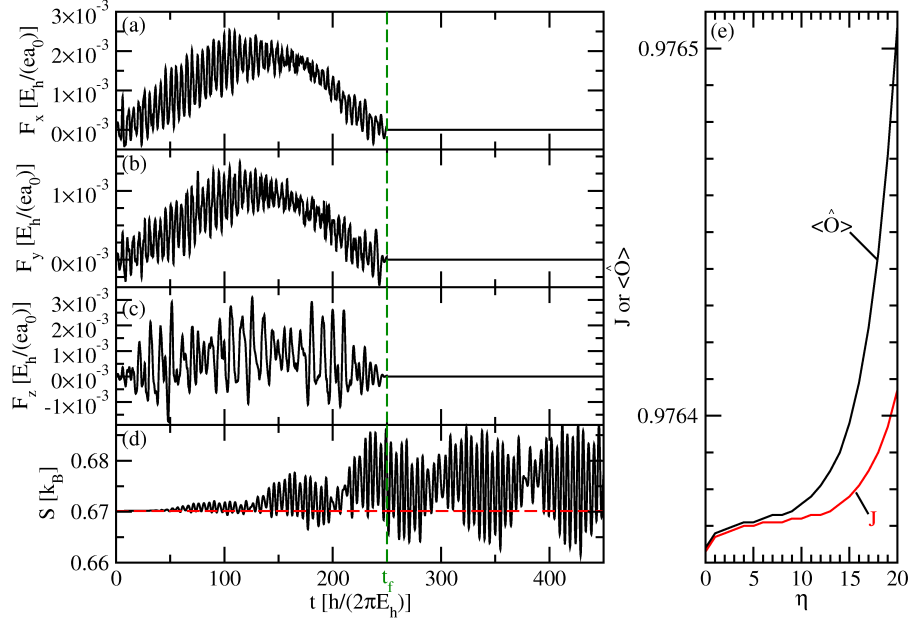


Figure 4.11: Shown are in the panels (a), (b), and (c) the x -, y -, and z -components of the electric field (F_x , F_y , and F_z) for an excitation from the CISD ground state to a Hartree-Fock-like target wave function, again for methane. This field is obtained as the result of an pulse optimization process within the optimal control theory (for details see text). In panel (d), the time-evolution of the SEE of the system is shown (black solid line). The red dashed line represents the constant entropy level of the CISD ground state. The vertical green dashed line in the panels (a) to (d) indicates the end of the pulse t_f . In panel (e), the values for the target operator value $\langle \hat{O} \rangle$ and the total objective functional J are plotted for each OCT iteration (with η as the number of iterations).

a penalty factor of $\alpha = 0.12$, an OCT field is obtained. This field is shown in the upper three panels of Fig. 4.11 (panel (a): x -component, panel (b): y -component, and panel (c): z -component).

As one can see, the electric field has a low intensity. None of the three components increases to more than $0.003 \frac{E_h}{ea_0}$ ($1.54 \frac{GV}{m}$). In the resulting SEE (panel (d) of Fig. 4.11), it is shown that the oscillating SEE is – averaged over the time – $S_{av} = 0.6753 k_B$ and thus above the reference entropy for the CISD ground state of $S_{CISD} = 0.6701 k_B$. It can be, however, temporarily below this SEE ($S_{min} = 0.6615 k_B$). This is reached although convergence in the target operator value $\langle \hat{O} \rangle$ and in the total objective functional J is not yet achieved after 20 OCT iterations. The calculation is truncated after this number of iterations only to see

if there is an improvement after such an optimization process. A real Hartree-Fock ground state-like state is nevertheless not obtained.

In this section, it was shown that one can obtain a SEE that is below the value for the CISD ground state temporarily. The oscillation period is very short for all of the different tested target wavefunctions, so it seems not to be possible to decrease the SEE permanently or at least with a long “lifetime”.

However, there may be other systems, for which the SEE does not increase on an ultrashort timescale. If a molecule has different stable and quasi-degenerate configurations, *i.e.*, static correlation, this may lead to a low SEE with a high “initial rise time” and a high oscillation period. Such a state can be accessed using optimal pulses created by OCT or another pulse optimization scheme. Furthermore, one could use long laser pulses in order to conserve a low SEE value over long time periods.

Chapter 5

Conclusions and Outlook

This thesis has shown how time-dependent correlated methods based on wavefunctions can be used to describe laser-induced processes in molecular systems. Further, they are capable of explaining these processes, and finally, they help to find predictions for laser experiments.

In the first part, a heuristic ionization model within the time-dependent configuration interaction singles method was presented. This model is used to describe an ionization continuum in the framework of atom-centered atomic orbital-type basis sets. This ionization continuum is formed by broadening discrete states by a ionization rate leading to an exponential decay of the population of this state. Three algorithms to calculate these ionization rates were presented.

The third model was chosen the best of the three models. Within this algorithm the ionization rates for all states below Koopmans' first ionization potential are set to zero leading to a set of non-ionizing excited states. The states above the ionization potential are assigned a finite lifetime according to their composition of one electron excitations within the molecular orbital picture. Thus, a non-monotonic increase of the ionization rate is guaranteed which seems to be reasonable. The density of states confirmed that an ionization continuum is formed above the ionization potential. Some states that are dominated by low lying valence electron excitations appear as resonances in this picture.

For all of the introduced algorithms, an empirical escape length d was introduced, after which the electron was considered as ionized. Here, d was adjusted once for a pulse sequence and once for different initial non-ionizing states in that manner, that the loss of norm and thus the ionization probability is as high as possible in order to

study a “worst case scenario”. Further, it was set to a constant value, independent of the initial state and independent of the pulse parameters like frequency or intensity. It is a challenge for future work to find an appropriate way to determine the values for the escape length for specific systems and various initial and/or final states.

Within the model, it has been demonstrated that excitations between states below the ionization potential according to Koopmans’ theorem using π -pulses are still leading to an almost complete population inversion, if the pulse has a sufficiently low intensity. For higher intensities, multi-photon excitations are promoted, and the ionization probability would increase. Here, for LiCN even for a pulse sequence consisting of four π -pulses, the loss of norm was lower than 0.13. Also excitations to ionizing, resonance-like states were simulated. Then, one can obtain a temporary population in this state that is above 0.10 for LiCN. This population, however, decays on the timescale dictated by the resonance width.

It was shown for two different systems, *e.g.* LiCN and benzo-[g]-*N*-methylquinolinium-7-hydroxylate, that one can generate electronic wavepackets below the ionization potential and probe the wavepacket motion with a second pulse, that is delayed in time, creating an ionization signal. If the delay time between the pulses is varied, one obtains a pump-probe spectrum where the loss of norm is the probe signal. For both systems (lithium cyanide molecule and benzo[g]-*N*-methylquinolinium-7-hydroxylate molecule), it has been shown that the time-dependence of the probe signal resembles the time-dependent dipole moment of the original wavepacket (the wavepacket that is generated if only the pump pulse is applied to the system). For the larger molecule, it was also shown that the loss of norm depends strongly on the frequency of the probe pulse, the initial state, the transition dipole moments, and – as already mentioned – the escape length parameter. The intensity of the probe pulse was then optimized in the way that the loss of norm is low enough to neglect the formation of multiply charged ions and the ionization of pre-ionized matter. As these effects are not yet included in the model, it is a project for the future to describe also these phenomena theoretically within a similar approach.

What was also determined using time-dependent configuration interaction singles including photoionization are the effects on frequency-dependent polarizabilities. For an intense pulse with variable frequency it was investigated, if and how the dynamic polarizability changes when photoionization is included. The polarizability has (for TD-CIS) without photoionization a characteristic behavior: At every tran-

sition frequency to a higher state there is a pole-like structure (a damped pole), if this state is optically accessible. When our heuristic ionization model is applied, nothing changes for all transitions below the ionization potential. For higher transitions in the continuum, the polarizability has no pole any more but the curve is damped (depending on the value of d). In an extreme case, the curve can even be horizontal. Since poles of the polarizability in a broad continuum are artificial, the TD-CI method with ionization gives a more realistic description of the system. Here, also the SOS-formula was extended to ionization as another algorithm to calculate frequency-dependent polarizabilities. It has no significant deviation with respect to the frequency-dependent polarizability calculated with TD-CIS including photoionization if transition frequencies above the ionization potential are investigated, for lower frequencies, however, true poles at the transition frequencies appear due to the perturbative wave nature of SOS.

The model presented here was also combined with another model based on the propagation of density matrices in order to describe the effects of both dissipation and photoionization. The effects are treated independently as competing processes. The density-matrix based method was tested for state-to-state excitations of the H_2 molecule using π -pulses. There, it was seen, that – despite of the treatment – the individual processes are influencing each other. The inclusion of dissipation reduces slightly the population losses due to photoionization. Furthermore, photoionization increases the selectivity of laser pulses, even in a dissipative environment.

For all these results, it should be mentioned that they were obtained in the clamped nuclei approximation. This approximation may be invalid during longer pulse sequences and propagations, especially for light atoms. A rearrangement of nuclei would change the excitation energies, the dipole moments and transition dipole moments, and even ionization rates. For the lithium cyanide molecule and the hydrogen molecule, the application of the fixed nuclei approximation is probably invalid, *i.e.*, a rearrangement of nuclei cannot be neglected. For the BMQ7H molecule, the validity of the fixed nuclei approximation is more likely, at least for the two states with the major contributions to the electronic wavepacket, which was investigated in this thesis. The inclusion of important nuclear modes is also a promising project for future work.

A second focus of this thesis was on the time-dependent single electron entropy (SEE) of a molecular system and its control using laser pulses. For this purpose,

the SEE is calculated from a one electron reduced density matrix, as the entropy calculated from a N electron density matrix would always be zero, for a pure state. Two time-dependent correlated wavefunction-based methods (MCTDHF and TD-CISD) were tested.

An investigation was aiming at the time-dependent SEE calculated from the MCTDHF and the TD-CISD wavefunctions. For this purpose, the Hartree-Fock ground state of the hydrogen molecule was propagated in real time, and the entropy was calculated. It was shown, that MCTDHF and TD-CISD lead to the same SEEs in the Full-CI limit. The second measure for time-dependent correlation using the quantum impurity (QI) results in the same qualitative behavior. For further investigations regarding the SEE and its control, the TD-CISD method was used. It was shown that the initial Hartree-Fock ground state has a SEE of 0 that increases in an ultrafast process and oscillates. This lead to two different investigations: On the one hand, laser pulses were optimized to minimize the SEE at least temporarily; on the other hand, different “approximate HF wavefunctions” (renormalized Hartree-Fock ground state wavefunctions truncated in CISD eigenstate representation), were tested in order to obtain a wavefunction with a low SEE and a higher “initial rise time” and main oscillation period. This “approximate HF wavefunction” was used as a target state in a pulse optimization scheme.

For the first part, it was shown that an OCT optimized laser pulse with the Hartree-Fock ground state as the target state leads to a temporarily lower SEE arising from a temporarily higher Hartree-Fock ground state population. But the average SEE even increases, and the initial rise time and the main oscillation period are still ultrashort. This OCT result was improved by using the stochastic pulse optimization as another laser pulse optimization scheme. For this algorithm, a lower entropy was obtained, however, also with ultrashort characteristic times. In this case, however, the Hartree-Fock ground state population decreases.

In the second part, two general approaches for “approximate HF wavefunctions” were tested. First, one can neglect populations in high-energy CISD states. The SEE range becomes smaller, but the initial rise time does not increase significantly. The other approach is the neglect of populations in states with a low population or states that are numerically unpopulated. This approach does not lead to higher initial rise times (but to lower SEE ranges). An optimization within the optimal control theory using an “approximate HF wavefunction” with the most populated

states as target state results a decreased SEE but still an ultrashort initial rise time. In future work, one could investigate other systems; furthermore, dissipation and ionization should be considered, and the low-entropy state may be conserved and stabilized by applying a continuous laser field.

To conclude, it has been shown that time-dependent correlated wavefunction-based methods describe phenomena that are related to the interaction between laser fields and matter properly and they can be extended that way that they include effects like photoionization or single electron entropies.

Appendix A

Functions of matrices

A.1 Functions of diagonal matrices

If a matrix is already diagonal, a function $f(\underline{\underline{A}})$ of this matrix (rank N) is given as a diagonal matrix containing the functions of the respective diagonal element:

$$f(\underline{\underline{A}}) = \begin{pmatrix} f(A_{11}) & 0 & \cdots & 0 \\ 0 & f(A_{22}) & \cdots & 0 \\ \vdots & \vdots & \ddots & \vdots \\ 0 & 0 & \cdots & f(A_{NN}) \end{pmatrix} . \quad (\text{A.1})$$

A.2 Functions of diagonalizable matrices

The function of a diagonalizable matrix is calculated as follows: First, the matrix $\underline{\underline{A}}$ is diagonalized by the matrix $\underline{\underline{U}}$ (and its adjoint $\underline{\underline{U}}^\dagger$) containing the eigenvectors \underline{a}_i of $\underline{\underline{A}}$. Then, the function is applied to all diagonal elements of the new matrix according to equation (A.1). The result is retransformed using the same matrices $\underline{\underline{U}}$ and $\underline{\underline{U}}^\dagger$. This is written as follows:

$$f(\underline{\underline{A}}) = \underline{\underline{U}} f(\underline{\underline{U}}^\dagger \underline{\underline{A}} \underline{\underline{U}}) \underline{\underline{U}}^\dagger . \quad (\text{A.2})$$

The function (here $e^{\underline{\underline{A}}}$ is developed as a Taylor series. One can always multiply with $\underline{\underline{U}} \underline{\underline{U}}^\dagger$, as this gives the identity matrix $\underline{\underline{1}}$.

$$\begin{aligned} e^{\underline{\underline{A}}} &= \underline{\underline{1}} + \underline{\underline{A}} + \frac{\underline{\underline{A}}^2}{2} + \dots \\ &= \underline{\underline{U}} \underline{\underline{U}}^\dagger \underline{\underline{1}} \underline{\underline{U}} \underline{\underline{U}}^\dagger + \underline{\underline{U}} \underline{\underline{U}}^\dagger \underline{\underline{A}} \underline{\underline{U}} \underline{\underline{U}}^\dagger + \frac{1}{2} \underline{\underline{U}} \underline{\underline{U}}^\dagger \underline{\underline{A}} \underline{\underline{U}} \underline{\underline{U}}^\dagger \underline{\underline{A}} \underline{\underline{U}} \underline{\underline{U}}^\dagger + \dots \\ &= \underline{\underline{U}} e^{\underline{\underline{U}}^\dagger \underline{\underline{A}} \underline{\underline{U}}} \underline{\underline{U}}^\dagger \end{aligned} \quad (\text{A.3})$$

For example, the natural logarithm of a matrix is calculated as

$$\ln(\underline{\underline{A}}) = \underline{\underline{U}}[\ln(\underline{\underline{U}}^\dagger \underline{\underline{A}} \underline{\underline{U}})]\underline{\underline{U}}^\dagger \quad , \quad (\text{A.4})$$

where

$$\ln(\underline{\underline{U}}^\dagger \underline{\underline{A}} \underline{\underline{U}}) = \begin{pmatrix} \ln(a_1) & 0 & \cdots & 0 \\ 0 & \ln(a_2) & \cdots & 0 \\ \vdots & \vdots & \ddots & \vdots \\ 0 & 0 & \cdots & \ln(a_N) \end{pmatrix} . \quad (\text{A.5})$$

Appendix B

Propagation in imaginary time

For time-dependent calculations, especially for MCTDHF, the ground state is often obtained by propagating an (arbitrary) initial state in imaginary time. This means, the usual propagation operator $e^{-i\hat{H}t/\hbar}$ is modified such, that the time step Δt is replaced by $-i\tau$. We thus obtain a wavefunction

$$\Psi(\tau) = C_0 e^{-E_0\tau} \psi_0 + C_1 e^{-E_1\tau} \psi_1 + \dots \quad , \quad (\text{B.1})$$

where C_i is the coefficient of the wavefunction ψ_i , and $\hat{H}\psi_i = E_i\psi_i$. In this equation, the wavefunctions ψ_n are sorted by ascending energies, *i.e.*, $E_0 < E_1 < E_2 \dots$. The consequence of this is, that $C_0 e^{-E_0\tau}$ becomes large for long propagation times with respect to all other time-dependent coefficients $C_n e^{-E_n\tau}$. For infinite values of τ , one obtains

$$\begin{aligned} \lim_{\tau \rightarrow \infty} \frac{C_0^2 e^{-2 \cdot E_0 \tau}}{\sum_m C_m^2 e^{-2 \cdot E_m \tau}} &= 1 \quad \text{and} \\ \lim_{\tau \rightarrow \infty} \frac{C_n^2 e^{-2 \cdot E_n \tau}}{\sum_m C_m^2 e^{-2 \cdot E_m \tau}} &= 0 \quad \text{for } n \neq m \quad . \end{aligned} \quad (\text{B.2})$$

This is also shown for a system with three states ψ_n and respective energies ($E_0 = 0.00 \text{ E}_h$, $E_1 = 0.20 \text{ E}_h$, $E_2 = 0.22 \text{ E}_h$) in Fig. B.1. At the beginning, all three states have the same population ($C_0^2 = C_1^2 = C_2^2 = \frac{1}{3}$). After a propagation time of $t = 30 \frac{\hbar}{\text{E}_h}$ (and renormalization of the wavefunction), practically all population is in the ground state ψ_0 , and the other states are depopulated.

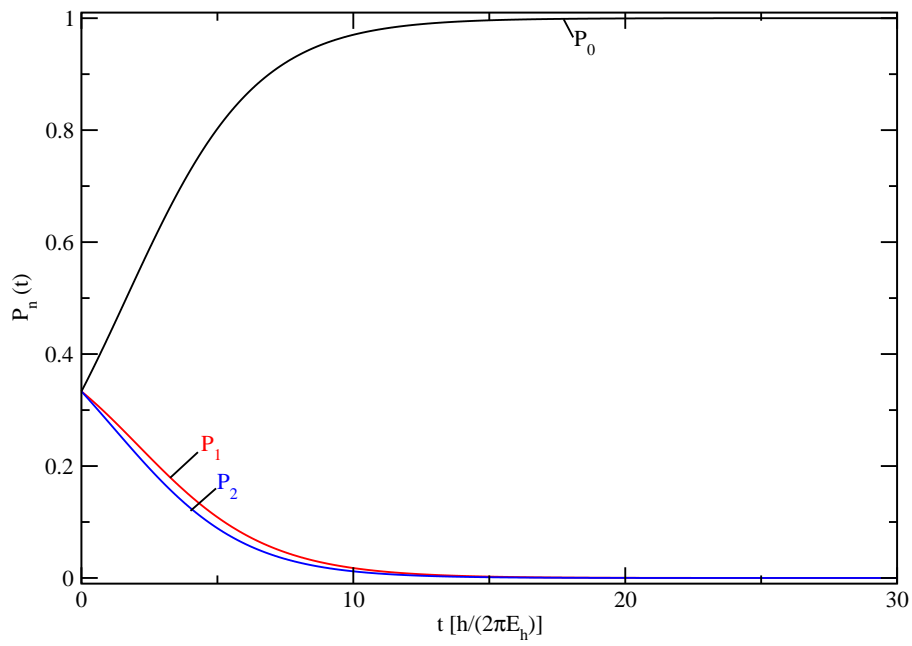


Figure B.1: Shown are the renormalized populations P_n for a model with three states at $E_0 = 0.00 E_h$, $E_1 = 0.20 E_h$, and $E_2 = 0.22 E_h$, when they are propagated in imaginary time. The initial populations are set to $P_0 = P_1 = P_2 = \frac{1}{3}$.

Bibliography

- [1] M. Dantus, M. J. Rosker, and A. H. Zewail, *J. Chem. Phys.* **87**, 2395 (1987).
- [2] T. S. Rose, M. J. Rosker, and A. H. Zewail, *J. Chem. Phys.* **88**, 6672 (1988).
- [3] M. Hentschel, R. Kienberger, C. Spielmann, G. A. Reider, M. Nenad, T. Brabec, P. B. Corkum, U. Heinzmann, M. Drescher, and F. Krausz, *Nature (London)* **414**, 509 (2001).
- [4] J. Itatani, J. Levesque, D. Zeidler, H. Niikura, H. Pépin, J.-C. Kieffer, P. B. Corkum, and D. M. Villeneuve, *Nature (London)* **432**, 867 (2004).
- [5] M. F. Kling, C. Siedschlag, A. J. Verhoef, J. I. Khan, M. Schultze, T. Uphues, Y. Ni, M. Uiberacker, M. Drescher, F. Krausz, and M. J. J. Vrakking, *Science* **312**, 246 (2006).
- [6] F. Krausz and M. Ivanov, *Rev. Mod. Phys.* **81**, 163 (2009).
- [7] D. R. Hartree, *Proc. Camb. Phil. Soc.* **24**, 89 (1928).
- [8] V. Fock, *Z. Physik* **61**, 126 (1930).
- [9] R. A. Ferrell, *Phys. Rev.* **107**, 1631 (1957).
- [10] E. Runge and E. K. U. Gross, *Phys. Rev. Lett.* **52**, 997 (1984).
- [11] P. Hohenberg and W. Kohn, *Phys. Rev. B* **136**, 864 (1964).
- [12] W. Kohn and L. J. Sham, *Phys. Rev. A* **140**, 1133 (1964).
- [13] E. Schrödinger, *Ann. Physik* **79**, 361 (1926).
- [14] E. Schrödinger, *Ann. Physik* **79**, 489 (1926).
- [15] E. Schrödinger, *Ann. Physik* **80**, 437 (1926).

- [16] E. Schrödinger, *Ann. Physik* **81**, 109 (1926).
- [17] J. Zanghellini, M. Kitzler, C. Fabian, T. Brabec, and A. Scrinzi, *Laser Phys.* **13**, 1064 (2003).
- [18] T. Kato and H. Kono, *Chem. Phys. Lett.* **392**, 533 (2004).
- [19] M. Nest, T. Klamroth, and P. Saalfrank, *J. Chem. Phys.* **122**, 124102 (2005).
- [20] D. Hegarty and M. A. Robb, *Mol. Phys.* **38**, 1795 (1979).
- [21] H.-D. Meyer, U. Manthe, and L. S. Cederbaum, *Chem. Phys. Lett.* **165**, 73 (1990).
- [22] T. Klamroth, *Phys. Rev. B* **68**, 245421 (2003).
- [23] C. Huber and T. Klamroth, *Appl. Phys. A* **81**, 91 (2004).
- [24] P. Saalfrank, T. Klamroth, C. Huber, and P. Krause, *Isr. J. Chem.* **45**, 205 (2005).
- [25] M. Awasthi, Y. V. Vanne, and A. Saenz, *J. Phys. B: At. Mol. Opt. Phys.* **38**, 3973 (2005).
- [26] N. Rohringer, A. Gordon, and R. Santra, *Phys. Rev. A* **74**, 043420 (2006).
- [27] H. B. Schlegel, S. M. Smith, and X. Li, *J. Chem. Phys.* **126**, 244110 (2007).
- [28] P. W. Atkins and R. S. Friedmann, *Molecular Quantum Mechanics* (Oxford University Press Inc., New York, 2005), 4th edition.
- [29] L. Greenman, P. J. Ho, S. Pabst, E. Kamarchik, D. A. Mazziotti, and R. Santra, *Phys. Rev. A* **82**, 023406 (2010).
- [30] P. Krause, T. Klamroth, and P. Saalfrank, *J. Chem. Phys.* **123**, 074105 (2005).
- [31] P. Krause, T. Klamroth, and P. Saalfrank, *J. Chem. Phys.* **127**, 034107 (2007).
- [32] P. Krause, *Many-electron Dynamics in Molecules by means of Time-dependent Configuration Interaction Methods*, Ph.D. thesis, University of Potsdam (2007).
- [33] S. Klinkusch, *Theorie des femtosekundenlaserinduzierten intermolekularen Elektronentransfers mittels zeitabhängiger Konfigurationswechselwirkungs-Methoden*, Diploma thesis, University of Potsdam (2008).

- [34] S. Klinkusch, T. Klamroth, and P. Saalfrank, *Phys. Chem. Chem. Phys.* **11**, 3875 (2009).
- [35] J. Breidbach and L. S. Cederbaum, *J. Chem. Phys.* **118**, 3983 (2003).
- [36] I. Barth and J. Manz, *Angew. Chem. Intern. Ed.* **45**, 2962 (2006).
- [37] M. Nest, *Chem. Phys. Lett.* **472**, 171 (2009).
- [38] S. Chelkowski, C. Foisy, and A. D. Bandrauk, *Phys. Rev. A* **57**, 1176 (1998).
- [39] M. V. Ammosov, N. B. Delone, and V. P. Krainov, *Zh. Eksp. Teor. Fiz.* **91**, 2008 (1986).
- [40] T. D. G. Walsh, J. E. Decker, and S. L. Chin, *J. Phys. B* **26**, L85 (1993).
- [41] V. P. Krainov, *J. Op. Soc. Am. B* **14**, 425 (1997).
- [42] A. Scrinzi and B. Piraux, *Phys. Rev. A* **56**, R13 (1997).
- [43] A. Saenz, *Phys. Rev. A* **61**, 051402 (R) (2000).
- [44] H. Hennig, J. Breidbach, and L. S. Cederbaum, *J. Phys. Chem. A* **109**, 409 (2005), and references therein.
- [45] S. E. Bialkowski, *Chem. Phys. Lett.* **83**, 341 (1981).
- [46] D. H. Waldeck, W. T. Lotshaw, D. B. McDonald, and G. R. Fleming, *Chem. Phys. Lett.* **88**, 297 (1982).
- [47] M. Aldén, S. Wallin, and W. Wendt, *Appl. Phys. B* **33**, 205 (1984).
- [48] J. W. Perry, N. F. Scherer, and A. H. Zewail, *Chem. Phys. Lett.* **103**, 1 (1983).
- [49] H. Ibrahim, M. Héjjas, M. Fushitani, and N. Schwentner, *J. Phys. Chem. A* **113**, 7439 (2009).
- [50] J. Mauritsson, T. Remetter, M. Swoboda, K. Klünder, A. L’Huillier, K. J. Schafer, O. Ghafur, F. Kelkensberg, W. Siu, P. Johnsson, M. J. J. Vrakking, I. Znakovskaya, T. Uphues, S. Zherebtsov, M. F. Kling, F. Lépine, E. Benedetti, F. Ferrari, G. Sansone, and M. Nisoli, *Phys. Rev. Lett.* **105**, 053001 (2010).

-
- [51] M. E. Casida, C. Jamorski, K. C. Casida, and D. R. Salahub, *J. Chem. Phys.* **108**, 4439 (1998).
- [52] A. Dreuw, J. L. Weisman, and M. Head-Gordon, *J. Chem. Phys.* **119**, 2943 (2003).
- [53] D. J. Lacks and R. G. Gordon, *Phys. Rev. A* **47**, 4681 (1993).
- [54] M. E. Casida, F. Gutierrez, J. Guan, F.-X. Gadea, D. R. Salahub, and J.-P. Daudey, *J. Chem. Phys.* **113**, 7062 (2000).
- [55] D. J. Tozer, *J. Chem. Phys.* **119**, 12697 (2003).
- [56] O. Gritsenko and E. J. Baerends, *J. Chem. Phys.* **121**, 655 (2004).
- [57] N. T. Maitra, *J. Chem. Phys.* **122**, 233104 (2005).
- [58] W. Hieringer and A. Görling, *Chem. Phys. Lett.* **419**, 557 (2006).
- [59] J. von Neumann, *Die Grundlehren der mathematischen Wissenschaften, Band XXXVIII: Mathematische Grundlagen der Quantenmechanik* (Springer, Berlin, 1932).
- [60] T. Kato and H. Kono, *Chem. Phys.* **366**, 46 (2009).
- [61] M. Born and J. R. Oppenheimer, *Ann. Physik* **84**, 457 (1927).
- [62] J. C. Slater, *Phys. Rev.* **35**, 210 (1930).
- [63] A. Szabo and N. S. Ostlund, *Modern Quantum Chemistry* (McGraw-Hill, New York, 1989), 1st (revised) edition.
- [64] C. C. J. Roothaan, *Rev. Mod. Phys.* **23**, 69 (1951).
- [65] G. G. Hall, *Proc. Roy. Soc. A* **205**, 541 (1951).
- [66] M. Knowles, M. Schütz, and H.-J. Werner, in *Modern Methods and Algorithms of Quantum Chemistry Proceedings*, edited by J. Grotendorst (John von Neumann Institute for Computing, Jülich, 2000), volume 3, p. 97, 2nd edition.
- [67] I. Shavitt, in *Methods of Electronic Structure Theory*, edited by H. F. Schäfer (Plenum, New York, 1977).
- [68] R. Paunz, *Spin Eigenfunctions* (Plenum, New York, 1979).

-
- [69] J. B. Foresman, M. Head-Gordon, J. A. Pople, and M. J. Frisch, *J. Phys. Chem.* **96**, 135 (1992).
- [70] L. N. Brillouin, *Act. Sci. Ind.* **71**, 159 (1933).
- [71] N. G. van Kampen, *Klg. Danske Vid. Sels. Mat. fys. Medd.* **26**, 15 (1951).
- [72] P. Krause and T. Klamroth, *J. Chem. Phys.* **128**, 234307 (2008).
- [73] A. D. Bandrauk, E. Aubanel, and S. Chelkowski, in *Femtosecond Chemistry*, edited by J. Manz and L. Wöste (Verlag Chemie, Weinheim, 1995), volume 2, chapter 25, p. 731.
- [74] P. A. M. Dirac, *Proc. Camb. Phil. Soc.* **26**, 376 (1930).
- [75] J. Frenkel, *Wave Mechanics* (Oxford Univ. Press, Oxford, 1934).
- [76] H. Levy and E. A. Baggott, *Numerical Studies in Differential Equations, Vol. 1* (Watts & Co., London, 1934), and references therein.
- [77] T. Koopmans, *Physica (Amsterdam)* **1**, 104 (1934).
- [78] S. Klinkusch, P. Saalfrank, and T. Klamroth, *J. Chem. Phys.* **131**, 114304 (2009).
- [79] J. C. Tremblay, S. Klinkusch, T. Klamroth, and P. Saalfrank, *J. Chem. Phys.* **134** (2011).
- [80] J. C. Tremblay, T. Klamroth, and P. Saalfrank, *J. Chem. Phys.* **129**, 084302 (2008).
- [81] K. Blum, *Density matrix theory and applications* (Plenum, New York, 1996).
- [82] G. Lindblad, *Commun. Math. Phys.* **48**, 119 (1976).
- [83] V. Gorini, A. Kossakowski, and E. C. G. Sudarshan, *J. Math. Phys.* **17**, 821 (1976).
- [84] V. Gorini and A. Kossakowski, *J. Math. Phys.* **17**, 1298 (1976).
- [85] I. I. Rabi, *Phys. Rev.* **51**, 652 (1937).
- [86] S. Shi, A. Woody, and H. Rabitz, *J. Chem. Phys.* **88**, 6870 (1988).

- [87] R. Kosloff, S. A. Rice, P. Gaspard, S. Tersigni, and D. J. Tannor, *Chem. Phys.* **139**, 201 (1989).
- [88] T. Klamroth, *J. Chem. Phys.* **124**, 144310 (2006).
- [89] W. Zhu, J. Botina, and H. Rabitz, *J. Chem. Phys.* **108**, 1953 (1998).
- [90] W. Zhu and H. Rabitz, *J. Chem. Phys.* **109**, 385 (1998).
- [91] T. Klamroth and D. Kröner, *J. Chem. Phys.* **129**, 234701 (2008).
- [92] A. Willets, J. E. Rice, D. M. Burlang, and D. P. Shelton, *J. Chem. Phys.* **97**, 7590 (1992).
- [93] L. Jensen, J. Autschbach, and G. C. Schatz, *J. Chem. Phys.* **122**, 224115 (2005).
- [94] L. Bergmann and C. Schäfer, *Lehrbuch der Experimentalphysik, Band 3: Optik* (Walter de Gruyter, Berlin / New York, 2004), 10th edition.
- [95] P. C. Hariharan and J. A. Pople, *Theor. Chim. Acta* **28**, 213 (1973).
- [96] M. J. Frisch, G. W. Trucks, H. B. Schlegel, G. E. Scuseria, M. A. Robb, J. R. Cheeseman, J. A. Montgomery, Jr., T. Vreven, K. N. Kudin, J. C. Burant, J. M. Millam, S. S. Iyengar, J. Tomasi, V. Barone, B. Mennucci, M. Cossi, G. Scalmani, N. Rega, G. A. Petersson, H. Nakatsuji, M. Hada, M. Ehara, K. Toyota, R. Fukuda, J. Hasegawa, M. Ishida, T. Nakajima, Y. Honda, O. Kitao, H. Nakai, M. Klene, X. Li, J. E. Knox, H. P. Hratchian, J. B. Cross, C. Adamo, J. Jaramillo, R. Gomperts, R. E. Stratmann, O. Yazyev, A. J. Austin, R. Cammi, C. Pomelli, J. W. Ochterski, P. Y. Ayala, K. Morokuma, G. A. Voth, P. Salvador, J. J. Dannenberg, V. G. Zakrzewski, S. Dapprich, A. D. Daniels, M. C. Strain, O. Farkas, D. K. Malick, A. D. Rabuck, K. Raghavachari, J. B. Foresman, J. V. Ortiz, Q. Cui, A. G. Baboul, S. Clifford, J. Cioslowski, B. B. Stefanov, G. Liu, A. Liashenko, P. Piskorz, I. Komaromi, R. L. Martin, D. J. Fox, T. Keith, M. A. Al-Laham, C. Y. Peng, A. Nanayakkara, M. Challacombe, P. M. W. Gill, B. Johnson, W. Chen, M. W. Wong, C. Gonzalez, and J. A. Pople, Gaussian 03, Revision c.02, Gaussian, Inc., Wallingford CT, 2004.

-
- [97] M. W. Schmidt, K. K. Baldridge, J. A. Boatz, S. T. Elbert, M. S. Gordon, J. J. Jensen, S. Koseki, N. Matsunaga, K. A. Nguyen, S. J. Su, T. L. Windus, M. Dupuis, and J. A. Montgomery, *J. Comput. Chem.* **14**, 1347 (1993).
- [98] A. A. Kilpio and M. V. Fedorov, *Laser Phys.* **7**, 295 (1997).
- [99] J. C. Tremblay, P. Krause, T. Klamroth, and P. Saalfrank, *Phys. Rev. A* **81**, 063420 (2010).
- [100] T. H. Dunning Jr., *J. Chem. Phys.* **90**, 1007 (1989).
- [101] M. Head-Gordon, R. J. Rico, M. Oumi, and T. J. Lee, *Chem. Phys. Lett.* **219**, 21 (1994).
- [102] T. Klamroth and M. Nest, *Phys. Chem. Chem. Phys.* **11**, 349 (2009).
- [103] M. Nest, T. Klamroth, and P. Saalfrank, *Z. Phys. Chem.* **224**, 569 (2010).
- [104] F. Jensen, *Introduction to Computational Chemistry* (Wiley & Sons, Chichester, 2001).

List of Figures

2.1	Shape function of a pulse used for the stochastic pulse optimization .	31
2.2	Electronic transitions and processes within TD-CI methods	33
3.1	Comparison of the algorithms for the determination of ionization rates	40
3.2	Optimal escape length for the LiCN system	41
3.3	Density of states for the LiCN system	42
3.4	Transitions below the ionization potential in the LiCN system	43
3.5	Transition to the ionizing state S_{69} in the LiCN system	45
3.6	Electronic wavepacket and pump-probe simulation for the LiCN system	48
3.7	Comparison of the geometries of the ground state and the fifth excited state within the BMQ7H system	49
3.8	Optimal escape length for the BMQ7H system	52
3.9	Ionization rates and density of states for the BMQ7H system	53
3.10	Electronic wavepacket within the BMQ7H system	54
3.11	Oscillation frequencies in the time-dependent, post-laser dipole mo- ment of a wavepacket within the BMQ7H system	55
3.12	Initial pump-probe simulation for the BMQ7H system	57
3.13	Frequency dependence of the loss of norm in the BMQ7H system . .	58
3.14	Transition dipole moments in the BMQ7H system	60
3.15	Optimized pump-probe simulation for the BMQ7H system	61
3.16	Dynamic polarizability in the H_2 molecule	65
3.17	Dynamic polarizability in the H_2 molecule with weaker ionization rates	66
3.18	Dissipation and photoionization during a π -pulse excitation	69
3.19	Dissipation and photoionization during a π -pulse sequence	71
4.1	Comparison of energies for the minimal basis model of H_2	76
4.2	Comparison of correlation measures for the minimal basis model of H_2	77

4.3	Potential energy for the H_2 molecule, calculated with different methods	79
4.4	Comparison of different methods and algorithms for entropy determination	80
4.5	CISD state populations forming the HF ground state	83
4.6	Laser-driven SEE minimization in H_2 using OCT	84
4.7	Laser-driven entropy minimization in H_2 using stochastic pulse optimization	86
4.8	SEE parameters and oscillation times for “partial wavefunctions” consisting of low-energetic eigenstates	88
4.9	SEE parameters and oscillation times for “partial wavefunctions” consisting of highly populated eigenstates	90
4.10	SEEs for different “truncated HF wavefunctions” in methane	92
4.11	OCT laser pulse for the CH_4 molecule resulting a decreased entropy	93
B.1	Imaginary time propagation for a model with three states	104

List of Tables

3.1	Energies and dipole moments in the LiCN molecule	39
3.2	Energies and dipole moments in the BMQ7H molecule	50
3.3	Energies and dipole moments in the H ₂ molecule	62
3.4	Excitation energies and dipole moments for the H ₂ molecule (CIS(D)/aug-cc-pVQZ)	68

Erklärung

Hiermit erkläre ich, dass ich die vorliegende Arbeit selbständig angefertigt habe und keine anderen als die angegebenen Quellen und Hilfsmittel verwendet habe.

Potsdam, im Juni 2011